

1996

# Modeling, characterization and integration of thin film resonator microsensors

Jie Xia

*Iowa State University*

Follow this and additional works at: <https://lib.dr.iastate.edu/rtd>

 Part of the [Acoustics, Dynamics, and Controls Commons](#), [Condensed Matter Physics Commons](#), and the [Electrical and Electronics Commons](#)

## Recommended Citation

Xia, Jie, "Modeling, characterization and integration of thin film resonator microsensors " (1996). *Retrospective Theses and Dissertations*. 11509.

<https://lib.dr.iastate.edu/rtd/11509>

This Dissertation is brought to you for free and open access by the Iowa State University Capstones, Theses and Dissertations at Iowa State University Digital Repository. It has been accepted for inclusion in Retrospective Theses and Dissertations by an authorized administrator of Iowa State University Digital Repository. For more information, please contact [digirep@iastate.edu](mailto:digirep@iastate.edu).

## INFORMATION TO USERS

This manuscript has been reproduced from the microfilm master. UMI films the text directly from the original or copy submitted. Thus, some thesis and dissertation copies are in typewriter face, while others may be from any type of computer printer.

The quality of this reproduction is dependent upon the quality of the copy submitted. Broken or indistinct print, colored or poor quality illustrations and photographs, print bleedthrough, substandard margins, and improper alignment can adversely affect reproduction.

In the unlikely event that the author did not send UMI a complete manuscript and there are missing pages, these will be noted. Also, if unauthorized copyright material had to be removed, a note will indicate the deletion.

Oversize materials (e.g., maps, drawings, charts) are reproduced by sectioning the original, beginning at the upper left-hand corner and continuing from left to right in equal sections with small overlaps. Each original is also photographed in one exposure and is included in reduced form at the back of the book.

Photographs included in the original manuscript have been reproduced xerographically in this copy. Higher quality 6" x 9" black and white photographic prints are available for any photographs or illustrations appearing in this copy for an additional charge. Contact UMI directly to order.

# UMI

A Bell & Howell Information Company  
300 North Zeeb Road, Ann Arbor, MI 48106-1346 USA  
313/761-4700 800/521-0600



Modeling, characterization and integration of thin film  
resonator microsensors

by

Jie Xia

A Dissertation Submitted to the  
Graduate Faculty in Partial Fulfillment of the  
Requirements for the Degree of  
DOCTOR OF PHILOSOPHY

Department: Electrical and Computer Engineering  
Major: Electrical Engineering (Microelectronics)

**Approved:**

Signature was redacted for privacy.

**In Charge of Major Work**

Signature was redacted for privacy.

**For the Major Department**

Signature was redacted for privacy.

**For the Graduate College**

**Committee:**

Signature was redacted for privacy.

Iowa State University

Ames, Iowa

1996

UMI Number: 9635375

---

**UMI Microform 9635375**  
**Copyright 1996, by UMI Company. All rights reserved.**

**This microform edition is protected against unauthorized  
copying under Title 17, United States Code.**

---

**UMI**  
**300 North Zeeb Road**  
**Ann Arbor, MI 48103**

## TABLE OF CONTENTS

CHAPTER 1. INTRODUCTION	1
Statement of Purpose	1
Literature Review	4
CHAPTER 2. TFR PIEZOELECTRIC THEORY	15
Piezoelectricity and Coupled Wave Theory	15
Coupled Waves In TFR Solid	19
Two-dimensional Device Analysis	31
Wave Analysis In TFR Liquid	36
CHAPTER 3. POLYMER-COATED AND LIQUID-COATED TFR ANALYSIS AND CHARACTERIZATION	42
Polymer-Coated TFR Analysis and Characterization	44
Liquid-Coated TFR Analysis and Characterization	72
CHAPTER 4. TFR ARRAY DESIGN AND MODELING	78
TFR Array Design	78
Array Acoustical Modeling	81
Array Electromagnetic Isolation	92
CHAPTER 5. TFR ARRAY PROCESS DEVELOPMENT AND ARRAY CHARACTERIZATION	95
Mask Design and Process Characterization	95
TFR Array Characterization	104
CHAPTER 6. SUMMARY AND RECOMMENDATIONS	114
BIBLIOGRAPHY	120
ACKNOWLEDGMENTS	124
APPENDIX I: IEEE TFR MICROSENSOR PAPER	125
APPENDIX II: MATRIX AND ENGINEERING NOTATION	126
APPENDIX III: DERIVED ALN MATERIAL MATRIX	127

APPENDIX IV: AIN AND QCM ELASTIC, PIEZOELECTRIC AND PERMITTIVITY MATRIX	128
APPENDIX V: FINITE DIFFERENCE ADMITTANCE	129
APPENDIX VI: DERIVATION OF THE STRAIN RATIO GENERATED BY CROSS-FILM GRADIENTS TO IN-PLANE GRADIENTS	130

## CHAPTER 1. INTRODUCTION

### Statement of Purpose

With the recent development of microresonators and SAW devices there is increasing interest to use these devices for the purposes of chemical sensing, interfacial study, and electrochemical analysis. Quartz crystal microbalances (QCMs) have played a vital part in most of these applications, based on their inexpensive cost, stable performance and excellent noise figure. Bulk thin film resonators (TFRs), as alternative devices with their small size, high sensitivity and compatibility with VLSI process, have also been applied to mass and chemical sensors and shown great promise for customized microelectronics. In order to realize sensing applications, an analyte sensing material must be coated onto the TFR, usually on the top surface. The capacity for accurate detection of TFR sensors is determined by the type of acoustic device, quality of piezoelectric film, metallization, interaction and selectivity between the analyte and the sensing coating, the support electronics, and the exposure environment. As shown in Figure 1.1, a typical TFR topology consists of multiple layers, with an aluminum nitride (AlN) film as the piezoelectric membrane capped with two planar-stacked metal layers. The silicon back-side window is etched away to assure fundamental-mode operation. The wave phase across the TFR composite is  $\pi$ , which gives a resonant frequency of around 1 GHz at about 5  $\mu\text{m}$  piezo-film thickness. The amount of response relies not only on the physically absorbed mass, but also depend on interaction between the sensing coating and analyte which may contribute volume expansion and viscoelastic variations. In order to accurately analyze TFR composite response, a multilayer coupled wave theory should be used to investigate the acoustic effects from each layer, especially the top analyte coating. This theory should also be used to characterize and distinguish mass loading and viscoelastic effects, and be flexible enough to be applied to other similar bulk-wave devices, such as QCMs and liquid-phase TFRs which utilize bulk shear waves.

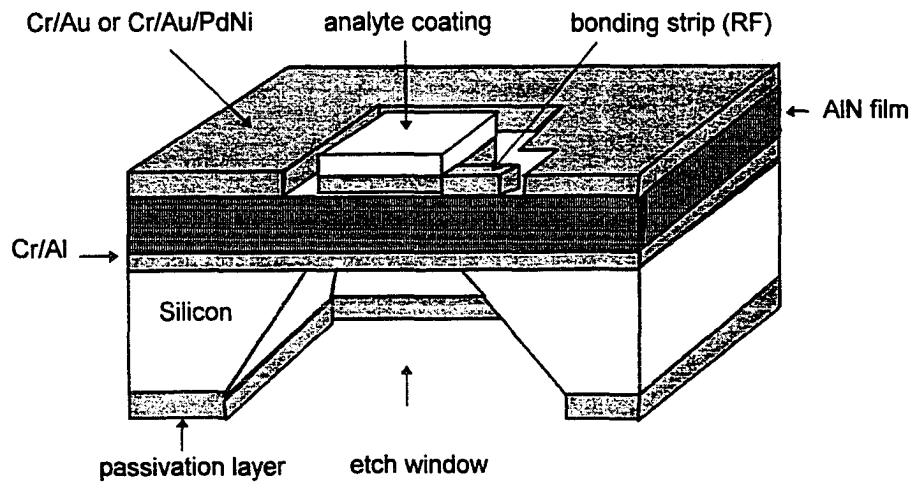


Figure 1.1 Typical TFR topological structure (not to scaled)

A two-dimensional finite difference method is also used to compare to the one-dimensional analysis, and to verify with the experimental results. The concepts of acoustical thickness and film resonance applied in TFR polymer sensors are discussed. Experimental characterization of polymer-coated and liquid-coated TFRs are then presented along with the theoretical analysis. Sensitivity and detection limit are also discussed with comparison to other devices.

Thin piezoelectric films used in TFRs are usually the sputtered ZnO, AlN, or Sol-gel PZT. With its high velocity, strong mechanical properties, relative ease of deposition, and resistance to environment affecting, aluminum nitride is a commonly used material. As in other sputtered film material, phase noise (mainly induced by defects) can cause frequency instability. The temperature coefficient is usually higher than that of quartz crystal, which in turn induces response drifting and noise. In order to minimize these temperature-induced effects, high-temperature CVD epitaxial or MBE growth are desired. However, these high-temperature processes do not easily integrate with BJT or CMOS processing. Another way to reduce temperature effect is to perform rapid thermal annealing immediately after aluminum

nitride is sputtered, but this may deteriorate the piezoelectric properties because of built-in defects, underneath aluminum or chrome, which can easily outdiffuse along AlN defect sites, especially the grain boundaries. The resulting laterally expanded columnar structure may reduce film density and misalign the crystal axis, which in turn worsens piezoelectricity. The method presented in this work is to design a TFR array which can compromise multiple TFRs on a single aluminum nitride membrane, as shown in Figure 1.2. The differential responses from the active (analyte) TFR and inactive (reference) TFR should compensate the temperature and other material-related effects to the first order. Another benefit of this approach is that by applying different coatings on different TFRs, one can conduct multi-analyte chemical pattern recognition. With different coating thickness, one may differentiate the responses resulting from either surface or bulk phenomena.

The major challenge for this array design is to evaluate wave crosstalk between individual TFRs; In other words, to find out how closely individual TFRs can be patterned on a single AlN membrane. These acoustical and electromagnetic couplings should be controlled to an acceptable level so as to not interfere with the adjacent TFRs. Another challenge is to find out how many TFRs can be housed in a single AlN membrane, in other words, to find out how much mechanical strength

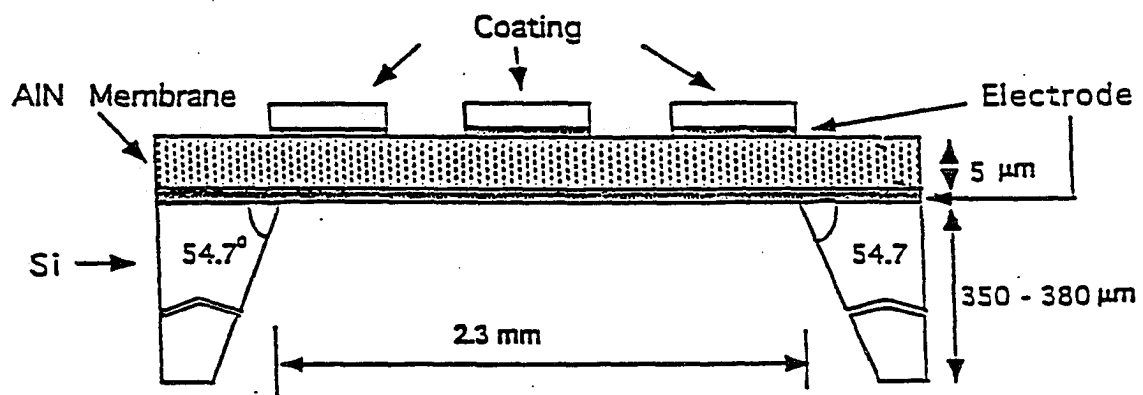


Figure 1.2 TFR array structure

the piezoelectric film can possess. Analytical and numerical methods are used to model these couplings or crosstalks and to assist process mask design. The modified process flow based on the standard TFR technology is presented and implemented. The measurements were made and compared with the modeled results. The characterization of responses of a TFR polymer sensor array is then investigated and discussed.

### Literature Review

Acoustic sensors are devices that employ elastic waves at frequencies in the megahertz to low gigahertz range to measure physical, chemical, or biological quantities. Their high sensitivity makes these devices particularly attractive for chemical vapor and gas sensing. Elastic waves in a solid are produced when atoms of the solid are forced either by an external electric field or mechanical stress. The neighboring atoms then produce a restoring force tending to bring the displaced atoms back to their original positions. These sensors are designed so that the propagation characteristics of these waves -- their phase, velocity, and resonator quantities (Q and resistance) -- are affected by the measurands of interest. Thus, in some of these devices, gravimetric or polymerized softening effects such as the sorption of molecules or the attachment of bacteria via the affinity coating causes a reduction of wave velocity and resonant Q. In others, mechanical forces induced by an applied pressure or an acceleration of the sensor increase the wave velocity. Acoustic waves are attenuated when a viscous liquid contacts the active region of an elastic wave sensor. The interesting parameters of liquid such as density and viscosity can be measured through the changes of resonant properties. These devices, which are based on propagation waves, include bulk thickness shear mode (TSM), surface acoustic wave (SAW), flexural plate wave (FPW), and acoustic plate mode (APM) sensors<sup>1-10</sup> Their basic acoustic motions are illustrated in Figure 1.3. One-port configured quartz crystal microbalance resonators (QCMs) and shear-

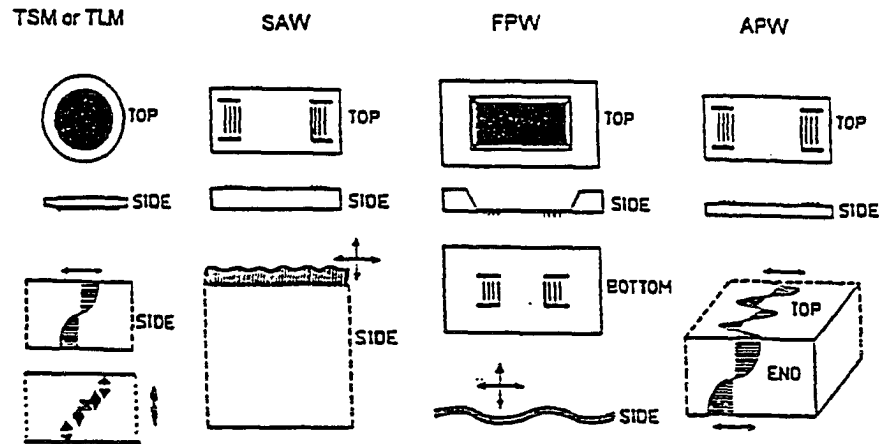


Figure 1.3 Wave motions in various acoustic devices<sup>1</sup>

mode TFRs are TSM devices, while longitude-mode TFRs utilize thickness longitude mode (TLM).

For low-cost and high-sensitivity acoustic sensors, a monolithic technology is required, where the sensor elements and electronics are processed and manufactured on the same substrate. To design and fabricate a monolithic acoustic sensor which is compatible with standard VLSI process, a piezoelectric film is required. During the past decade, many researchers reported useful characteristics of piezo-films for different growth methods and applications<sup>11-13</sup>. Thin film resonators made with magnetron sputtered AlN or ZnO piezo-films are among the most common. This type, often associated with GPS communication systems,<sup>14</sup> have been developed as chemical or mass microsensors and phased-array antenna systems.<sup>15</sup> Aluminum nitride is a promising thin film piezoelectric material due to its high acoustic velocity and endurance in humidity and high temperature. Its piezoelectric coupling factor is relatively large; it is lower than ZnO but higher than most other thin film materials, excluding thin film piezoelectric ceramics. The high acoustic velocity and mechanical endurance of AlN makes it very attractive at

frequencies in the GHz range which promote high mass sensitivity. The initial investigation is to grow AlN film from CVD or MBE methods,<sup>1</sup> whereby high quality films can be obtained. The drawback of these methods is the high substrate temperature used (1000-1300 C),<sup>16-18</sup> which restricts standard VLSI metallization and limits substrate choices. The VLSI compatibility issues stimulate other film growth techniques. Magnetron sputtering is the most promising one because of its low-temperature growth, well-understood technique, and ease of implementation.<sup>12,19,20</sup> TFRs with AlN piezoelectric films are usually used in bulk thickness-longitude mode (TLM) to sense gravimetric gaseous absorbers, and in thickness shear mode (TSM) to detect liquid properties. To sense different gases or vapors, a selective coating is deposited on the resonator surface. This coating, either metallic or polymer, is subjected to an oscillation driving force at the resonator/coating interface. The gaseous or vapor species and the amount of the absorbed species can be directly measured by a network analyzer or by a TFR-controlled oscillator in which the TFR is used as a feedback element. By applying a two-port configuration and different electrode patterning, TFRs can also propagate surface or plate waves. Of the many TFR topologies, edge-supported, P<sup>+</sup>-Si membrane and SiO<sub>2</sub> or Si<sub>3</sub>N<sub>4</sub> membrane-supported are used most. These structures are shown in Figure 1.4. The early-developed P<sup>+</sup>-Si membrane layer is now replaced by PVD or CVD SiO<sub>2</sub> and Si<sub>3</sub>N<sub>4</sub> films because of the compatibility requirement with the VLSI process. All these devices have been made by bulk silicon processing. Thin film resonators made by surface processing (sacrificial etch) as shown in (d) in Figure 1.4 could be attractive to further reduce device size, enhancing compatibility with industrial CMOS/BiCOMS processes. The typical cross-section view of motion of QCMs and TFRs is shown in Figure 1.5. The minimum requirements for QCM or TFR sensors include an analyte coating (metallic or polymer), a means of exciting acoustic waves (quartz crystal or c-axis vertical piezoelectric aluminum nitride, or zinc oxide), and a set of electrodes (either gold or

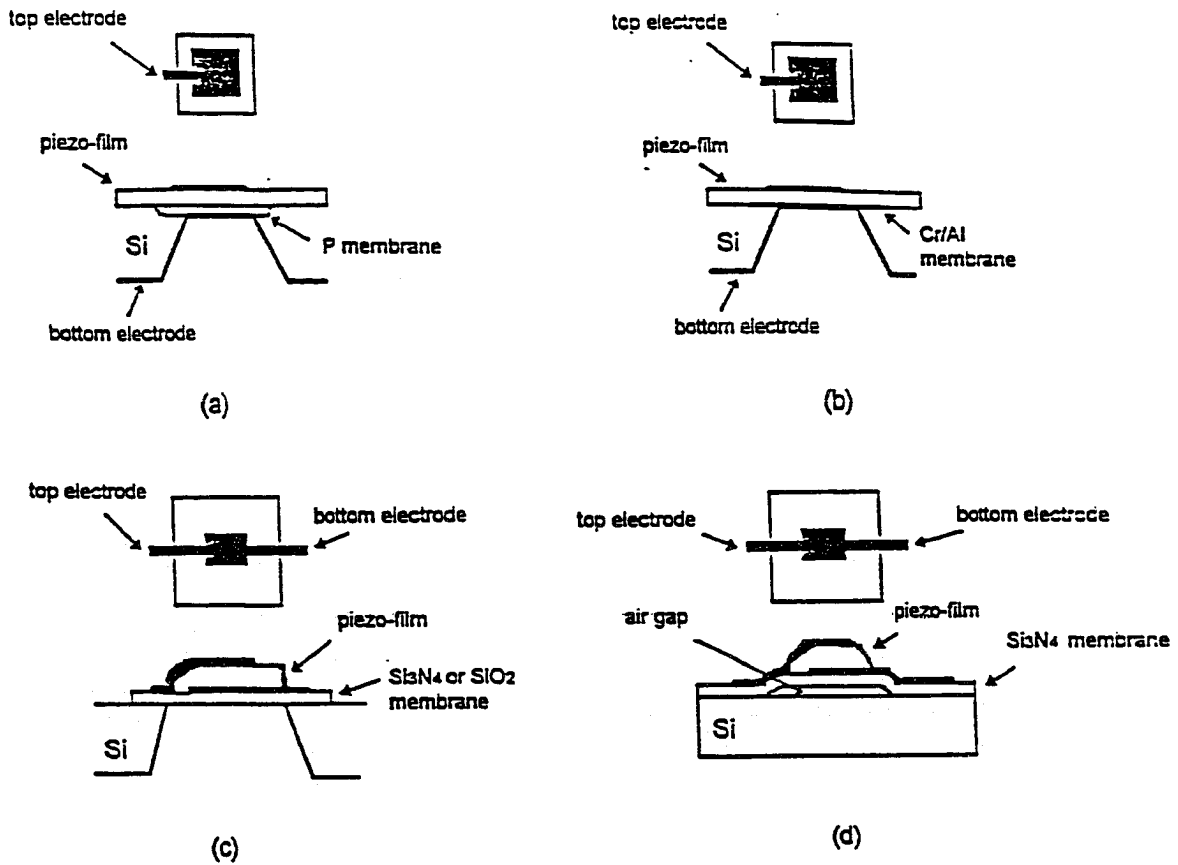


Figure 1.4 Among film acoustic resonators are bulk P<sup>+</sup> layer edge-supported (a), metal edge-supported (b), bulk Si<sub>3</sub>N<sub>4</sub> or SiO<sub>2</sub> membrane-supported (c), and surface Si<sub>3</sub>N<sub>4</sub> membrane-supported (d)

aluminum). Acoustic standing waves are generated by piezoelectric excitation, which is caused by applying an external electric field. These waves propagate and reflect within these multilayer composite structures. Those acoustic and electrical responses such as velocity, resonant Q and resistance are varied by the mechanical, piezoelectric and permittivity properties of each layer and can be directly measured.

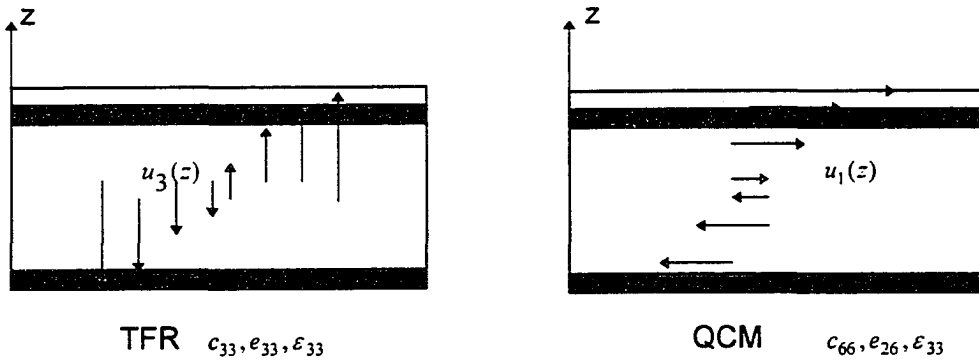


Figure 1.5. TFR and QCM motional displacements

The frequency perturbation of a resonator upon the sorption of the analyte can best be described by boundary and internal perturbation theory in which all the induced changes can be derived as,<sup>21</sup>

$$\frac{\Delta f_s}{f_s} = \frac{j}{8\pi f_s U_{ss}} \int_S \{ \mathbf{v}_s^* \cdot \mathbf{T}_s' + \mathbf{v}_s' \cdot \mathbf{T}_s^* - \phi_s^* (i\omega_s \mathbf{D}_s)' - \phi_s' (i\omega_s \mathbf{D}_s)^* \} \cdot \hat{\mathbf{n}} dS \quad (1.1)$$

$$- \frac{1}{4U_{ss}} \int_V (\Delta \rho \mathbf{v}_s^* \cdot \mathbf{v}_s' - \mathbf{S}_s^* : \Delta \mathbf{c}^E : \mathbf{S}_s' + \mathbf{E}_s^* \cdot \Delta \mathbf{e}^T \cdot \mathbf{E}_s' + \mathbf{E}_s' \cdot \Delta \mathbf{e} : \mathbf{S}_s^* + \mathbf{S}_s^* : \Delta \mathbf{e} \cdot \mathbf{E}_s') dV$$

$$U_{ss} = \frac{1}{2} \int_V (\rho \mathbf{v}_s^* \cdot \mathbf{v}_s') dV \quad (1.2)$$

where,  $U_{ss}$ ,  $\mathbf{v}$ ,  $\mathbf{S}$ ,  $\mathbf{T}$ ,  $\mathbf{E}$ ,  $\rho$ ,  $\mathbf{c}$ ,  $\mathbf{e}$  are the storage energy in TFR, wave velocity, strain, stress, electric field, coating density, viscoelastic and piezoelectric coefficients, respectively. If there is no electrical surface and internal perturbation, and no piezoelectric and dielectric variations inside the piezoelectric material has occurred, the responses caused by a thin coating can then be simplified as

$$\frac{\Delta f_s}{f_s} = \frac{j}{4\omega_s U_{ss}} \int_S \{ \mathbf{v}_s^* \cdot \mathbf{T}_s' + \mathbf{v}_s' \cdot \mathbf{T}_s^* \} \cdot \hat{\mathbf{n}} dS \quad (1.3)$$

which consists of boundary velocity and stress field perturbation. If only a pure mass layer is deposited onto the resonator, then frequency changes can be derived from the equation (1.3) and expressed by the classical Sauerybrey equation,<sup>22</sup>

$$\frac{\Delta f_s}{f_s} = -\frac{2f_s}{v_s \rho} \left( \frac{\Delta m}{A} \right) \quad (1.4)$$

where  $\Delta m$ ,  $A$ ,  $f_s$ ,  $v_s$ ,  $\rho$  are the absorbed analyte mass, active device area, resonant frequency, velocity and density of resonator, respectively. This is a good approximation for a rigid, acoustically thin coating under low frequency operation. It is accurate only for mass depositions less than 2% of the mass of the resonator.<sup>5</sup>

However, responses due to gas or vapor absorption via the coating are different from that of just a thin mass layer deposited onto resonators. Complicated phenomena may arise from the changes of acoustical, electrical, and chemical properties of the coating. Although many QCM/TSM sensor applications utilize the Sauerybrey equation to extract the absorbed mass and are in agreements with experiments, this relation may not be directly interpreted to vapor absorption via a thick soften layer, especially in TFR high frequency applications. For soften and acoustically thick layers, especially for polymer films, a non-gravimetric response may arise from the plasticization or vapor-induced softening.<sup>6</sup> Viscoelastic nature of soften coating may cause elastic energy to be both stored and dissipated during film deformation which may be induced by vapor absorption or temperature changes. Viscoelasticity may also be varied by chemical absorption and reaction between analyte and coating. For example in the Pd-H<sub>2</sub> system, mass loading is usually shown in low hydrogen content. Under high hydrogen concentration, the elastic moduli may be changed by a different Pd-H<sub>2</sub> phase status. Some observed

that the Young modulus could be changed to about 20 % under high hydrogen contents.<sup>2,3</sup> For acoustically thick polymers in SAW microsensors, the actual responses may be four to six times greater than the calculated mass effects, mostly due to film plasticization and viscoelastic effects.<sup>7</sup> Coating plasticizing and viscoelastic effects may even become very difficult to predict if high frequency and temperature effects are considered. The dynamic response of vapor absorption via coating is thus required to investigate the boundary velocity and stress fields due to all the changes of coating mass, thickness (plasticizing effects), and viscoelastic properties. However, little has been done to investigate wave phenomena and analyze velocity and stress field on TFR sensors.

Martin et al. first introduced the concept of acoustical thickness to interpret responses of two-port SAW polymer sensors.<sup>6</sup> The criterion for separating acoustically thin and thick coating in SAW devices is judged by the ratio ( $R$ ) of cross-plane strain to in-plane strain. Polymer coatings with  $R \ll 1$  are considered as acoustically thin film, while coatings with  $R \gg 1$  are acoustically thick film. By using this concept, he explains SAW responses with temperature variation and high vapor concentration. In contrast to two-port SAW devices, TFRs are characterized by one-port configuration and utilize different acoustic modes. The wave motion in TFR polymer sensors is thus expected to be different. Also the frequency used in TFRs are several times larger than that in SAW devices, which may result in different wave phenomena. The correct interpretation of the frequency responses of TFR polymer sensors is thus required.

The difference between TFRs and QCMs, in addition to the propagation mode and frequency range, is that metal electrodes in TFRs can be a substantial fraction of the total TFR thickness at GHz range. The dimension used in TFRs has a large lateral extent compared to the resonator thickness in order to realize energy trapping and electrically matching 50  $\Omega$  system. It has been found that metallization plays an important role in TFR sensor characterization. Metal deposition, patterning and passivation can affect device electrical and acoustic properties. It is known that

aluminum has the best acoustic performance with good acoustic matching with AlN and small acoustic loss among the common used electrode metals, however it is not inert to the environment. On the other hand, gold, an often used electrode metal, has more acoustic attenuation because of its high mass density<sup>24</sup>. In order to reduce metal conductive loss and improve step coverage, a thicker electrode is preferred in top metallization. However, the thicker the electrode is, the more imperfections are incorporated in the deposition, and the worse the acoustic homogeneity is, which in turn produces more acoustic loss. Thicker electrodes may also produce metal local resonance and interfere with coating sensitivity. Electrode edge discontinuity may also generate spurious plate waves. Built-in strains, either compressive or tensile, are always associated with deposited films and strongly depend on process parameters. Interfacial microstructure mismatch may produce stress. These effects may result in unstable phase correlation between wave reflection and membrane thickness, and rough reflected surfaces. Therefore, intermediate layers, either stress-relief or adhesion, are routinely incorporated in TFR structures. TFR analysis and characterization thus must include these effects from the electrode and intermediate layers.

To model wave propagation along TFR sensors, a multilayer coupled wave theory has to be considered. Single-mode devices of either thickness-longitude and thickness-shear wave are usually considered in resonator analysis. This is the case for QCMs since well-defined bulk processing of crystalline materials and their associated cuts are well developed and available in the market. However, this may not be appropriate for TFRs since a c-axis sputtered AlN film, depending on the processing, is not always perfectly perpendicular to the substrate, or uniform across the wafer. Considerable quasi-shear strain can occur along thickness direction and produce quasi-shear and spurious responses. It often requires complicated two- or three-dimensional finite element method (FEM)<sup>25</sup> or finite difference method (FDM) to numerically solve these boundary-value problems. Since TFRs work in the low-microwave frequency region (very short wavelength), large mesh points are needed

to accurately implement these numerical methods which may cost a lot of computing time and manpower. A large width to thickness ratio is designed in TFRs so that the one-dimensional assumption can be applied without serious loss of accuracy. Multiport network models based on the Mason model have been developed for low-frequency crystal multilayer structures,<sup>24,26-29</sup> and TFR composite.<sup>9</sup> Although wave analysis has also been used in recent years,<sup>30,31</sup> assumptions such as the ignoring of metal and intermediate layer and constant displacement across thin layers, were often used which may not accurately reflect real device operation. Also most analysis and characterization has been done based on the extended BVD equivalent models which were specifically developed for QCM applications and may not directly interpret wave propagation phenomena. Few have been done on full wave analysis of a multi-layer TFR sensor structure. While used in liquid phase, TFR thickness-shear mode is generated and attenuated in the contacting solution. The detectable displacement or velocity field contains the information about the liquid, such as viscosity and density. No theoretical study of TFR liquid analysis has been done yet. In this study, a one-dimensional full coupled wave theory is illustrated to model wave propagation and electrical response both in TFR solid composite and in liquid phase. The mass loading and viscoelastic effects from each layer can be separately illustrated. A two-dimensional finite difference method is implemented to compare with one-dimensional analysis and the experimental results.

With an understanding of the device acoustic phenomena, experiments based on TFR polymer sensors and liquid sensors can be conducted. Both longitude and shear mode TFR polymer sensors will be considered. One-port configuration will be used to characterize device resonant frequency, resistance,  $Q$ , inductance and capacitance through an HP 8731 network analyzer. Polymers usually have large hydrocarbon molecular chains and many vacancy-sites where the analyte is relatively easy to absorb and diffuse. The concept of acoustical thickness and film resonance are then introduced to TFR polymer sensors, along with

experimental characterization. The sensitivity and mass detection limits are also discussed with a comparison to other acoustic devices. To explore TFR-liquid biosensor applications, the experimental characterization of TFR-water is demonstrated along with modeling.

Microsensor arrays have been actively studied in recent years for development of complete microanalytical systems.<sup>32,33</sup> The driving force behind this approach is that resonators, either TSM or SAW devices, are easily influenced by their surrounding environment, especially by temperature. These effects may oversize the response due to analyte absorption if single device is used. With a pre-calibrated sensing pattern, a microsensor array is able to interpret response more correctly, and can be used to detect 'real' gas or vapor environment with much less data acquisition effort. Many studies have also been done in reducing the size and power consumption of a microsensor system. The TFR array should be attractive in these microanalytical systems because of its super-small size and compatibility to microelectronics integration. The temperature coefficient (TC) for shear AlN/Si TFR is around  $-24 \text{ ppm}/^\circ\text{C}$ .<sup>34</sup> Although TC of longitude TFR is expected to be smaller than that of shear TFR, temperature effect may cause response drifting and deteriorate sensitivity, particularly in TFR polymer sensors. To compensate both the environmental-induced drift and other effects such as uniformity, geometrical and material mismatch, a differential approach is proposed where the differential output from a reference TFR and an analyte TFR should be able to compensate the temperature-induced drifting and other material effects to the first-order. To utilize on-chip microsensor integration, monolithic integration of a TFR array with active devices should be constructed. To acoustically isolate individual TFRs, patterning AlN is required. Effectively etching III-V nitrides has is a very difficult task. The solubility of AlN film was only observed in strongly oxidizing acidic and basic Si cleaning solutions. Hot 85% phosphoric acid or 10% sodium hydroxide are usually used as the etchants.<sup>35,36</sup>  $\text{BCl}_3/\text{Cl}_2/\text{N}_2$  RIE dry etch has been recently investigated<sup>37,38</sup> but this chemistry is not selective to the underneath aluminum.

Also etch rates in these techniques are fairly low. Other methods like dialectically-assisted liftoff or aperture mask processes have also been used for AlN definition.<sup>39</sup> However the patterning and definition of individual TFRs with  $5\mu$  nominal thickness of AlN used by these methods have not been optimized. ECR or other high density plasma (HDP) have been used to etch III-V nitrides recently,<sup>40</sup> but this capability was not available for this research. Instead of patterning TFRs individually, another way to make a TFR array is to house multiple TFRs on a single AlN membrane. Either hybrid or monolithic integration can then be incorporated with this array structure to realize a microoscillator or other signal-condition circuits. The major challenge associated with this array design is the acoustic and electromagnetic wave coupling between TFRs. The electrode edge evanescent electric field can be isolated by standard design rules for microstrip and coplanar waveguide MMICs. A two-dimensional numerical scheme is originally implemented to model the acoustic coupling which could be interpreted by the electrically measured insertion loss. From the modeled results, the actual masks are generated. With some modifications of the present TFR processes, the array structures can be fabricated. In this study, the temperature compensation was characterized and demonstrated through a TFR polymer sensor array. The selectivity experiments on TFR polymer sensor array were also conducted and compared with QCM results. This array approach may have benefit for interfacial study and sensing pattern recognition, eventually leading to fully automated microanalytical systems.

## CHAPTER 2. TFR PIEZOELECTRIC THEORY

### Piezoelectricity and Coupled Wave Theory

At equilibrium in a piezoelectric material, crystal strain force is balanced by the internal polarization force. When this equilibrium is disturbed either by application of an external electric field or external mechanical stress, the emitting depolarization field will create a rebalance force to maintain the initial equilibrium. If the external force is an electric field, a displacement will occur, but if the external force is from a mechanical displacement, then an electric field will be produced. Electromagnetic field and acoustic field are coupled by the constitutive relation within a piezoelectric material. Acoustic sensors can be designed based on piezoelectricity because they provide an effective means for electrically generating and detecting acoustic vibrations or vice versa. Linear theory of piezoelectricity in a solid can be used for the sensing purpose since small magnitude perturbation is usually expected. Under the conditions of linear material and steady-state case, the governing equations of a piezoelectric sensor are Newton's law, Gauss's law and the constitutive relations that are expressed in following,<sup>21</sup>

Newton's law (no mechanic body force) is

$$\frac{\partial T_{ij}}{\partial x_i} = -\rho \omega^2 u_j \quad (2.1)$$

Gauss's law is

$$\frac{\partial D_i}{\partial x_i} = 0 \quad (2.2)$$

The constitutive relations are

$$T_{ij} = c_{ijkl} \frac{\partial u_k}{\partial x_l} + e_{kij} \frac{\partial \phi}{\partial x_k} \quad (2.3)$$

$$D_i = e_{ikl} \frac{\partial u_k}{\partial x_l} - \varepsilon_{ik} \frac{\partial \phi}{\partial x_k} \quad (2.4)$$

The variables used are listed in following,

$T_{ij}$	Stress ( $N / m^2$ )
$u_{ij}$	Displacement ( $m$ )
$S_{ij}$	Strain ( $m / m$ )
$D_i$	Electric Flux Density ( $C / m^2$ )
$\phi$	Electric Potential ( $V$ )
$\omega$	Radian Frequency ( $rad / s$ )
$c_{ijkl}$	Viscoelastic Tensor ( $N / m$ )
$e_{ijk}$	Piezoelectric Tensor ( $C / m^2$ )
$\varepsilon_{ik}$	Permittivity ( $F / m$ )

The repeated subscripts imply summation ( $i, j, k, l = 1, 2, 3$ .) These equations in engineering form can also be expressed in matrix form  $\mathbf{u}$ ,  $\mathbf{v}$ ,  $\mathbf{S}$ ,  $\mathbf{T}$  for mathematical simplification. The relationship between the Full (or the Engineering) and the Abbreviated (or the Matrix) notation is summarized in Appendix II. The strain field  $\mathbf{S}$  is related to the particle displacement field  $\mathbf{u}$  by the stress-displacement equation

$$\mathbf{S} = \nabla_s \mathbf{u} \quad (2.5)$$

where

$$\nabla_s = \begin{bmatrix} \partial/\partial x & 0 & 0 \\ 0 & \partial/\partial y & 0 \\ 0 & 0 & \partial/\partial z \\ 0 & \partial/\partial z & \partial/\partial y \\ \partial/\partial z & 0 & \partial/\partial x \\ \partial/\partial y & \partial/\partial x & 0 \end{bmatrix} \quad (2.6)$$

The boundary conditions involved in acoustic devices are the continuity of displacement velocity and traction force

$$\mathbf{v} = \mathbf{v}' \quad (2.7)$$

$$\mathbf{T} \cdot \hat{\mathbf{n}} = \mathbf{T}' \cdot \hat{\mathbf{n}} \quad (2.8)$$

An important approximation that is often used in analysis of acoustic devices is the so-called quasistatic approximation in which the rotational (electromagnetic) electrical field is neglected comparing to potential gradients.<sup>21</sup> This is especially true for materials with low piezoelectricity, such as quartz and film piezoelectric materials (except ceramic films). In other words, the piezoelectricity has little effect on electromagnetic and acoustic wave propagation which results in a greatly simplified wave analysis. Electromagnetic and acoustic wave propagation can be separately treated by EM wave theory and acoustic wave theory provided that the piezoelectricity stiffened elastic constants are used whereas they are required. The example illustrated in the next section for acoustic wave propagation in TFR solids gives more detail discussion.

Substituting (2.3) into (2.1) and (2.4) to (2.2), one can derive the coupled equations and the constitutive relations as a set of general PDEs in the rectangular coordinator.

$$\begin{aligned}
& A_{jk} \frac{\partial^2 u_k}{\partial x_1^2} + B_{jk} \frac{\partial^2 u_k}{\partial x_2^2} + C_{jk} \frac{\partial^2 u_k}{\partial x_3^2} + (D_{jk} + E_{jk}) \frac{\partial^2 u_k}{\partial x_1 \partial x_2} + \\
& (F_{jk} + G_{jk}) \frac{\partial^2 u_k}{\partial x_2 \partial x_3} + (H_{jk} + I_{jk}) \frac{\partial^2 u_k}{\partial x_1 \partial x_3} = \lambda_j u_j
\end{aligned} \tag{2.9}$$

The stresses are derived as

$$T_{1j} = A_{jk} \frac{\partial u_k}{\partial x_1} + D_{jk} \frac{\partial u_k}{\partial x_2} + H_{jk} \frac{\partial u_k}{\partial x_3} \tag{2.10}$$

$$T_{2j} = E_{jk} \frac{\partial u_k}{\partial x_1} + B_{jk} \frac{\partial u_k}{\partial x_2} + F_{jk} \frac{\partial u_k}{\partial x_3} \tag{2.11}$$

$$T_{3j} = I_{jk} \frac{\partial u_k}{\partial x_1} + G_{jk} \frac{\partial u_k}{\partial x_2} + C_{jk} \frac{\partial u_k}{\partial x_3} \tag{2.12}$$

where

$$\lambda_j = -\rho\omega^2 \quad j = 1, 2, 3 \tag{2.13}$$

$$\lambda_j = 0 \quad j = 4 \tag{2.14}$$

$$k = 1, 2, 3, 4 \tag{2.15}$$

$$u_4 = \phi \tag{2.16}$$

$A_{jk}, B_{jk}, C_{jk}, D_{jk}, E_{jk}, F_{jk}, G_{jk}, H_{jk}, I_{jk}$  are material constant matrices and are shown in Appendix III. With the assumptions of weakly coupled and non-degenerate, an equation for one-dimensional single-mode wave can be formed and was solved for

several cases.<sup>30,31</sup> For TFRs, one-dimensional assumption is often obeyed but multi-modes are often observed. The complete answer for modeling composite TFR and QCM devices is to numerically solve three-dimensional boundary-value problems, which itself is an advanced research area. Also these calculations require an extremely large amount of computation time since short wavelength and high velocity were used. Further discussion about varied numerical methods is beyond the scope of this study. Simplifying approximations may be made to derive the fundamental relations without seriously affecting the actual results. One-dimensional description of coupled wave phenomena in multilayer structures is described. A two-dimensional finite difference model is implemented to verify the one-dimensional analysis.

#### Coupled Waves In TFR Solid

The general piezoelectric theory introduced in the last section is applicable to all linear materials. In an isotropic medium such as a polymer, the three coordinate axes,  $x, y, z$  and the three coordinate planes,  $yz, xz, xy$  are equivalent. Consequently, the response of the medium must be the same for a compressive stress applied along any axis. Also the shear strain produced by a shear stress must be the same for all coordinate planes. The general 6 X 6 elastic matrix shown in appendix IV has only two independent components  $c_{11}$  and  $c_{44}$ ,

$$c_{12} = \lambda \quad (2.17)$$

$$c_{44} = \mu \quad (2.18)$$

$$c_{11} = c_{22} = c_{33} = \lambda + 2\mu \quad (2.19)$$

The elastic modulus can be written as the general elastic constants  $c_{IJ}$ , or *Lame constants*,  $\lambda$  and  $\mu$ , and shear and bulk modulus  $G, K$ . The moduli used in TFR isotropic media are shown in Table 2.1.<sup>6</sup> These moduli are important in analysis of TFR polymer sensors. Metal layers used in TFR composites such as aluminum and gold are cubic medium that has three independent elastic constants  $c_{11}, c_{12}, c_{44}$ , while aluminum nitride piezoelectric film has hexagonal structure with five independent elastic constants  $c_{11}, c_{12}, c_{13}, c_{33}, c_{44}$ . In these cases, the elastic constant matrix is required to perform wave analyses since anisotropic properties are expected.

A TFR composite consisting of an analyte coating, top electrode, AlN piezoelectric film and bottom electrode is shown in Figure 2.1. Since larger width to thickness ration (larger than 50) is designed to the TFR topology, one-dimensional analysis could be used without loss of accuracy. Then no variations are permitted in the lateral plane ( $x_1, x_2$ ). The coupled wave equation can be simplified from equation (2.9) as

Table 2.1 Elastic moduli used for TFR-isotropic medium

strain mode	displacement gradient	modulus definition	modulus in terms of $\lambda, \mu$	modulus in terms of $G, K$
transverse shear	$\frac{\partial u_x}{\partial z}$	$E^{(1)} = \frac{T_{13}}{2S_{13}}$	$\mu$	$G$
Longitude compression	$\frac{\partial u_z}{\partial z}$	$E^{(3)} = \frac{T_{33}}{S_{33}}$	$\frac{4\mu(\lambda + \mu)}{\lambda + 2\mu}$	$\frac{4G(3K + G)}{3K + 4G}$

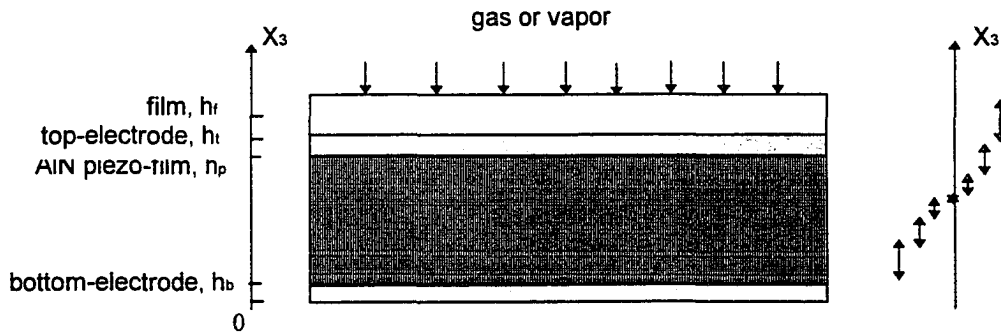


Figure 2.1 A cross-section view of TFR composite

$$C_{jk} \frac{d^2 u_k}{dx_3} = \lambda_j u_j \quad (2.20)$$

The notations are the same as in equation (2.9). Expanded (2.20), the following set of equations can be obtained

Displacement

$$\overline{C}_{11} \frac{d^2 u_1}{dx} + \overline{C}_{12} \frac{d^2 u_2}{dx} + \overline{C}_{13} \frac{d^2 u_3}{dx} = -\rho \omega^2 u_1 \quad (2.21)$$

$$\overline{C}_{21} \frac{d^2 u_1}{dx} + \overline{C}_{22} \frac{d^2 u_2}{dx} + \overline{C}_{23} \frac{d^2 u_3}{dx} = -\rho \omega^2 u_2 \quad (2.22)$$

$$\overline{C}_{31} \frac{d^2 u_1}{dx} + \overline{C}_{32} \frac{d^2 u_2}{dx} + \overline{C}_{33} \frac{d^2 u_3}{dx} = -\rho \omega^2 u_3 \quad (2.23)$$

Potential

$$\phi(x) = -\frac{C_{41}}{C_{44}}u_1 - \frac{C_{42}}{C_{44}}u_2 - \frac{C_{43}}{C_{44}}u_3 + \xi x + \eta \quad (2.24)$$

Stress

$$T_{1j} = H_{jk} \frac{du_k}{dx} \quad (2.25)$$

$$T_{2j} = F_{jk} \frac{du_k}{dx} \quad (2.26)$$

$$T_{3j} = C_{jk} \frac{du_k}{dx} \quad (2.27)$$

where

$$\overline{C}_{jk} = C_{jk} - \frac{C_{j4}C_{4k}}{C_{44}} \quad j, k = 1, 2, 3 \quad (2.28)$$

$\xi, \eta$  are constants

$x_3$  here is replaced by a general variable  $x$  for simplification. The general solutions to (2.21-2.23) can be written as (2.29-2.31) which comprise incident and reflection waves inside the TFR composite

$$u_1(x) = a_1 e^{j\kappa x} + b_1 e^{-j\kappa x} \quad (2.29)$$

$$u_2(x) = a_2 e^{j\kappa x} + b_2 e^{-j\kappa x} \quad (2.30)$$

$$u_3(x) = a_3 e^{j\kappa x} + b_3 e^{-j\kappa x} \quad (2.31)$$

where  $\kappa$  is the wave vector,  $a_k, b_k$  are mode related constants and  $k = 1, 2, 3$ . Notice that  $\kappa$  and  $a_k, b_k$  have different values for different layers. Substitute (2.29-2.31) to (2.21-2.23), the dispersion relation can then be derived as below

$$\begin{vmatrix} \overline{C_{11}} - \rho \frac{\omega^2}{\kappa^2} & \overline{C_{12}} & \overline{C_{13}} \\ \overline{C_{21}} & \overline{C_{22}} - \rho \frac{\omega^2}{\kappa^2} & \overline{C_{23}} \\ \overline{C_{31}} & \overline{C_{32}} & \overline{C_{33}} - \rho \frac{\omega^2}{\kappa^2} \end{vmatrix} = 0 \quad (2.32)$$

The dispersion relation is obviously depend on the stiffened viscoelastic constants. C-axis vertical AlN and ZnO piezoelectric films have hexagonal structures that are elastically and electrically isotropic in the lateral  $x, y$  plane. All the undiagonal terms in (2.32) are equal to zero by substituting equation (2.28) and data from Appendix IV. Then the first two solutions are two unstiffened shear waves with dispersion relation

$$\overline{c}_{44} \kappa_s^2 = \rho \omega^2 \quad (2.33)$$

where

$$\overline{c}_{44} = \overline{C}_{11} = \overline{C}_{22} = c_{44} + \frac{e_{14}e_{41}}{\epsilon_{11}} = c_{44} \quad (2.34)$$

and the third solution is a stiffened longitude wave with dispersion relation

$$\overline{c}_{33} \kappa_l^2 = \rho \omega^2 \quad (2.35)$$

where

$$\bar{c}_{33} = \bar{C}_{33} = c_{33} + \frac{e_{33}e_{33}}{\varepsilon_{33}} \quad (2.36)$$

From equation (2.24) and Appendix IV, the electrical potential is then given by

$$\phi(x) = \frac{e_{33}}{\varepsilon_{33}} u_3 + \xi x + \eta \quad (2.37)$$

There is no stiffened shear mode which is shown in the one-dimensional case with a perfect c-axis vertical AlN film. However, this is not suitable to one-dimensional c-axis tilt or non-homogenous AlN films since all the undiagonal terms in the dispersion equation (2.32) are now not equal to zero. Stiffened shear mode is usually observed for those TFRs located at the wafer edge where aluminum nitride is deposited in a tilted angle towards the Si substrate. Stiffened shear modes may be also created in a two or three-dimensional device geometry since more complicated boundary conditions, especially lateral stress and electrode-edge evanescent field, may produce considerable shear strains. A two-dimensional analysis will be used in the next section to compare with the one-dimensional analysis.

The boundary conditions are that the traction force of normal components and wave velocities are continuous across the interface between layers, and traction-free on the top and bottom surfaces since air is encountered there. These boundary conditions can be written as:

at  $x = 0$ , stress-free

$$T_{3j} \Big|_{x=0} = 0 \quad (2.38)$$

at  $x = h_b$ , stress and velocity continue

$$T_{3j, b} \Big|_{x=h_b} = T_{3j, f} \Big|_{x=h_b} \quad (2.39)$$

$$u_{3j, b} \Big|_{x=h_b} = u_{3j, f} \Big|_{x=h_b} \quad (2.40)$$

$$\phi \Big|_{x=h_b} = 0 \quad (2.41)$$

at  $x = h_f$ , stress and velocity continue

$$T_{3j, f} \Big|_{x=h_f} = T_{3j, t} \Big|_{x=h_f} \quad (2.42)$$

$$u_{3j, f} \Big|_{x=h_f} = u_{3j, t} \Big|_{x=h_f} \quad (2.43)$$

$$\phi \Big|_{x=h_f} = V \quad (2.44)$$

at  $x = h_t$ , stress and velocity continue

$$T_{3j, t} \Big|_{x=h_t} = T_{3j, c} \Big|_{x=h_t} \quad (2.45)$$

$$u_{3j, t} \Big|_{x=h_t} = u_{3j, c} \Big|_{x=h_t} \quad (2.46)$$

at  $x = h_c$ , stress free

$$T_{3j} \Big|_{x=h_c} = 0 \quad (2.47)$$

The sub-notations  $b, f, t, c$  present the bottom-electrode, piezo-film, top-electrode, and analyte coating. Since only longitude mode is piezoelectrically stiffened, so sub-notation  $j$  is actually equal to 3. By combining equation (2.23-2.24), (2.27-2.28), (2.31), with the above boundary conditions, a complete wave

analysis can be conducted. The resulting 8 x 8 linear equations can be stacked in a matrix formula

$$[A] \cdot [X] = [B] \quad (2.48)$$

where

$$[X] = [a_b \ a_f \ b_b \ \xi_f \ \eta_f \ a_t \ b_t \ a_c]^T \quad (2.49)$$

$$[B] = [0 \ 0 \ 0 \ V \ 0 \ 0 \ 0 \ 0]^T \quad (2.50)$$

$$[A] = \begin{bmatrix} Q_{11} & Q_{12} & Q_{13} & 0 & 0 & 0 & 0 & 0 \\ Q_{21} & Q_{22} & Q_{23} & Q_{24} & 0 & 0 & 0 & 0 \\ 0 & Q_{32} & Q_{33} & Q_{34} & Q_{35} & 0 & 0 & 0 \\ 0 & Q_{42} & Q_{43} & 0 & 0 & Q_{46} & Q_{47} & 0 \\ 0 & Q_{52} & Q_{53} & Q_{54} & 0 & Q_{56} & Q_{57} & 0 \\ 0 & Q_{62} & Q_{63} & Q_{64} & Q_{65} & 0 & 0 & 0 \\ 0 & 0 & 0 & 0 & 0 & Q_{76} & Q_{77} & Q_{78} \\ 0 & 0 & 0 & 0 & 0 & Q_{86} & Q_{87} & Q_{88} \end{bmatrix} \quad (2.51)$$

where

$$Q_{11} = e^{j\kappa_b h_b} + e^{-j\kappa_b h_b}, \quad Q_{12} = -e^{j\kappa_f h_b}, \quad Q_{13} = -e^{j\kappa_f h_b}$$

$$Q_{21} = jc_b \kappa_b (e^{j\kappa_b h_b} - e^{-j\kappa_b h_b}), \quad Q_{22} = -jc_f \kappa_f e^{j\kappa_f h_b}, \quad Q_{23} = jc_f \kappa_f e^{-j\kappa_f h_b},$$

$$Q_{24} = -e_f$$

$$Q_{32} = \frac{e_f}{\varepsilon_f} e^{j\kappa_f h_b}, \quad Q_{33} = \frac{e_f}{\varepsilon_f} e^{-j\kappa_f h_b}, \quad Q_{34} = h_b, \quad Q_{35} = 1$$

$$Q_{42} = e^{j\kappa_f h_f}, \quad Q_{43} = e^{-j\kappa_f h_f}, \quad Q_{46} = -e^{j\kappa_i h_f}, \quad Q_{47} = -e^{-j\kappa_i h_f}$$

$$Q_{52} = jc_f \kappa_f e^{j\kappa_f h_f}, \quad Q_{53} = -jc_f \kappa_f e^{-j\kappa_f h_f}, \quad Q_{54} = e_f, \quad Q_{56} = -jc_i \kappa_i e^{j\kappa_i h_f},$$

$$\begin{aligned}
Q_{57} &= jc_t \kappa_t e^{-j\kappa_t h_t} \\
Q_{62} &= \frac{e_f}{\varepsilon_f} e^{j\kappa_f h_f}, \quad Q_{63} = \frac{e_f}{\varepsilon_f} e^{-j\kappa_f h_f}, \quad Q_{64} = h_f, \quad Q_{65} = 1 \\
Q_{76} &= e^{j\kappa_t h_t}, \quad Q_{77} = e^{-j\kappa_t h_t}, \quad Q_{78} = -e^{j\kappa_t h_t} - e^{-j\kappa_t h_t} \cdot e^{2j\kappa_t h_t} \\
Q_{86} &= jc_t \kappa_t e^{j\kappa_t h_t}, \quad Q_{87} = -jc_t \kappa_t e^{-j\kappa_t h_t}, \\
Q_{88} &= -jc_c \kappa_c e^{j\kappa_c h_c} + jc_c \kappa_c e^{-j\kappa_c h_c} \cdot e^{2j\kappa_c h_c} \\
V &\text{ is the applied RF voltage}
\end{aligned}$$

After the coefficient matrix is solved, other parameters such as displacement, stress, potential can be directly obtained by substituting these coefficients back into equation (2.31), (2.27), (2.37). The electrical flux density can be derived, by substituting equation (2.37) for (2.4), as

$$D_3 = \varepsilon_{33} \frac{\partial u_3}{\partial x} - \varepsilon_{33} \frac{\partial \phi}{\partial x} = -\varepsilon_{33} \xi_f \quad (2.52)$$

The one-port input admittance can then be derived as

$$Y_{in} = \frac{I}{V} = \frac{\int_A \vec{J} \cdot d\vec{s}}{V} = \frac{-j\omega \int_A \vec{D}_3 \cdot d\vec{s}}{V} = \frac{j\omega D_3 A}{V} = \frac{j\omega \varepsilon_{33} A \xi_f}{V} \quad (2.53)$$

where

$$\varepsilon_{33} = \varepsilon_f$$

$$e_{33} = e_f$$

From the above derivation, TFR input admittance depends on all the parameters contributed from each layers. This analysis can be used to investigate not only mass loading, but also viscoelastic effects for each layer. For TFR shear mode devices, a

similar analysis can be conducted except that the longitudinal module is replaced by the shear modules. This analysis can be easily extended to QCM cases. For example, AT-QCM is a Y-cut quartz rotated an angle of 35.25 clockwise about the  $x_1$  axis. To stay consistent with standard AT-quartz notation, the thickness direction is now set in the  $x_2$  direction. By applying matrix transformation, The similar results for QCMs can be obtained by substituting the governing parameters  $e_{33}, \epsilon_{33}, c_{33}$  with shear wave module  $e_{26}, \epsilon_{22}, c_{66}$  as illustrated in Figure 1.4. Figure 2.2 shows the longitudinal displacement across the TFR composite in which a large displacement field is found in two reflected surfaces and a minimum is inside the AlN film. Waves are totally reflected from two surfaces because of traction-free boundaries. Figure 2.3 shows the relationship between the displacement field at the top-electrode/coating interface and the swept frequency. It is obvious that the largest

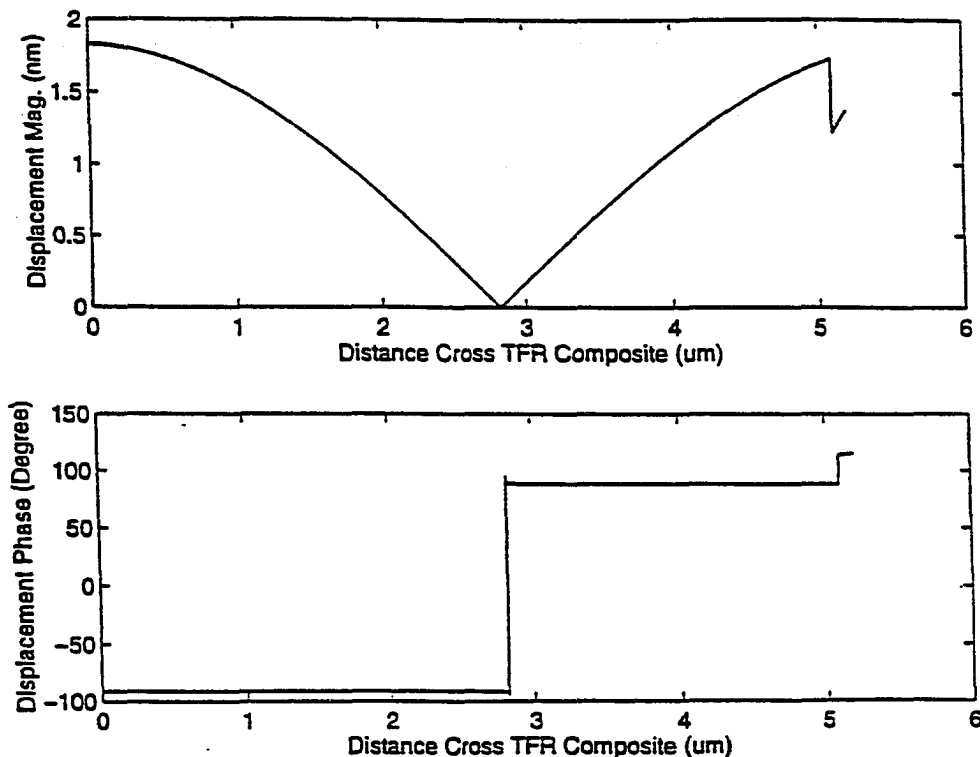


Figure 2.2 Displacement across TFR composite

displacement occurs at the resonance. However, the displacement magnitude is fair small compared to metal electrode or coating thickness. Layer thicknesses used in this calculation are  $0.1\ \mu\text{m}$  for AlCr-bottom-electrode,  $5.5\ \mu\text{m}$  for aluminum nitride film,  $0.05\ \mu\text{m}$  for AuCr-top-electrode and  $0.1\ \mu\text{m}$  for PdNi-coating. The standard elastic constants of these metals are listed in Appendix IV. The excitation voltage and device area are one volt and  $400\ \mu\text{m}^2$ , respectively. The modeled results for longitude-mode, shear-mode TFR and QCM are showed in Figure 2.4-2.6. The frequency ratio of longitude- to shear-TFR is calculated to be 0.55. The perturbing effects from each layer are apparently shown. The gas or vapor absorption may vary with coating thickness, density, and viscoelastic properties. This analysis can then be used to investigate those effects individually or combined. The material parameters used in analysis such as permittivity, elastic and piezoelectric tensors can be found from Appendix IV.

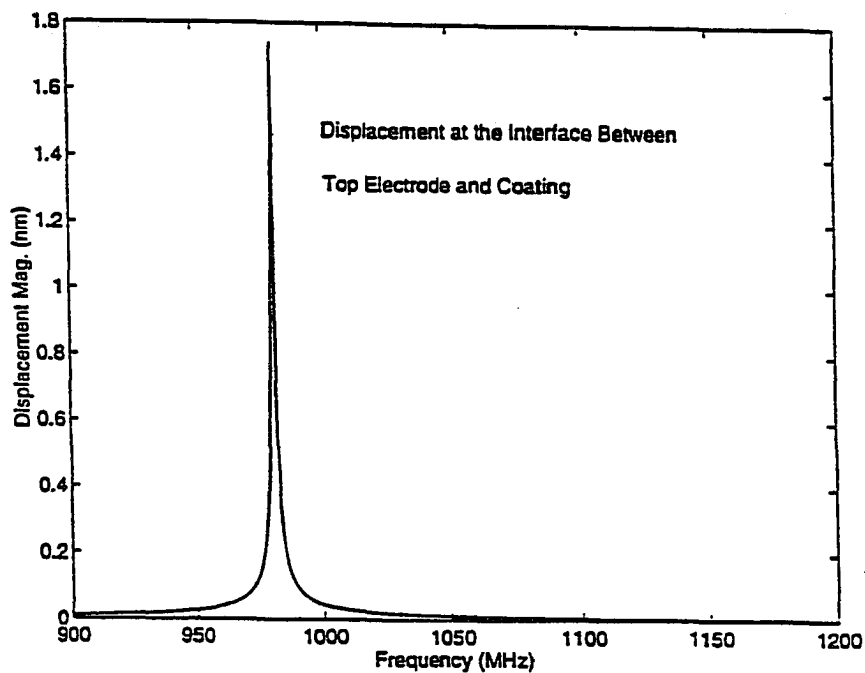


Figure 2.3 Displacement magnitude vs. frequency

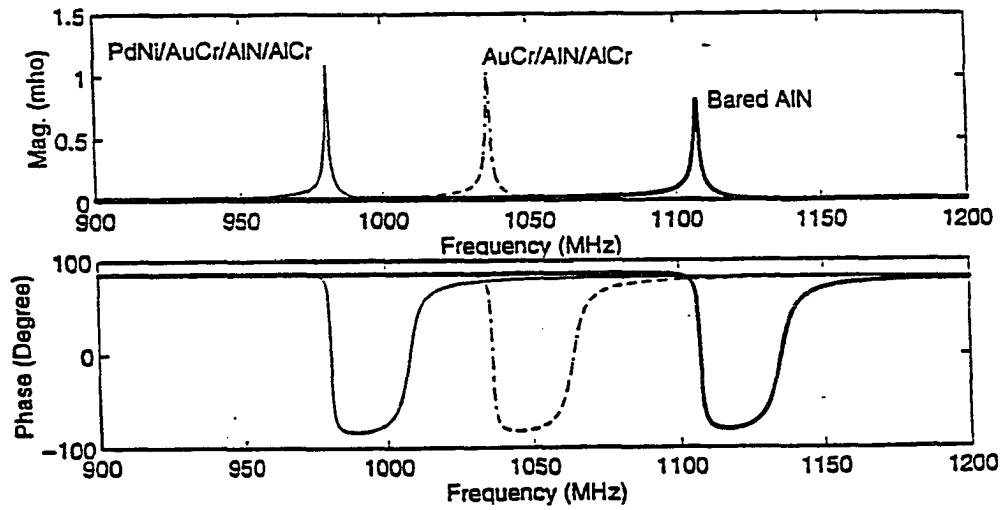


Figure 2.4 Modeled longitude-mode TFR responses

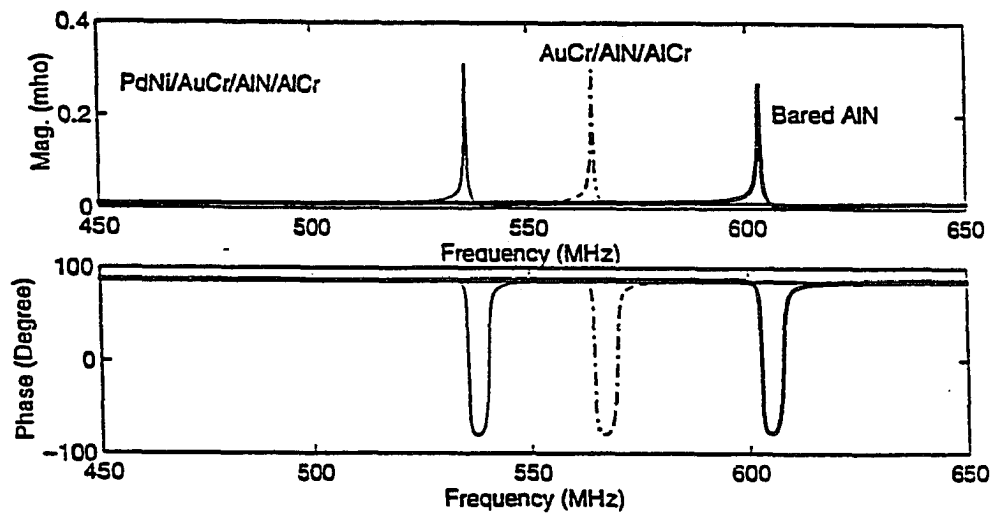


Figure 2.5 Modeled shear-mode TFR responses

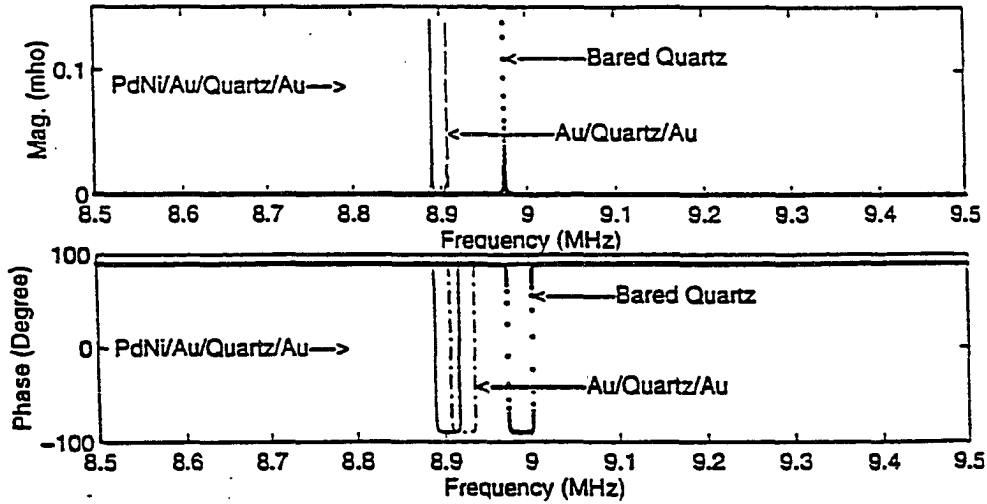


Figure 2.6 Modeled shear-mode QCM responses

#### Two-dimensional Device Analysis

As described above, TFR devices have both longitude and shear strain because of the elastic properties of the sputtered AlN film. The coupling nature between shear and longitude strain may create other modes within the operation frequency. Before applying the one-dimensional analysis to characterize polymer or liquid response, a two-dimensional finite difference method (FDM) is thus used to evaluate other possible modes and the validity of the one-dimensional analysis.

To consider a two-dimensional case, no variation on  $x_2$  direction is assumed. Then the general two-dimensional coupled PDE and constitutive relations can be written as following from (2.9-2.12),

$$A_{jk} \frac{\partial^2 u_k}{\partial x_1^2} + C_{jk} \frac{\partial^2 u_k}{\partial x_3^2} + (H_{jk} + I_{jk}) \frac{\partial^2 u_k}{\partial x_1 \partial x_3} = \lambda_j u_j \quad (2.54)$$

where

$$\lambda_j = -\rho\omega^2 \quad j = 1, 3$$

$$\lambda_j = 0 \quad j = 4$$

$$u_4 = \phi$$

### Stress

$$T_{1j} = A_{jk} \frac{\partial u_k}{\partial x_1} + H_{jk} \frac{\partial u_k}{\partial x_3} \quad (2.55)$$

$$T_{3j} = I_{jk} \frac{\partial u_k}{\partial x_1} + C_{jk} \frac{\partial u_k}{\partial x_3} \quad (2.56)$$

A nine-point scheme<sup>41,42</sup> in which the mesh is generated as shown in Figure 2.7 is implemented in the FDM. The calculation geometry is shown in Figure 2.8, with a c-axis vertical AlN film of  $5\mu$  nominal thickness. A pair of infinitely thin electrodes is

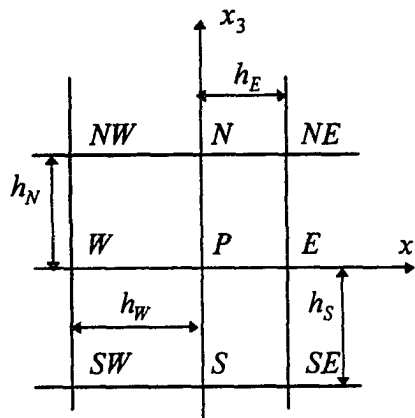


Figure 2.7 Nine-point mesh scheme

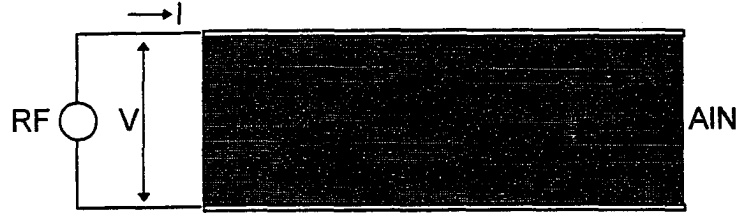


Figure 2.8 FDM mesh geometry

also assumed in the calculation. To reduce calculation errors, all the mesh spaces are equally chosen. The difference equation of PDE and traction forces (equation 2.54-2.56) can be expressed as

$$Y^E(j,k)u_k^E + Y^W(j,k)u_k^W + Y^N(j,k)u_k^N + Y^S(j,k)u_k^S + Y^{SE}(j,k)u_k^{SE} + Y^{SW}(j,k)u_k^{SW} + Y^{NE}(j,k)u_k^{NE} + Y^{NW}(j,k)u_k^{NW} + Y^P(j,k)u_k^P = 0 \quad (2.57)$$

$$T_{1j} = Y_1^E(j,k)u_k^E + Y_1^W(j,k)u_k^W + Y_1^N(j,k)u_k^N + Y_1^S(j,k)u_k^S + Y_1^P(j,k)u_k^P \quad (2.58)$$

$$T_{3j} = Y_3^E(j,k)u_k^E + Y_3^W(j,k)u_k^W + Y_3^N(j,k)u_k^N + Y_3^S(j,k)u_k^S + Y_3^P(j,k)u_k^P \quad (2.59)$$

here  $Y^{xx}(j,k)$ ,  $Y_1^{yy}(j,k)$ ,  $Y_3^{yy}(j,k)$  are functions of material viscoelasticity, piezoelectricity and permittivity at mesh points and shown in Appendix V.  $xx$  represents  $E, W, S, N, SE, SW, NE, NW$  points.  $yy$  represents  $E, W, S, N$  points. Mass density has been included in  $Y^P(j,k)$  of center mesh point. The Lloyd approach is implemented in the corner of device geometry because of the discontinuity of stress at these points.<sup>42</sup>

Figure 2.9 - 2.10 shows the modeled two-dimensional TFR responses. Both thickness-longitude and thickness-shear mode have been shown with the frequency

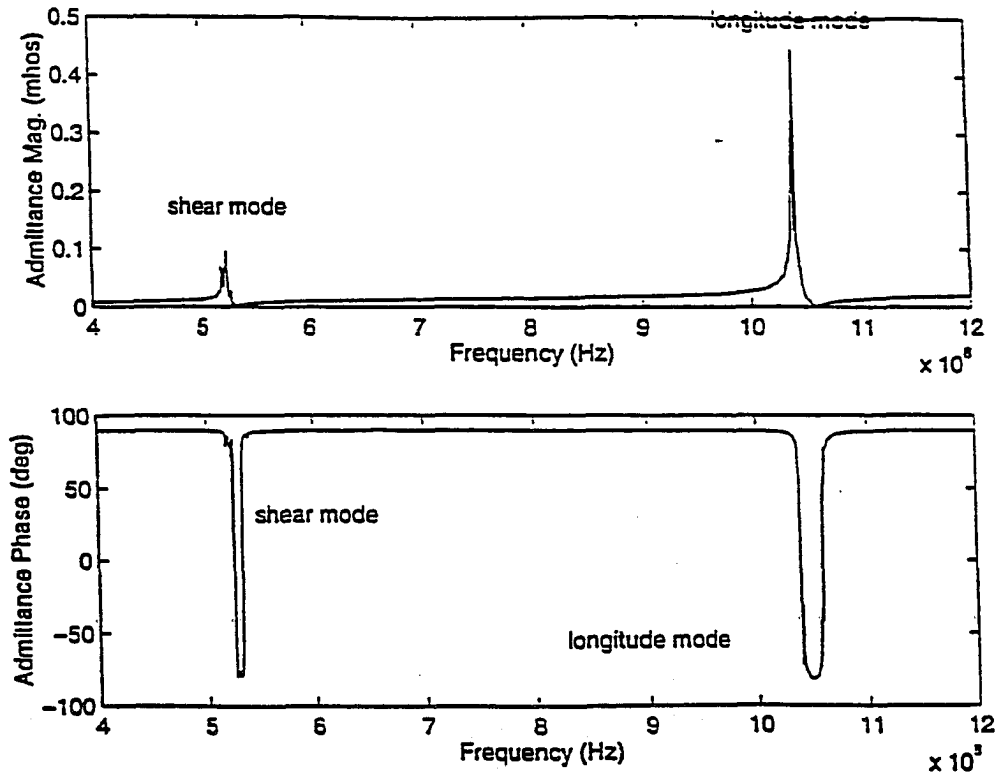


Figure 2.9 2D/FDM simulation of TFR admittance

ratio of shear mode to longitude mode to be about 0.52. This compares closely with the one-dimensional (frequency ratio  $\sim 0.55$ ) and implies that, under well-grown AlN film, weakly-piezoelectric coupling is satisfied. Therefore the one-dimensional model can be used to model TFR composite sensors with the acceptable accuracy. It was found that the calculation accuracy is very sensitive to how many mesh points are used and the data type of numerical calculation. Sixteen mesh points per wave length is usually required to ensure calculation accuracy. With the same number of mesh points, numerical calculation with double precision gives more accurate. A typical aluminum/TFR experimental response is shown in Figure 2.11. The frequency ratio of shear mode to longitude mode is about 0.54, which is in agreement with the models.

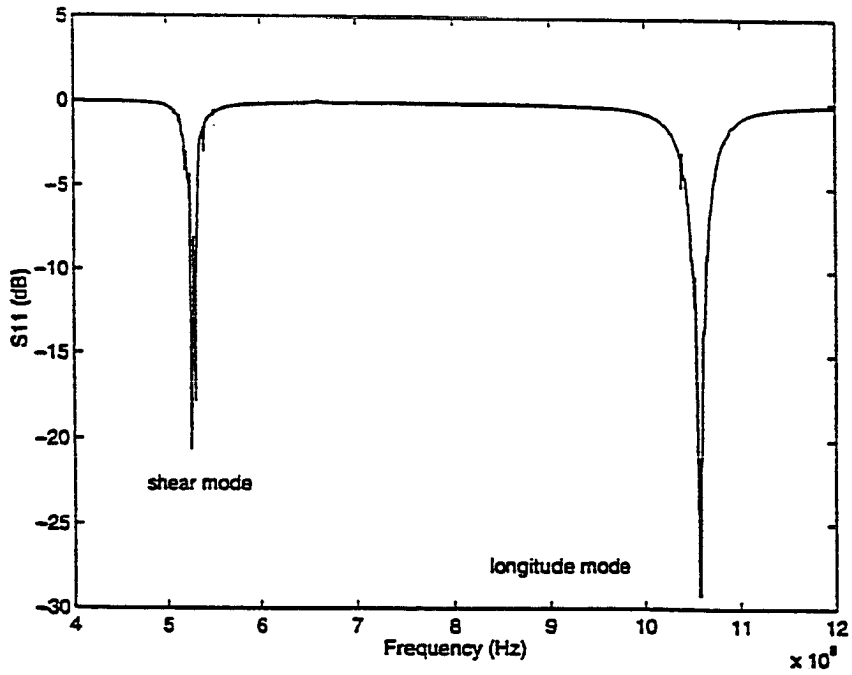


Figure 2.10 2D/FDM TFR return loss

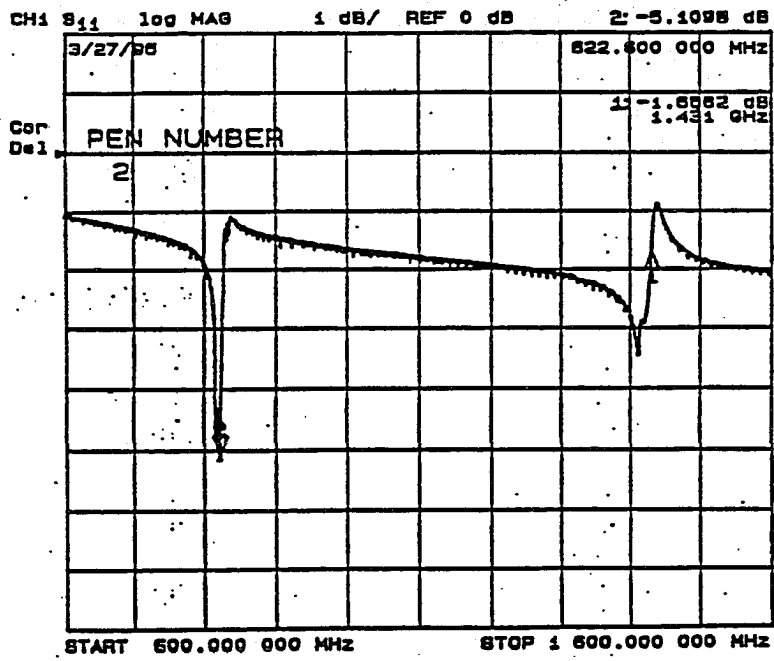


Figure 2.11 typical aluminum TFR measurement

### Wave Analysis in TFR Liquid

For TFRs in liquid applications, shear mode must be used. The TFR is passivated on one side to allow the electrode to contact the liquid as shown in Figure 2.7. Acoustic waves are generated by the applied electric field and radiate into the liquid at the solid/liquid boundary and attenuate with the propagation distance. The liquid velocity field can be determined by solving the Navier-Stokes equation for one-dimensional flow<sup>3</sup>

$$\eta_l \frac{\partial^2 v_z}{\partial x^2} = \rho_l \dot{v}_z \quad (2.60)$$

$$\dot{v}_z = \frac{\partial v_z}{\partial t} \quad (2.61)$$

where  $\rho_l$  and  $\eta_l$  are liquid density and shear viscosity, respectively. Rewriting

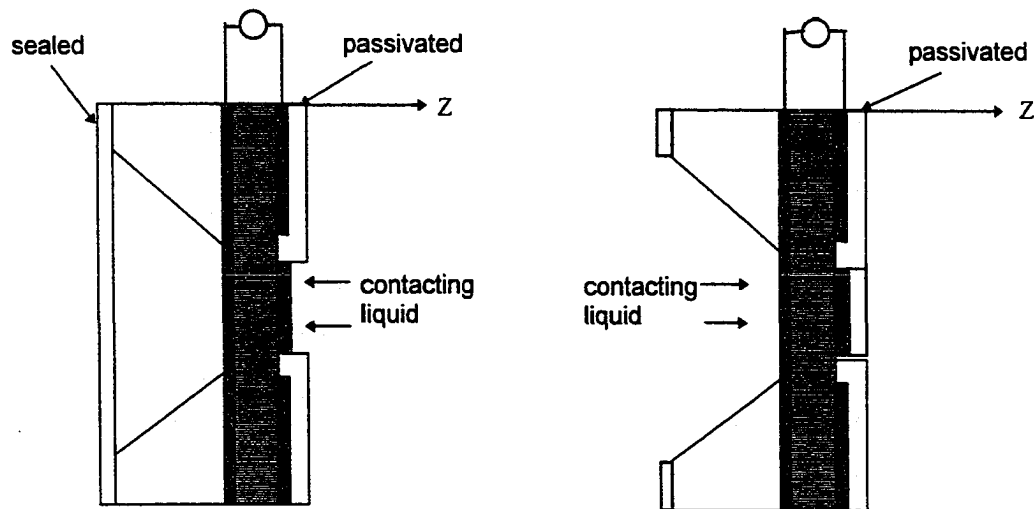


Figure 2.12 Two configurations of liquid-loaded TFR

(2.60) in time harmonic form gives

$$j\omega\eta_l \frac{\partial^2 u_z}{\partial x^2} = -\rho_l \omega^2 u_z \quad (2.62)$$

$$j\omega\eta_l \frac{\partial^2 u_z}{\partial x^2} = -\rho_l \omega^2 u_z \quad (2.62)$$

$$c_l \frac{\partial^2 u_z}{\partial x^2} = -\rho_l \omega^2 u_z \quad (2.63)$$

where  $c_l = j\omega\eta_l$ . Comparing (2.62) with (2.20), one shows that they are the same except that liquid does not have shear elastic properties. The solution of (2.63) should satisfy that  $u_z(x) \rightarrow 0$  as  $x \rightarrow \infty$ , and can be easily obtained as

$$u_z(x) = Ee^{-\gamma(x-h)} \quad (2.64)$$

where complex wave constant

$$\gamma = \left(\frac{\omega\rho_l}{\eta_l}\right)^{1/2} (1+j) \quad (2.65)$$

and wave decay length or skin depth is then

$$\delta_l = \left(\frac{2\eta_l}{\omega\rho}\right)^{1/2} \quad (2.66)$$

The wave analysis is the same as that in TFR-solid. Non-slip boundary condition is used. Although Kipling and Thompson suggest that the non-slip boundary may be

inappropriate with certain surface treatment,<sup>43</sup> the non-slip assumption was used and verified by Martin et al. in QCM liquid applications.<sup>3</sup> The non-slip velocity condition, in this author's opinion, is also valid in TFR analysis for the following reasons. First the deposited metal surface is relatively smooth compared to the decay length of the damped shear wave, which ensures generation of plane-parallel flow in the liquid. Secondly, under high operation frequency, liquid may behave as viscoelastic fluid with adequate wetting of the TFR surface. The continuity of displacement in the TFR surface can be roughly satisfied. The modeled frequency shift and magnitude damping are shown in Figure 2.13-2.14. The TFR is assumed to have 5  $\mu\text{m}$  thickness of aluminum nitride and sandwiched by 0.1  $\mu\text{m}$  gold metals.

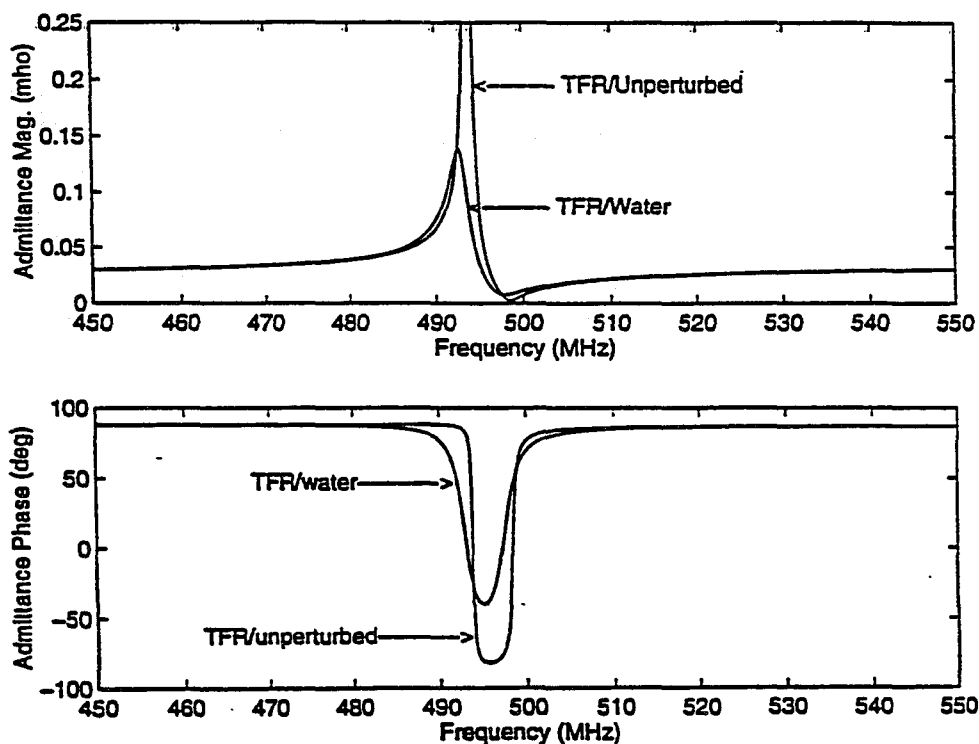


Figure 2.13 TFR admittance vs water-loading

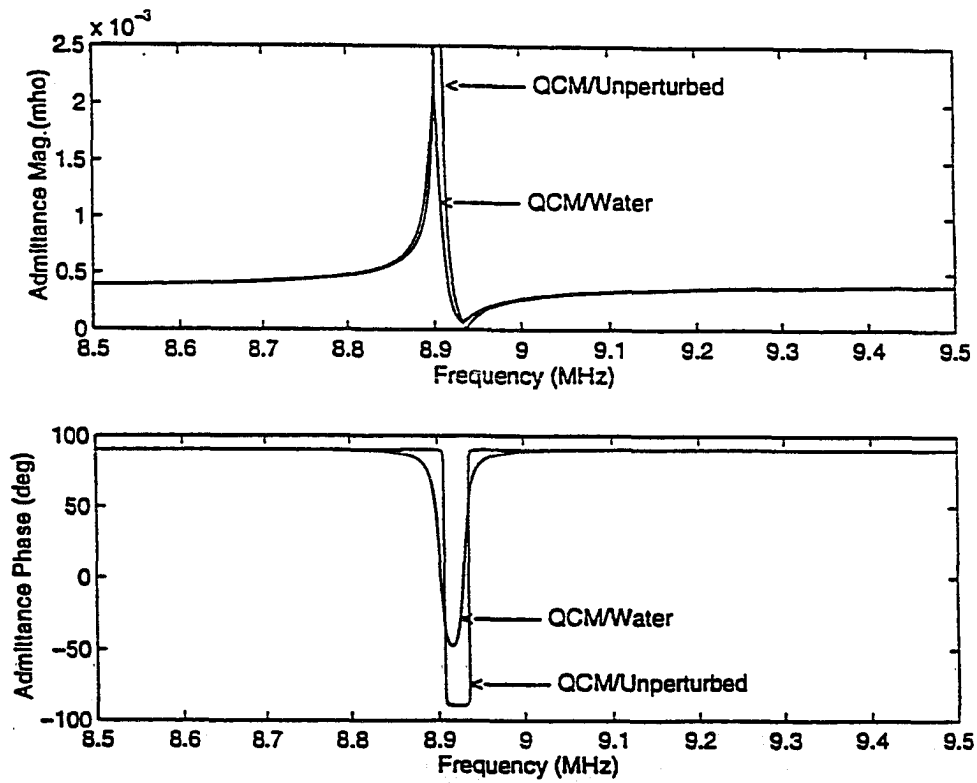


Figure 2.14 QCM admittance vs. water-liquid

Table 2.2 Modeled QCM, TFR responses in water

## QCM

	Fs (MHz)	Qs	Rs (ohms)	Ls (mH)	Cs (fF)
Air	8.9072	57700	7.1	7.3	43.57
Water	8.9029	747	527.3	7	45.42

## TFR

	Fs (MHz)	Qs	Rs (ohms)	Ls (mH)	Cs (fF)
Air	493.7822	2026	1	0.57	181.6
Water	493.0972	206	8	0.53	196.2

Typical 9 MHz QCM parameters are used in the QCM calculation. The decay length of QCM in water at room temperature is about  $0.186 \mu\text{m}$ . This value may shrink down to  $250 \text{ \AA}$  if a typical 500 MHz shear-TFR is used. The changes of resonant parameters by water-loading are listed in Table 2.2. The frequency shifts in water are about 4.3 KHz and 685 KHz for QCM and TFR respectively. Figure 2.15 shows the responses due to liquid loading. It is expected that the frequency shift and admittance magnitude damping become large with increasing liquid viscosity and density.

This analysis shows that the TFR can be also applied in liquid phase, and should be more sensitive to the viscosity and density of the contacting solution than the QCM. TFR shear devices can then be used as microsensors in many potential

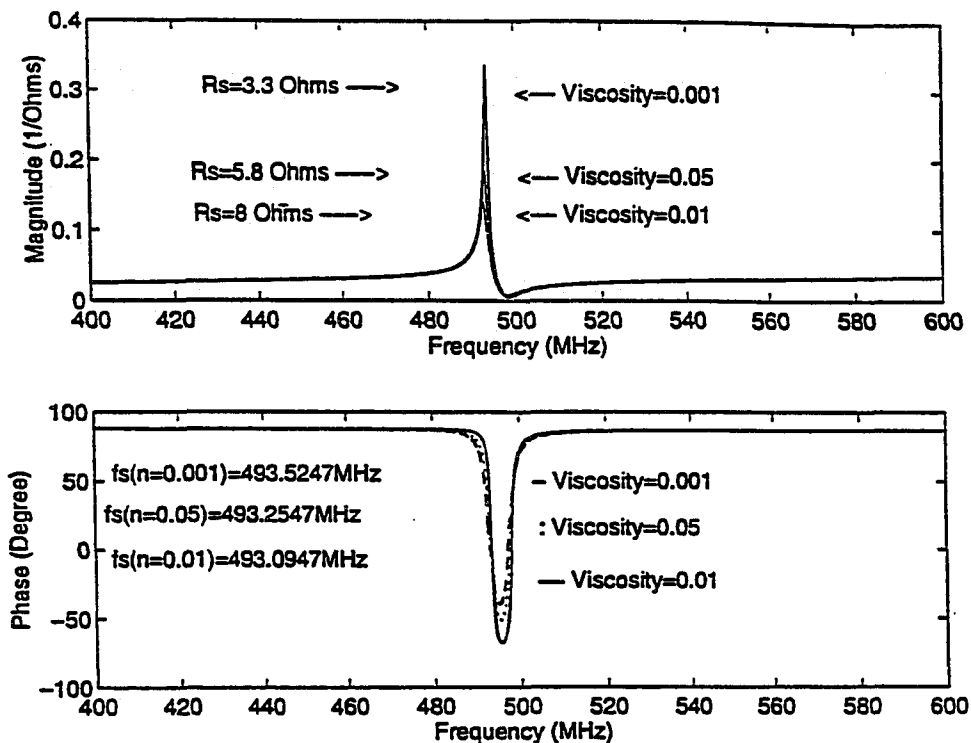


Figure 2.15 TFR responses due to different liquids

areas such as species detection, liquid chromatographic detection, electrochemical analysis and biological applications. The parameters of interest parameters such as liquid viscosity and density can be measured by the resonant frequency shift, phase change and magnitude damping. Another interesting application is that it is possible to simultaneously detect mass and liquid loading by sweeping the TFR frequency range, covering both shear and longitude modes.

### CHAPTER 3. POLYMER-COATED, LIQUID-COATED TFR ANALYSIS AND CHARACTERIZATION

The computer modeling for this analysis utilizes wave analysis from Chapter 2, in which the resonant parameters are extracted by a fundamental differential approach. To be consistent with standard resonator calculation and HP resonator software,<sup>44</sup> the series resonant frequency ( $f_s$ ) is defined as the frequency at which the motional conductance is the maximum. The directly measured series frequency from a network analyzer,  $f_r$ , is the series frequency at which the phase of measured  $S_{11}$  is zero.  $f_s$  should not be confused with  $f_r$ , which is the series resonant frequency of the whole circuit.  $f_s$  includes the motional admittance paralleled with the TFR static capacitor ( $C_o$ ) and other parasitic elements from bonding-pad, bonding wire and test fixture. The static capacitor and parasitic elements offset the  $f_r$  with  $f_s$  as shown in Figure 3.1. In contrast to the low-frequency QCM, the measured admittance locus for TFRs is usually not a well-defined circle. High frequency spurious circulars are often observed. The motional resistance is then calculated from the diameter of the best fit circle in the admittance plane. At series resonance, the motional inductance can then be calculated from the

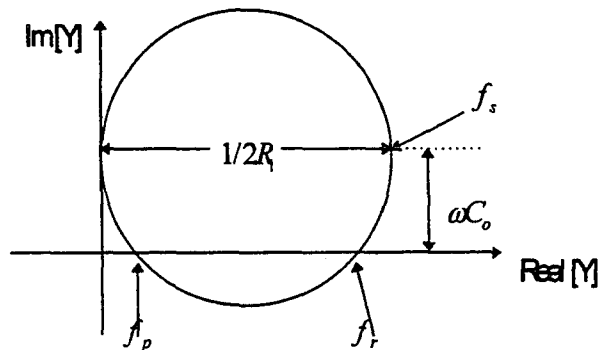


Figure 3.1 Admittance Plane of one-port TFR/QCM Resonators

reactance expression by using the different approach as:

$$L_1 = \frac{1}{4\pi} \left. \frac{\partial X}{\partial f} \right|_{f=f_s} \quad (3.1)$$

The central difference approach is used to calculate the first derivative of reactance as<sup>44</sup>:

$$\left. \frac{\partial X}{\partial f} \right|_{f=f_s} = \frac{X(f_s - 2\Delta f) - 8X(f_s - \Delta f) + 8X(f_s + \Delta f) - X(f_s + 2\Delta f)}{12\Delta f} \quad (3.2)$$

where  $\Delta f = \frac{\text{Sweep Frequency Range}}{\text{data samples} - 1}$ . Other parameters of interest are the motional capacitor  $C_1$ , and the quality factor  $Q$ . They can now be calculated as:

$$C_1 = \frac{1}{\omega_s^2 L_1} = \frac{1}{(2\pi f_s)^2 L_1} \quad (3.3)$$

$$Q = \frac{\omega_s L_1}{R_1} = \frac{1}{2\pi f_s C_1 R_1} \quad (3.4)$$

From (3.4), we can see that the  $Q$  depends on not only the motional resistance, but also the dynamic motional inductance or capacitance at series resonance.

The reason for choosing  $f_s$  instead of  $f_r$  is that  $f_s$  directly relates to the acoustic effects where analyte absorption and desorption can be dynamically interpreted, and which is important for understanding coating acoustic, chemical and physical changes by analyte absorption and desorption. Other techniques, such as measuring the S-parameter can also be used to characterize resonant

parameters.<sup>45</sup> The static capacitance ( $C_0$ ) and parasitic elements of the TFR can be characterized by S-parameter measurements.

The analysis has been focused on resonant characteristics varied by coating properties such as mass, thickness and viscoelasticity. Depending on the application, these properties are changed either by absorption of gas or vapor molecules, or by liquid contact. Mass absorption is usually observed at low analyte concentration, while thickness expansion and viscoelastic variation may occur in high analyte concentration or temperature-dependence applications. Changes of these acoustic properties rely on not only the acoustic devices used, but also the operation frequency, temperature and the interaction between analyte and coating, which makes theoretical prediction difficult. Several assumptions are thus made to perform the model analysis. Firstly, all the interfaces and surfaces are assumed planar. Wave scattering and mode generation from the rough surface will not be considered. Secondly, it is assumed that the electrodes adhere well to the aluminum nitride film and no electrical, dielectric and acoustic changes are caused by the electrode and AlN film during analyte absorption and desorption. Finally, the absorbed analyte is assumed to be uniformly distributed across the coating layer whether by physical absorption or by chemical bonding. In other words, the analyte will diffuse into the bulk of coating. In fact, these assumptions can be realized by well-controlled processing and measurement setup. The devices used in this analysis are polymer-coated TFRs, and liquid-coated TFRs.

#### Polymer-coated TFR Analysis and Characterization

With the first use of quartz resonator vapor polymer sensors by King,<sup>46</sup> and SAW polymer sensor by Wohltjen,<sup>5</sup> many applications have been recently explored, especially in SAW polymer sensors. However, few applications have been examined for TFR polymer sensors. TFRs work in a much high frequency range than QCM/TSM devices and have different characterization configuration than SAW devices, which may result in different dynamic response. In this section, the

resonant behavior of polymer-coated TFRs is investigated. Both longitude and shear mode are examined. One-dimensional wave analysis is applied with the actual device dimension. The thicknesses of the bottom electrode (Cr/Al), aluminum nitride film and top electrode (Cr/Au/PdNi) are 0.15  $\mu\text{m}$ , 5.5  $\mu\text{m}$ , and 0.15  $\mu\text{m}$ , respectively. The film thickness is chosen to be close to actual device data. The polymer thickness is chosen not to be close to the 'film resonance region', in which elastic energy is mostly coupled to the coating and severely damped. The acoustic phase across the polymer can be characterized as:

$$\phi_{\text{polymer}} = \text{Real}(\omega h_c \sqrt{\frac{\rho_c}{c_c + j\omega\eta_c}}) \quad (3.5)$$

where  $h_c$ ,  $\rho_c$ ,  $c_c$ ,  $\eta_c$  are polymer thickness, density, elastic constant and viscous constant, respectively. If a polymer is acoustically thin at high frequency and remains under isothermal conditions, polymers of either rigid or rubbery states usually behave as glassy films with elastic constant or bulk elastic modulus on the order of  $10^{10} \text{ Nm}^{-2}$ .<sup>6</sup> However, the polymer state may be varied by temperature or analyte absorption if the polymer film is acoustically thick. Polymer film resonance is defined as the point when the wave phase across the polymer reaches 90 degree.<sup>10</sup> At this point, the elastic energy of the resonator is coupled to the polymer from substrate TFR and damped away. The thickness of film resonance for common used materials are shown in Table 3.1. Film resonance most easily occurs in rubbery films where wave velocities are low. Thin polymer films at QCM frequency range are probably very thick at TFR frequency range. Film resonance may also occur in metal electrodes if thick metallization is used. The physical concept behind film resonance can be explained clearly if one investigates the wave reflection at the interface between polymer and substrate resonator. The wave reflection

Table 3.1 Film resonant thickness

	film resonance thickness at 1 GHz	film resonance thickness at 9 MHz
rubbery polymer	0.08 $\mu\text{m}$ ( small viscosity)	0.8 $\mu\text{m}$ ( small viscosity)
	0.8 $\mu\text{m}$ ( larger viscosity)	1.2 $\mu\text{m}$ ( large viscosity)
glassy polymer	0.7 $\mu\text{m}$	28 $\mu\text{m}$
Au metal	0.8 $\mu\text{m}$	80 $\mu\text{m}$
Pd metal	0.9 $\mu\text{m}$	90 $\mu\text{m}$
Al metal	1.6 $\mu\text{m}$	160 $\mu\text{m}$

coefficient  $\Gamma$ , by the analogue between acoustic and electromagnetic transmission line, can be expressed by the

$$\Gamma = \frac{Z_s - Z_t}{Z_s + Z_t} \quad (3.6)$$

where  $Z_s$  and  $Z_t$  are the input impedance seen at the resonator/film interface, and the characteristic impedance of top electrode of TFR,  $Z_t = \sqrt{\rho_t c_t}$ . The stress-free upper film surface is analogous to a short-circuit electrical termination. From this analogy,  $Z_s$  can be simply derived as,  $Z_s = jZ_c \tan(\kappa_c h_c)$ , where  $Z_c$  is the coating characteristic impedance,  $Z_c = \sqrt{\rho_c c_c}$ , and  $\kappa_c$  is the wave number of polymer,

$\kappa_c = \omega \sqrt{\rho_c / c_c}$ . The wave reflection coefficient can then be calculated as shown in

Figure 3.2, where the reflection coefficient reaches a minimum at a certain thickness, which indicating that a strong wave coupling occurs in the vicinity of film resonance. For glassy films, the storage component (elasticity) of elastic modulus has more effect on film resonance, while the loss component (viscosity) becomes dominant for very lossy rubbery films. The coupled energy from TFRs will be damped in polymer films, and the resonant performance of TFRs will be worse, which results in high resistance and low Q.

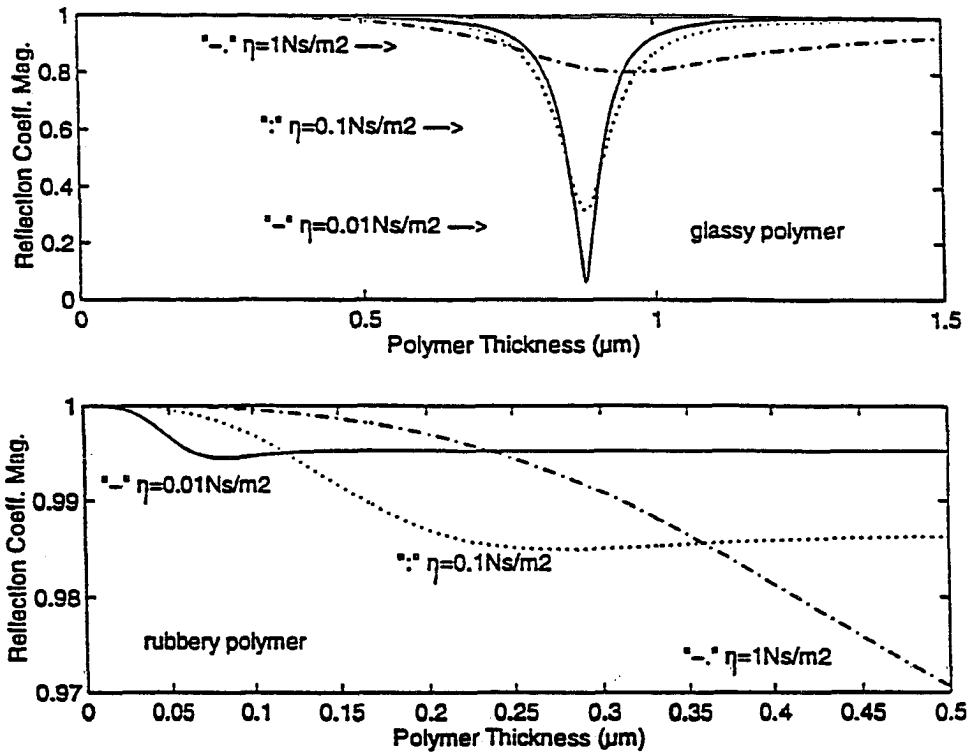


Figure 3.2 Wave reflection coefficients vs. polymer thickness

The absorption of gas or vapor molecules not only deposits mass in film, but also may expand the polymer volume (plasticization) and thus vary polymer film thickness. On the other hand, these low molecular weight analytes (comparison to polymer chain) may also cause dilution of polymer. The diluent molecules may be thought to arise from the addition of free volume and lower the effective viscosity and reduce polymer transition temperature.<sup>51</sup> If the polymer is acoustically thick, then the diluent absorbed analyte may also induce the cross-film displacement gradients which result in inertial displacement lag between the top surface and polymer-TFR interface (described in below). As described in Chapter 2, the frequency shift should now depend on both boundary (thickness expansion) and internal perturbation (mass and elastic module variation) if the electrical, dielectric and piezoelectric effects are negligible. For better understanding TFR polymer

operation, the comparison between physical thickness and acoustical thickness is first presented with the detailed derivation listed in Appendix VII. In order to be consistent with the conventions, elastic moduli are used in the analysis. Absorbed mass, thickness expansion and viscoelastic effects are then examined. Experimental characterization is finally analyzed and discussed.

#### Acoustically Thickness and Physical Thickness

The concept of acoustical thickness was first discussed by Martin in SAW polymer sensors.<sup>6</sup> He has found that the acoustical thickness depends not only on the polymer physical thickness, but also on the operation frequency and polymer intrinsic modulus properties. He found that polymer 'swelling' and elastic fluctuations usually occurred in an acoustically thick polymer film. These effects may become predominant if temperature is changed. In contrast to the wave mode and testing configuration in SAW devices, TFRs undergo different wave phenomena and thus may have different characteristics. Although most of the particle displacement in TFRs is either longitude or shear motion, quasi-longitude displacements in shear TFRs or quasi-shear displacement in longitude TFRs are usually found in actual devices based on aluminum nitride deposition conditions and device geometry. The ratio of polymer strains generated by cross-plane displacement gradients to those generated by in-plane gradients is derived as (appendix VI)

$$R = A \frac{\rho_c h_c}{|G_c|} f_c \quad (3.7)$$

where  $A$  is a constant related to TFR wave velocity and AIN properties,  $\rho_c$ ,  $h_c$ ,  $G_c$  are polymer density, physical thickness and shear modulus, respectively. When the polymer film is sufficiently thin (small physical thickness,  $h_c$ ), and rigid (large  $G_c$ ) in comparison to the operation frequency such that  $R \ll 1$ , in-plane gradients dominate over cross-plane gradients, and the film is acoustically thin. Polymer film

can vibrate simultaneously with the substrate TFR. When the film properties are such that  $R \geq 1$ , inertial lag of displacement of the top portion related to the polymer-substrate TFR interface becomes significant so that cross-plane gradients dominate, and film is acoustically thick. A 50 nm-thick polymer on 1 GHz TFR behaves as acoustically thin in the glassy state ( $G_c \approx 1.0 \times 10^{10} \text{ N/m}^2$ ), but behaves as acoustically thick in the rubbery state ( $G_c \leq 1.0 \times 10^8 \text{ N/m}^2$ ). A 0.5- $\mu\text{m}$ -thick polymer film on 1 GHz TFR behaves as acoustically thick even in the glassy state. The polymer states rely on individual polymer intrinsic elastic moduli, and their dependence on the applied frequency, temperature and absorbed analyte.

#### Mass Loading and Thickness Expansion

The mass loading effects characterized by Sauerybrey equation is valid for 2 % frequency shifts from the unloaded resonant frequency.<sup>5</sup> The basic assumption behind the equation is that the deposited film is located entirely within the whole region of the particle displacement of the resonator. The density of deposited layer is treated the same as the resonator itself. The frequency decreases when a polymer coating is applied. This is primarily due to mass change of a thin polymer layer. When an acoustic thin polymer is coated onto a longitude-TFR, and exposed to a vapor, the absorption of the vapor perturbs the polymer layer and resonant frequency normally decreases. In addition to the added analyte mass, polymer thickness may be also expanded. The film mass density and thickness varying with the concentration of absorbed analyte can be analyzed as:<sup>6</sup>

$$h(C) = h_0(1 + CV) \quad (3.8)$$

$$\rho(C) = \frac{\rho_0 + Cm}{1 + CV} \quad (3.9)$$

$$C = \frac{\Delta m_a \rho_0}{\Delta m_c m} \quad (3.10)$$

where  $C$  and  $CV$  are the analyte concentration (mol of sorbed vapor/mL of polymer) and expanded thickness.  $m$  and  $Cm$  are the analyte specific mass (g/mol) and absorbed analyte mass density.  $V$  is the specific volume of absorbed analyte (mL/mol).  $h_0$  and  $\rho_0$  are the pure polymer thickness and density.  $\Delta m_c$  and  $\Delta m_a$  are the polymer film mass and absorbed analyte mass. The amount of increased mass and thickness expansion are dependent on the polymer microstructure, surface condition, chemical affinity between polymer and analyte, and coating preparation method. From equation (3.8, 3.9), one can find that the polymer thickness is linearly expanded with analyte concentration, but density has a weak dependence on the concentration if the film has experienced thickness expansion. The typical elastic constant of a rubbery polymer is below  $10^8 \text{ N/m}^2$ , whereas that of a glassy polymer or a rubbery polymer at high frequency is usually about  $10^{10} \text{ N/m}^2$ . At room temperature and frequency above 1 MHz, nearly all rubbery polymers have measured module typical of polymer glass.<sup>6</sup> To understand the effects due to both mass and thickness expansion, Figure 3.3 shows the modeled series resonant parameters of a glassy polymer varied by film thickness and mass density. The polymer parameters used in calculation are density of 1230 kg/m<sup>3</sup> (polychloroprene), unloaded thickness of 0.18  $\mu\text{m}$  (weak acoustically thin,  $R \approx 0.35$ ), unloaded frequency of 810 MHz, elasticity of  $10^{10} \text{ N/m}^2$ , and viscosity of  $0.5 \text{ Ns/m}^2$ , respectively. Linear dependence of frequency on coating thickness and density can be observed. Frequency decreases about 80 KHz if the thickness or mass density is increased 1%. Figure 3.4 shows the same calculation with a three-dimensional dynamic plot of the motional parameters varied with polymer mass density and thickness. The motional resistance increases with both polymer thickness and density as expected, since the wave attenuation is proportional to the

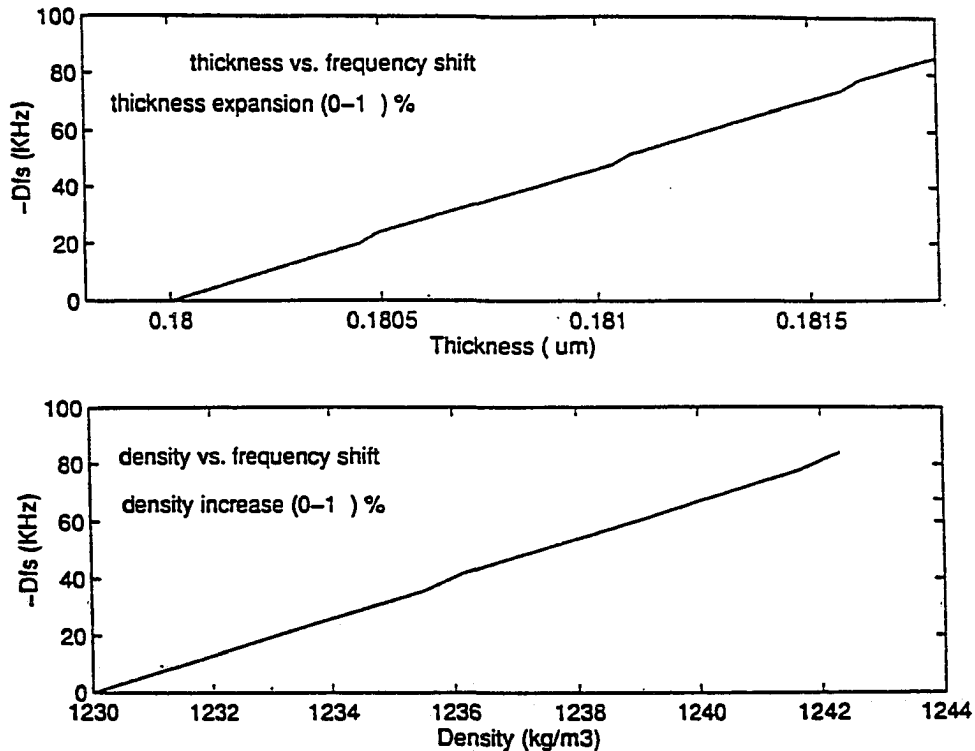


Figure 3.3 Modeled TFR frequency shift vs. polymer mass and thickness changes for an acoustically thin glassy polymer

product of thickness, the square root of both viscosity and density. The motional inductance increases while the motional capacitance decreases. This can be explained from the wave analogue between electromagnetic and acoustic waves. The additional motional inductance induced by the polymer film is proportional to the polymer mass. Pure mass layer benefits circuit Q. Unfortunately, this Q slightly increasing effect is totally compensated by polymer viscous damping, especially for TFR high frequency operation. At low analyte concentration and acoustically thin film, thickness expansion should not be expected large since a small amount of analyte mass is first absorbed in the vacancy sites of polymer film. Cross-chain mobility and film distortion resulting from analyte absorption should be small. The

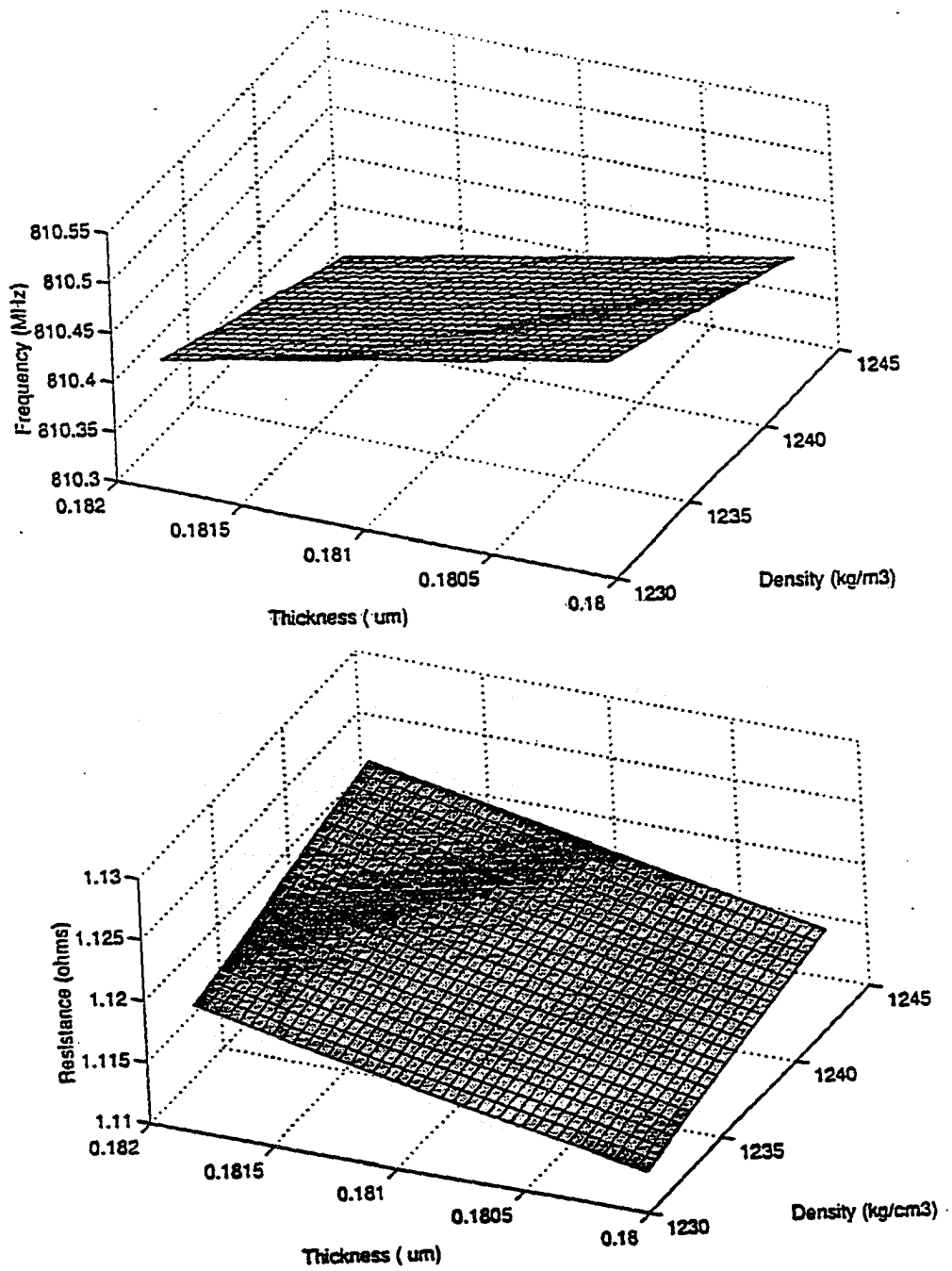


Figure 3.4 a) 3D plots of resonant frequency and motional resistance varied by thickness and mass density of an thin glassy polymer

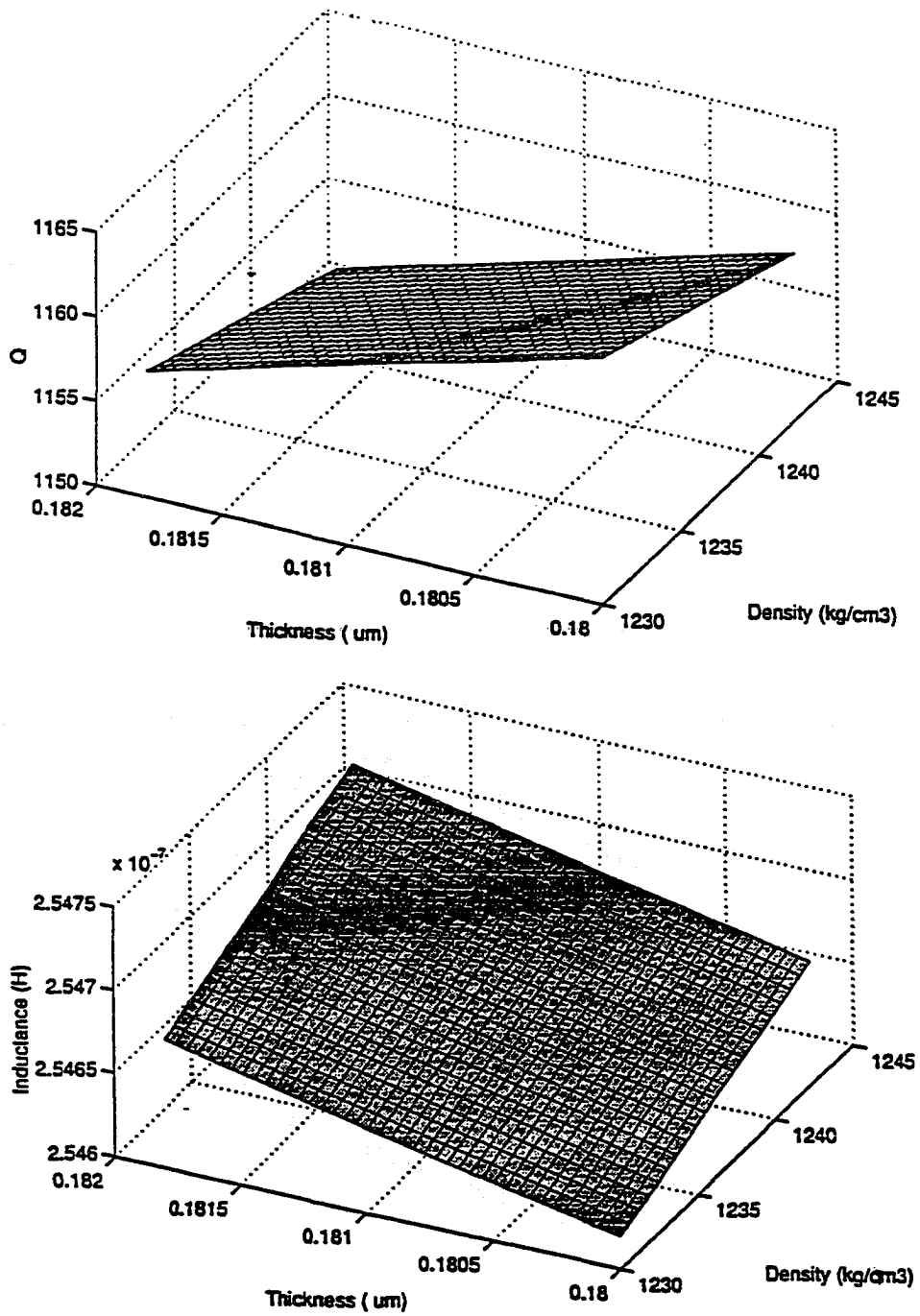


Figure 3.4 (continued) b) 3D plots of resonant Q and motional inductance varied by thickness and mass density of a thin glassy polymer

responses may be reasonably referred due to the absorbed mass -- mass loading effect. However, polymer volume expansion should be expected when analyte concentration becomes high, specially in an acoustically thick film. Then mass density effects should not dominate because a small mass increase effect by absorbed analyte may partially be compensated by the polymer expanded thickness (or volume). The modeled results for a rubbery polymer film (elasticity of  $10^7 \text{ N / m}^2$ , viscosity of  $0.5 \text{ Ns / m}^2$ ) are illustrated in Figure 3.5. To better illustrate the profound effects on film resonance, thickness is calculated to cover the ranges from acoustically thin to acoustically thick. General parameters of either glassy or rubbery films are used in the calculation. No specific polymer film is considered. An interesting result is that the frequency increases when thickness suppresses the film

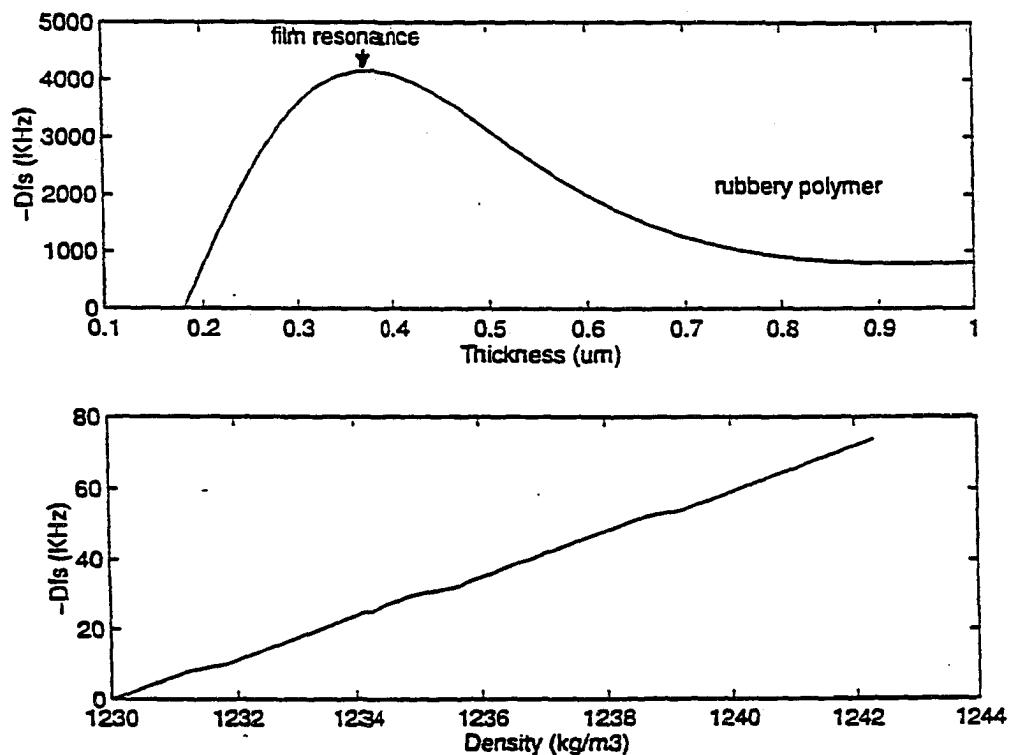


Figure 3.5 Modeled TFR frequency shift vs. polymer mass and thickness changes for a rubbery polymer film

resonance point, which can be experimentally observed as a positive frequency change. The effects by mass density variation are slightly smaller than that in a glassy film. As shown in Figure 3.2, the film resonance shifts to a thin rubbery thickness at low viscosity range. The film resonance effects are also observed in QCM mass sensor applications.<sup>10,30</sup> The 3D results of series resonant resistance and Q shown in Figure 3.6 give a clear illustration. As described before, the resistance increases while Q dramatically decreases in the vicinity of film resonance.

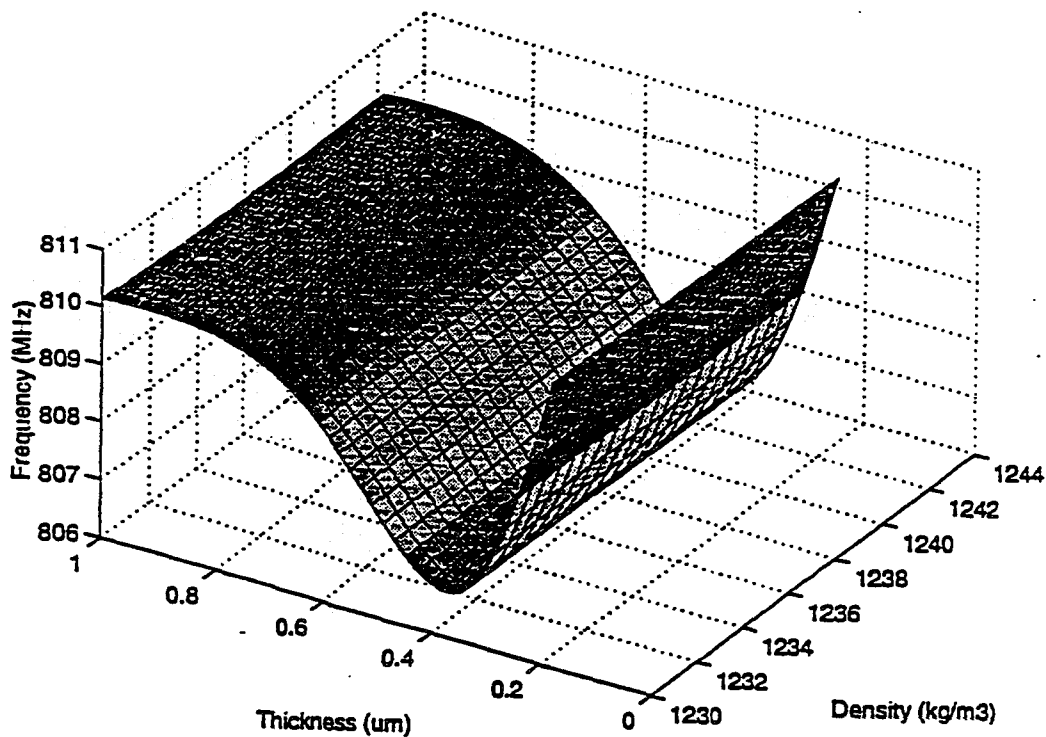


Figure 3.6 a) 3D plot of resonant frequency varied by thickness and mass density of a rubbery polymer film

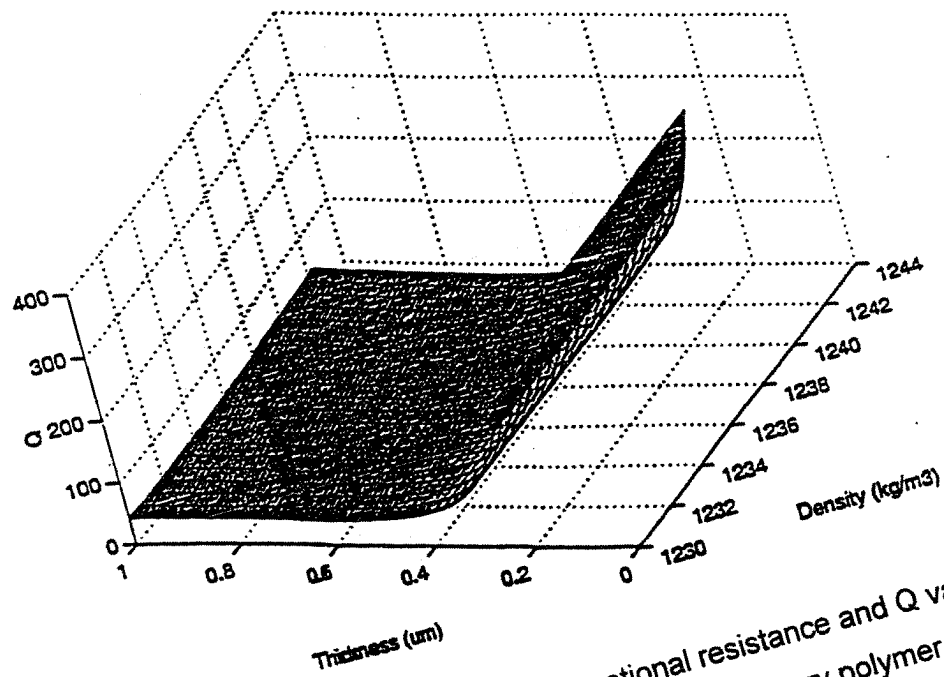
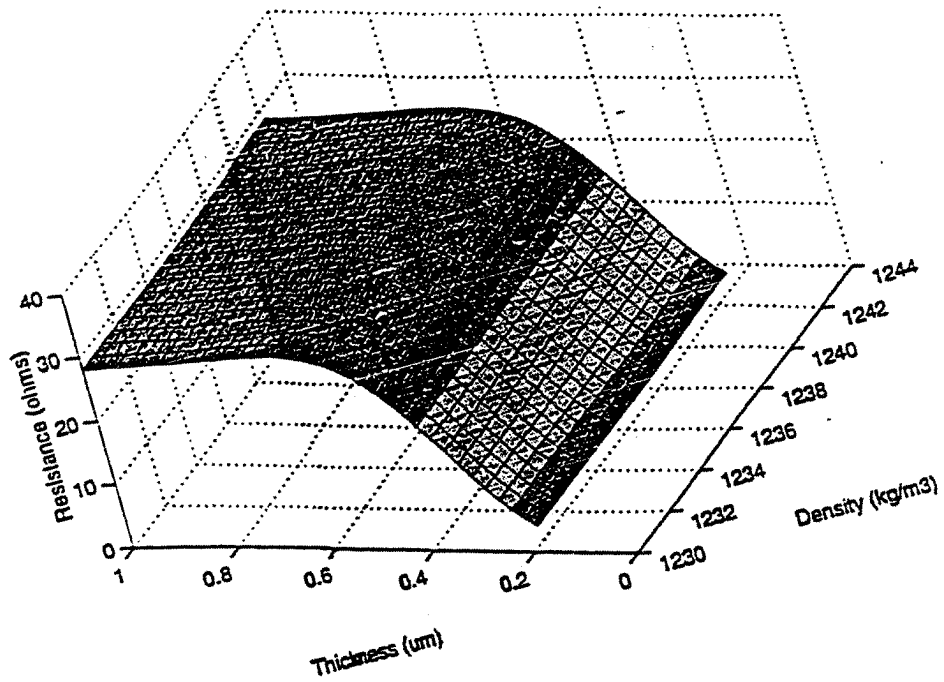


Figure 3.6 (continued) b) 3D plot of motional resistance and Q varied by thickness and mass density of a rubbery polymer film

### Viscoelastic Effects

As described before, the absorbed analyte dilute polymer film and increases the free volume inside the polymer. Free volume is the volume not occupied by polymer molecules that presents microvoids of molecular dimension. This effect, especially when an acoustically thick film is used, enhances polymer chain segmental mobility and can be generalized by a translation parameter,  $\alpha_T$ :<sup>6</sup>

$$\log(\alpha_T) = \frac{B}{2.303} \left( \frac{1}{F(T, V_1)} - \frac{1}{F_0} \right) \quad (3.11)$$

where  $B$  is a constant related to specific polymers. While  $F_0$  is the free volume of pure polymer at a reference temperature.  $F(T, C)$  is the free volume at certain temperature and vapor concentration, and can be expressed as:<sup>6</sup>

$$F(T, V_1) = F(T) + \chi V_1 \quad (3.12)$$

$$V_1 = \frac{\Delta V}{V} = \frac{CV}{1 + CV} \quad (3.13)$$

where  $F(T)$  is the free volume of polymer without analyte dilution. If temperature is constant, then  $F(T) = F_0$ .  $\chi$  is an empirically determined plasticizing parameter, and  $V_1$  is the volume fraction of absorbed analyte.  $C$  is the concentration (mol of sorbed vapor/mL of polymer), and  $V$  is the specific volume of absorbed analyte. At high analyte concentration, the volume fraction of absorbed analyte increases which induces the translation coefficient  $\alpha_T$  to decrease. The changes in the viscoelastic properties with temperature and vapor absorption can be expressed as the translation  $\alpha_T$  in the polymer relaxation time or the probe frequency  $\omega(T, V_1)$ :<sup>6</sup>

$$\log[\omega(T, V_1)] = \log(\omega) + \log(\alpha_T) \quad (3.14)$$

The increased free volume leads to a decrease of the probe frequency and both bulk and shear moduli as shown in Figure 3.7. A polymer relaxation or glassy transition is exhibited by the intrinsic elastic properties: At high probe frequency, the storage components ( $K'$ ,  $G'$ ) are maximum and the polymer is in glassy state. The small changes that occur in  $K'$  in comparison with  $G'$  may result in TFR responses arising largely from the changes in  $G$  rather than changes in  $K$ . This phenomenon may change the dynamic range of acoustically thickness. Loss components,  $K''$  and  $G''$  are dramatically changed in TFR frequency range which may result large viscosity effects. Frequency shift is thus required to include both mass, thickness expansion and viscoelastic effects. Notice that changes due to elastic moduli may not be necessarily due to linear dependence on the amount of absorbed analyte

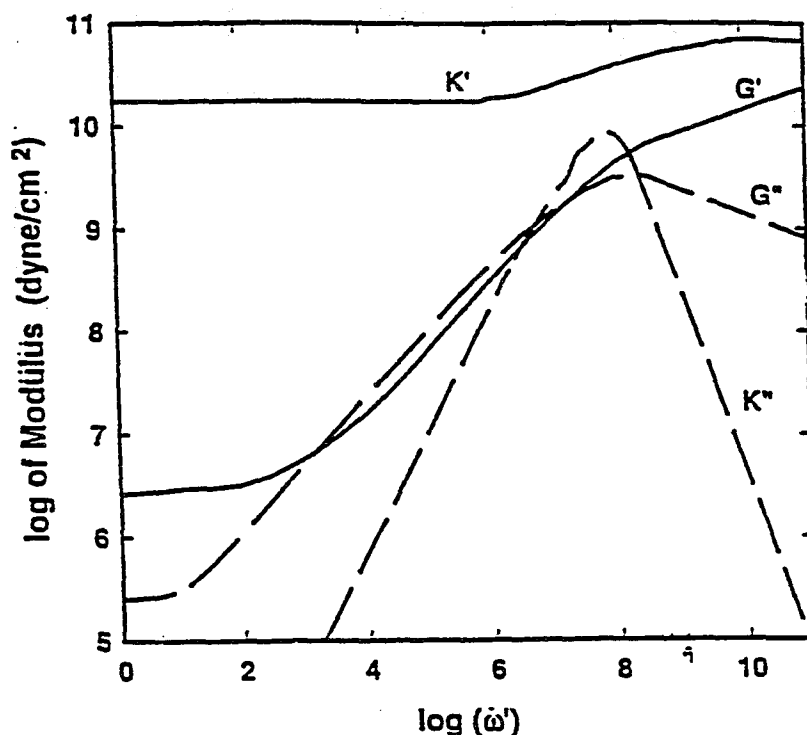


Figure 3.7 Elastic moduli vs. polymer relaxation time<sup>6</sup>

since very complicated molecular thermodynamics and relaxation processes are involved in the analyte absorption-desorption dynamics.

The modeled resonant parameters for a glassy polymer film are shown in Figure 3.8 in which a film resonance occurs in the glassy-rubbery transition range while frequency changes dramatically. Parameters used for this calculation are density of 1230 kg/m<sup>3</sup>, thickness of 0.18  $\mu\text{m}$  for glassy polymers and 0.5  $\mu\text{m}$  for rubbery polymers. As the thickness effects in rubbery polymer film, a positive frequency change may occur. With large viscosity, this film resonant point moves even to low elastic range of rubbery state. The motional resistance, Q, inductance and capacitance vary dramatically in the vicinity of film resonance since device is highly damped. The viscosity variation for a very glassy film has small impact on

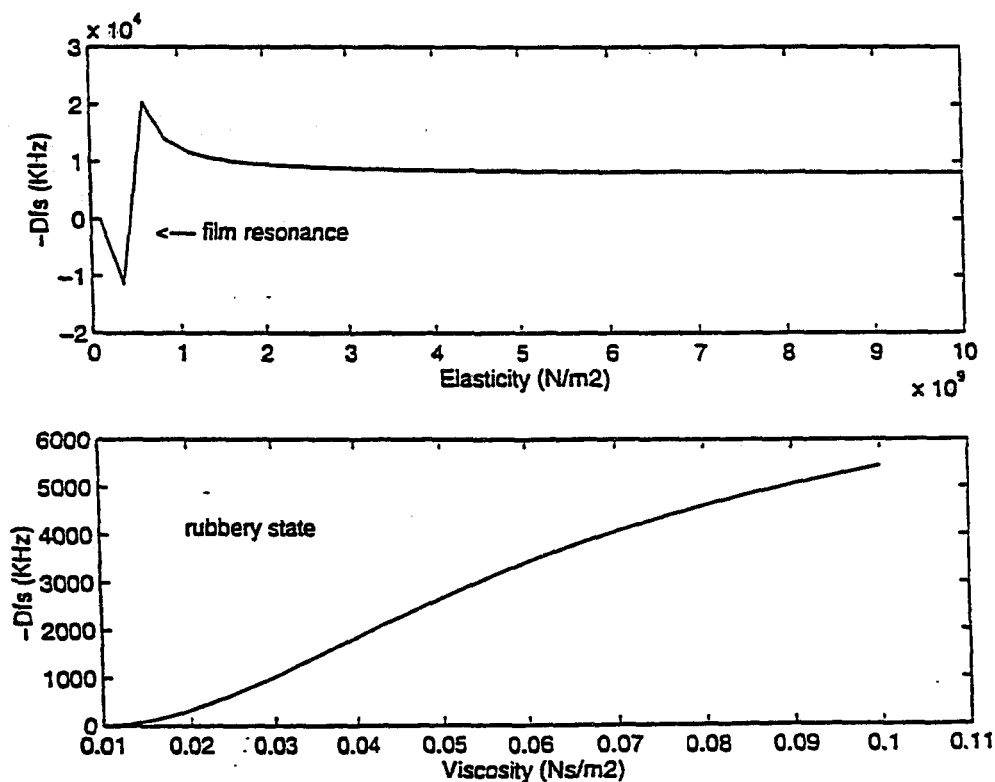


Figure 3.8 Modeled TFR frequency shift vs. polymer viscoelasticity in glassy range

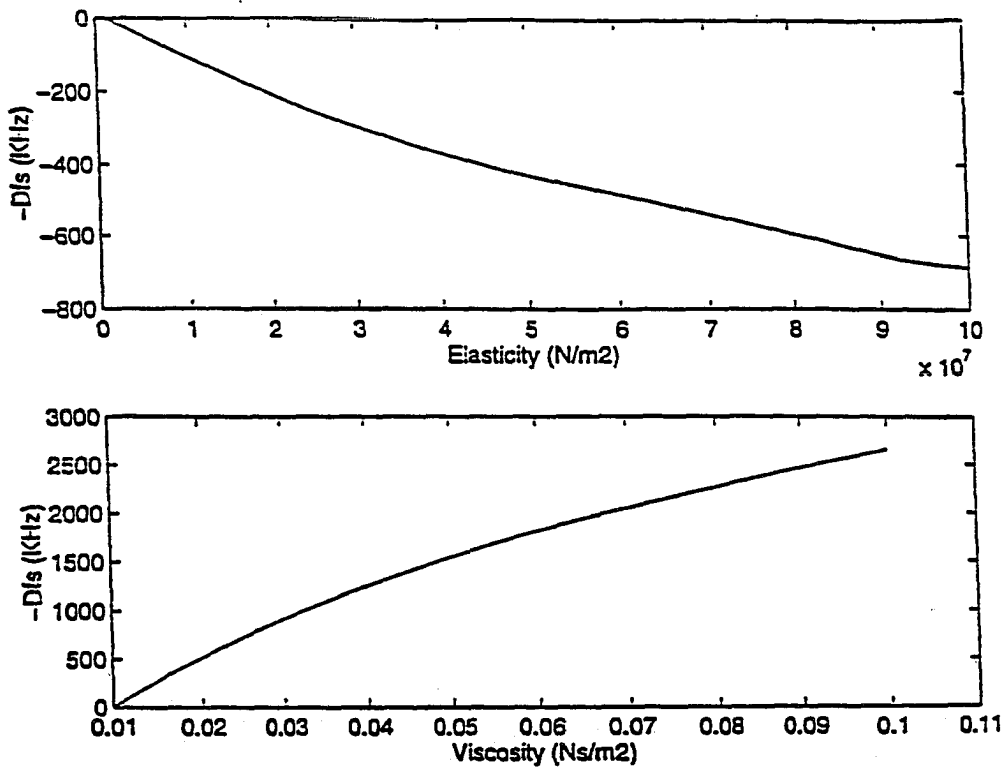


Figure 3.9 Modeled TFR frequency shift vs. polymer viscoelasticity in rubbery range

responses compared to the elasticity. Responses from a rubbery polymer film are shown in Figure 3.9. The frequency decreases with reducing elastic modulus. Compared with glassy film, viscosity shows strong effects on the responses which is expected in the high frequency range. This indicates the rubbery film has more profound dynamic responses, especially for TFR devices.

The 3D plots are shown in Figure 3.10 (glassy film) and in Figure 3.11 (rubbery film) where dynamic responses are varied by viscoelastic properties. Since a polymer usually behaves as a glassy film in TFR high frequency range, storage modulus variation is relatively smaller. Dynamic responses other than mass loading and thickness expansion are most probably due to the changes of loss modulus (mostly viscosity).

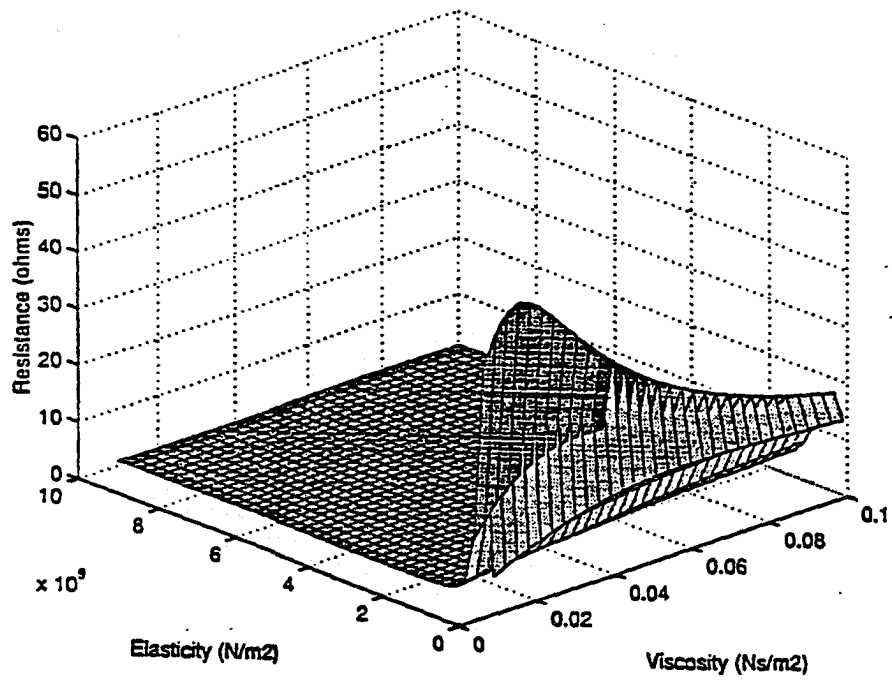
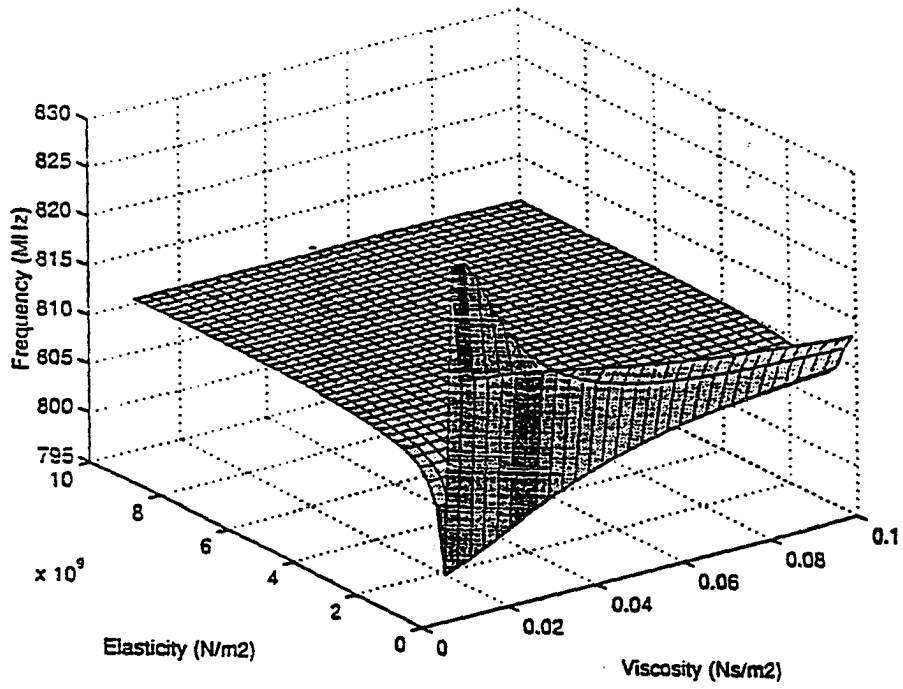


Figure 3.10 3D plots of motional parameters varied by viscoelasticity in glassy range

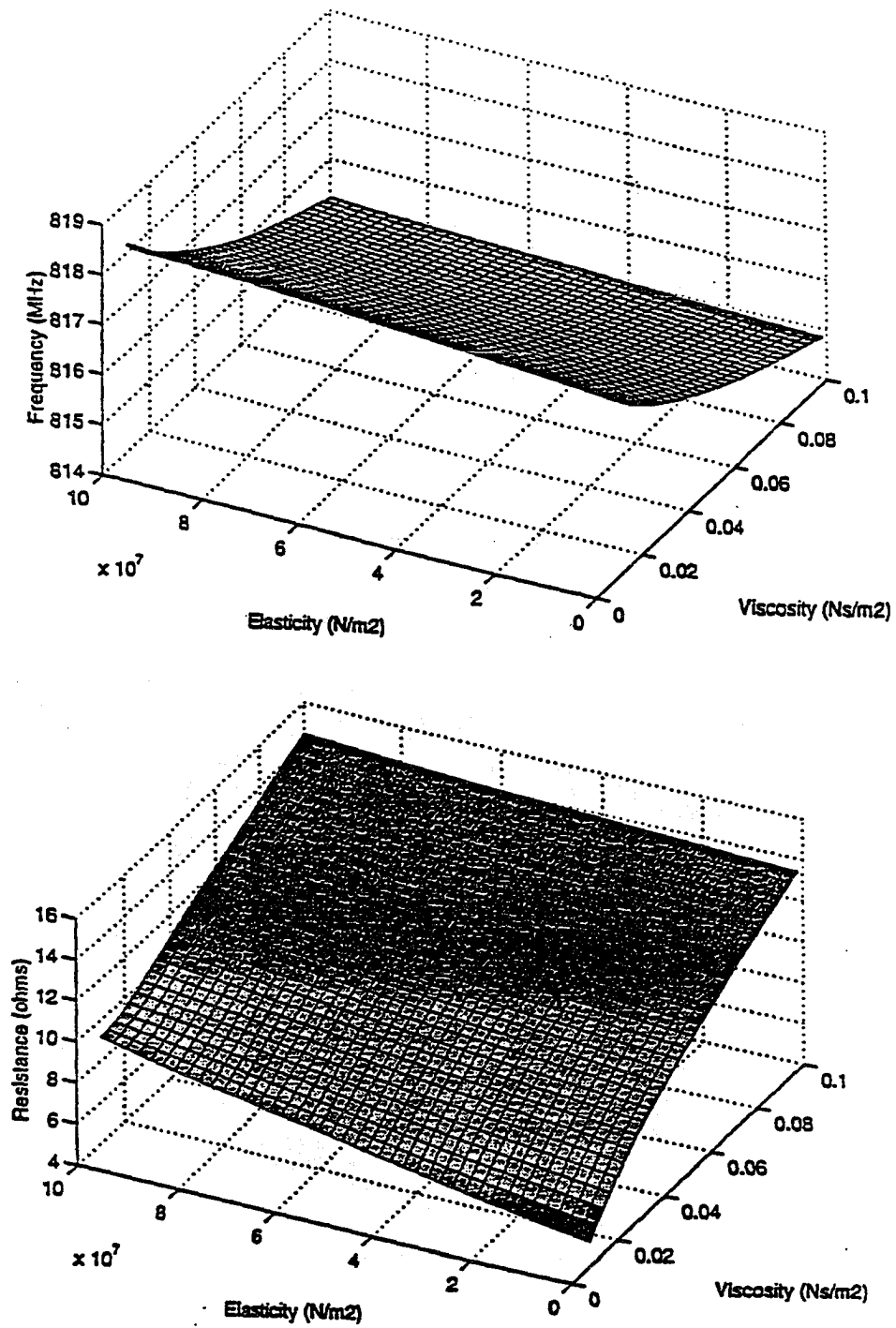
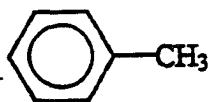
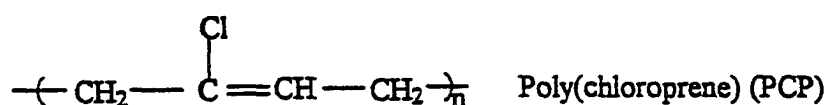


Figure 3.11 3D plots of motional parameters varied by viscoelasticity in rubbery range

## Experiments

TFR polymer sensitivity experiments consist of measuring the responses of PCP (polychloroprene) polymer-coated TFR devices during toluene vapor absorption by the polymer at room temperature. The TFRs used in this study have stacked structure of Cr/Al bottom electrode, sputtered AlN piezo-film, and Cr/Au/PdNi top electrode. TFRs were wired-bonded to a matched TFR test fixture and corrected by the standard one-port calibration. It is found that the contact and transmission-line inside the test fixture contribute about 2 ohms resistance, while bonding-pad and thin metallization contribute at least 2-5 ohms, depending on which metal is used (calculated in Chapter 5). This is the major disadvantage for high-Q TFR application. HP resonator software was used to calculate resonator parameters through an HP 8753 network analyzer. The best curve fit technique is used to extract the motional lumped elements.

A manually and a computer-controlled vapor test system varied the vapor concentration by varying the relative flow rates of the nitrogen carrier stream saturated with the vapor (passage through a bubbler) with a nitrogen mix down stream. The associated vapor concentration can be calculated from the saturation vapor pressure and testing temperature. The PCP unit and toluene vapor are shown in Figure 3.12. PCP coating was prepared by spin casting at different speed to



Toluene

Figure 3.12 PCP and toluene chemical formula

assure coating uniformity and can slightly vary the resulted coating thickness. Film thickness measurements were attempted by profilometry. However, the softness of the films resulted in stylus penetration into the film and erroneously low readings. Therefore, film thickness was obtained by measuring frequency changes of a QCM device before and after film coating. At QCM frequency range, film is in the glassy regime and behaves as perfectly acoustically thin. The Sauerbrey equation was then used to calculate the film thickness. A 18.3 KHz frequency was measured by network analyzer, from which the film thickness is calculated to be 0.18  $\mu\text{m}$ . A typical TFR response with PCP polymer to toluene is shown in Figure 3.13. To determine the concentration of vapor absorbed in the polymer film on the TFR device, again, a 9 MHz QCM device with the same polymer film thickness was used for the calibration. The absorbed mass at different analyte vapor concentration was calculated by frequency change from a 9 MHz QCM. Due to its low frequency, the 9

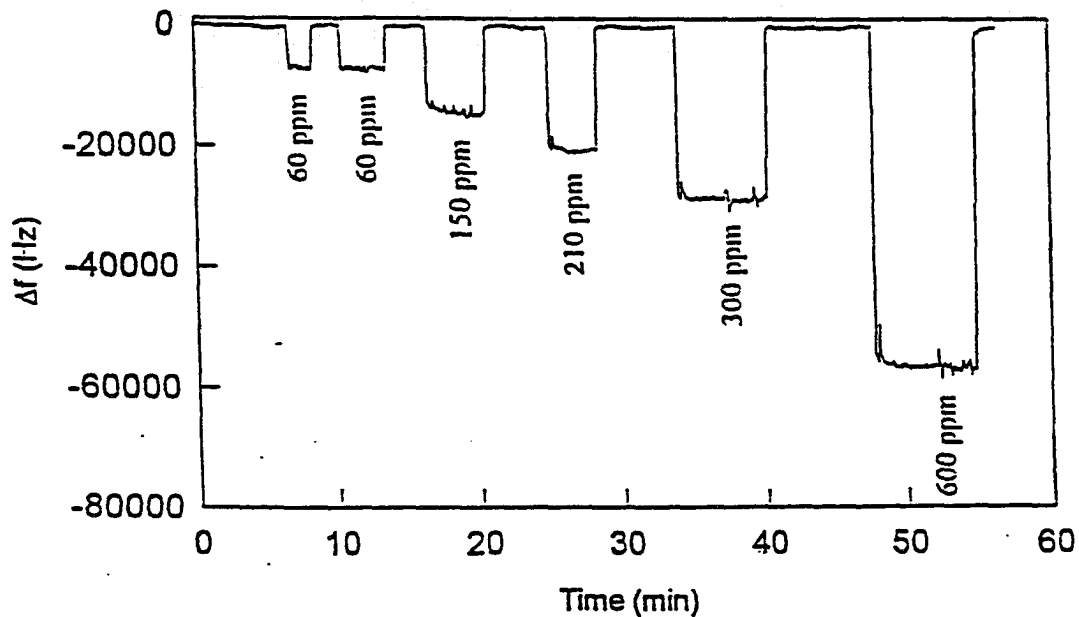


Figure 3.13 Typical TFR Responses with PCP/toluene system

Table 3.2 Analyte parameters

toluene analyte	
mass, $m$ (g/mol)	92
liquid density, $\delta$ (g/cm <sup>3</sup> )	0.86
volume, $V=m/\delta$ , (mL/mol)	105
plasticization parameter, $\chi$	0.083

MHz QCM responds as a nearly ideal gravimetric detector for this range of film thickness. From the absorbed mass, the analyte concentration in polymer film was determined. The model parameters used to calculate the toluene concentration in PCP polymer is shown in Table 3.2.<sup>47</sup> Thickness expansion and mass density changes due to the vapor absorption were determined via the analyte concentration in polymer. Substituting this thickness and mass density in simulation, frequency shift can then be calculated. Figure 3.14 shows the comparison of responses between the measurement and the modeled where one modeled result is due to pure mass and another is due to both mass loading and thickness expansion. At relatively low vapor concentration ( $\leq 100$  ppm), the modeled and measured results are very close. Above medium high concentration ( $\geq 600$  ppm), the difference becomes large. The modeled result combining both mass and thickness effects is more close to the measurement. This may indicate that, at low concentration, mass loading dominates the responses. The absorbed analyte mostly occupies the vacancies inside the PCP polymer. At high concentration, thickness expansion has to be considered since all the vacancies have already been resident by analyte. Although a PCP film may behave as a glassy film in the TFR frequency regime at room temperature, its physically rubbery structure may be more prone to promote thickness expansion. This may suggest that the film expansion (plasticizing) effect more easily occurs in polymer films with the absorbed analyte of light molecular weight and large specific molecular volume, while mass loading effect dominates in analyte absorption with large weight and small specific

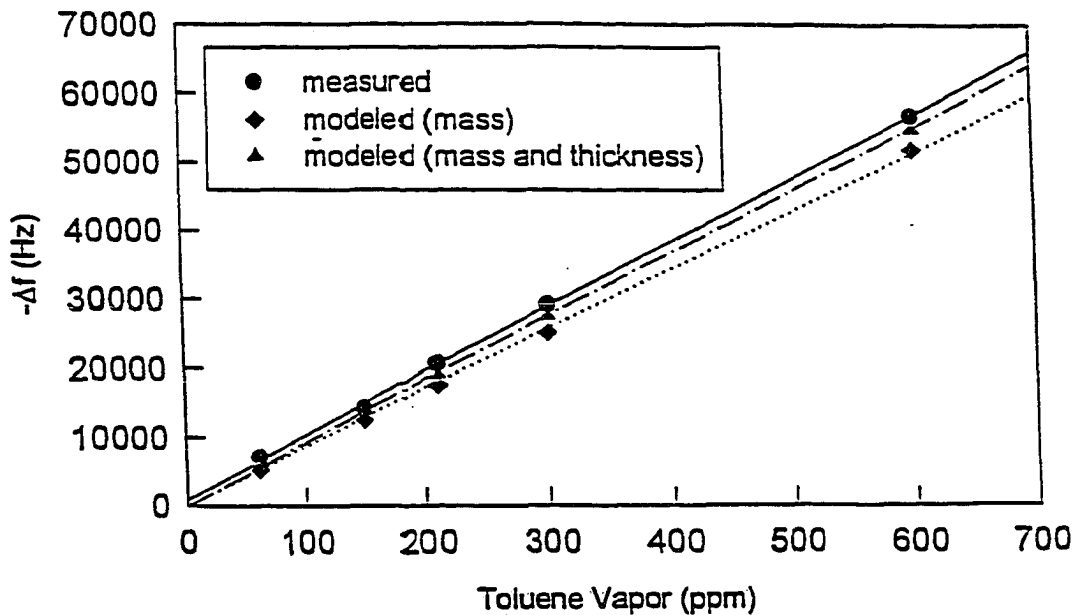


Figure 3.14 Modeled and measured the PCP responses to toluene vapor

molecular volume. Also notice that about 4-5 % of the responses at this mediate high concentration ( $\geq 600$  ppm), are due to other unknown effects such as experimental error, film moduli changes, or substrate TFR and film electrical and dielectric changes.

The free volume contributed by toluene analyte can be calculated from equation (3.11, 3.12) by substituting in the calculated analyte concentration. The fraction volume of absorbed analyte at 600 ppm vapor concentration is fairly small ( $8.8 \times 10^{-5}$ ). The probed frequency change ( $\log(\omega)$ ) is thus calculated to be about 0.001, which is small to change the elastic moduli as indicated by the master curve in Figure 3.7. On the other hand, volume expansion by high vapor concentration not only leads to increased free volume but also increased in-plane compressive stress, which may in turn diminish free volume increments. The moduli variation in an acoustically thin glassy film coated on longitude TFR devices may play a minor part

in characterization dynamic responses, especially in low vapor concentration ranges. The difference between modeled and measured results shown in Figure 3.14 is thus believed to be caused mostly by experimental error and other electrical and dielectric changes which are difficult to predict with present models.

Results of PCP-coated longitude and shear TFR exposed to Toluene vapor are shown in Figure 3.15 in which a thin PCP polymer film ( $0.18 \mu\text{m}$ ) was used. The fractional frequency changes ( $\Delta f_s/f_s$ ) of longitude-TFR and shear-TFR were not quite different. Although shear modulus is smaller than bulk modulus, the film is still acoustically thin and remains in the glassy regime since resonance frequency for shear mode is around 500 MHz. The fractional frequency change is proportional to

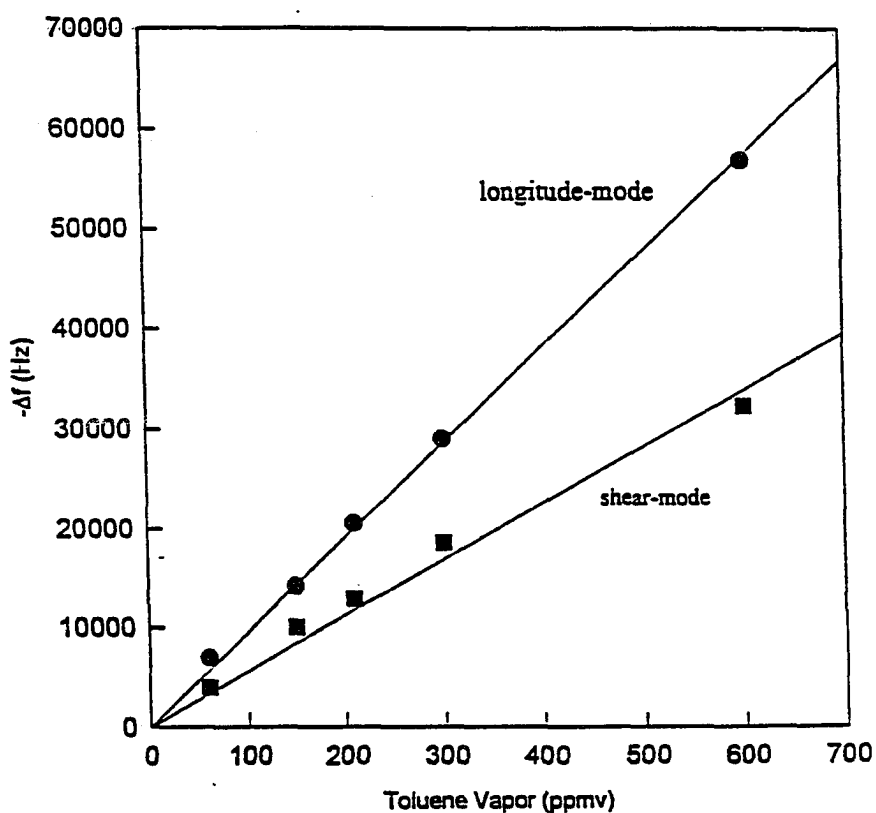


Figure 3.15 Responses from longitude-mode and shear-mode TFR

the absorbed mass, expanded thickness and unloaded frequency, and inversely proportional to the corresponding wave velocity. If the same amount of mass and thickness expansion occur in the film and the moduli variation is small, then fractional frequency change is totally controlled by the thickness of the TFR composite and aluminum nitride film density. Therefore, similar fractional frequency responses of longitude and shear TFR should be expected. This indicates that, with an acoustically thin polymer film, both longitude-mode and shear-mode TFRs can be effectively used as microsensors. Notice that this conclusion is only based on the frequency changes. The shear-mode TFR devices experience more viscosity damping which increases resonant resistance and deteriorates  $Q$ , and in turn worsens the frequency stability. This effect can also be viewed from the master curve in which the loss component of modulus for shear strain is higher than that of the compressive strain.

In contrast to QCM or SAW devices, in-plane compression strain dominates wave motion in a longitude-mode TFRs. Cross-plane displacement, which is large in SAW polymer sensors, is fairly small in TFR-longitude polymer sensors. The frequency used in longitude TFRs is usually five to six times higher than that used in SAW devices. Polymers used in TFRs are thus more prone to behave as acoustically thin compared to SAW devices, which means the polymer is more rigid and behaves as glassy film. The dependence of elastic modules on polymer relaxation variation induced by absorbed analyte is fairly small for the longitude component. Consequently, mass loading and film expansion effects may predominate the responses compared to SAW polymer sensors. If noise performance of TFRs can be enhanced, TFR polymer sensors should have very promising applications.

#### Sensitivity and Detection Limit

As discussed in the front sections, sensor responses are due to the changes of mass loading, thickness expansion and elastic modulus. Although mass loading is

not the only mechanism of sensor responses, it is a common acceptable benchmark to characterize and compare different acoustic sensors. This is also because most acoustic devices are developed to detect the trace-level analyte under a well-controlled environment. Other effects due to the changes of dielectric, piezoelectric and electrode resistivity are controlled to a minimum level. The film elastic properties and plasticizing effects are reduced by using acoustically thin coating. The sensitivity is defined as <sup>7</sup>

$$S_m = \frac{\Delta f_s / f_s}{\Delta m / A} \quad (3.15)$$

$S_m$  thus expresses the sensitivity of the fractional frequency change ( $\Delta f_s / f_s$ ) per incremental change in mass loading. For most acoustic devices, the sensitivity increases by increasing frequency (except for FPW devices) and decreasing the effective mass per unit area. This can be done by decreasing membrane thickness (QCMs, TFRs, FPWs) or decreasing wavelength (SAWs, STWs). Table 3.3 lists the sensitivity examples of commonly used acoustic devices. <sup>7</sup> The sensitivity of TFRs is calculated from the experimental data by PCP(0.18  $\mu\text{m}$ )/ toluene system. From the sensitivity examples of commonly used acoustic devices. <sup>7</sup> The sensitivity of TFRs is calculated from the experimental data by PCP(0.18  $\mu\text{m}$ )/ toluene system. From the

Table 3.3 Mass sensitivity of five type acoustic wave devices

	$S_m$ , sensitivity (Hz/MHz)/(ng/cm <sup>2</sup> )
TSM (6 MHz/QCM)	0.014
SAW (158 MHz/quartz plate)	0.2
FPW (5.5 MHz/composite plate)	0.38
TLM (810 MHz/TFR composite)	0.45

above table, one can find that the TFR is attractive for sensor application because of its high sensitivity.

Mass detection limits depend on the sensor noise level and drift in addition to the sensor's sensitivity. The observed noise is determined by frequency instability of the resonator and analyte coating. Short-term instability of resonant frequency is mainly due to Johnson thermal noise and  $(1/f)$  phase noise.<sup>54,55</sup> Phase noise is caused by phonon scattering fluctuation in the resonator. The more defects and the more imperfect crystal structure the resonator has, the worse the fluctuation of phonon scattering is. The applied frequency and RF power level, and temperature drift may also induce additional fluctuations. High Q resonators are thus required to reduce the phase noise and to improve frequency stability. In case of bulk film resonators, the primary phase noise contributor is believed to be the sputtered piezoelectric film. Low-temperature sputtered piezoelectric films have more intrinsic defects and stresses compared to high-temperature epitaxial films. The tested TFRs fabricated at the MRC have Qs ranging from 100 to 1000 for fundamental longitudinal-mode and from 200 to 2500 for fundamental shear-mode, depending on the different metallizations. In addition to device phase noise, the associated electronics, such as the commonly used oscillator circuits, also contribute noise. This will become even worse in very high frequency application. Slow drift in signal, besides the phase noise, is usually observed in the lab experimental environment. Sometimes the drift behaves as a low-frequency component superpositioned in the fundamental frequency. The drift issue is not only related to the device performance, but also directly to the test environment, setup engineering, humidity, and interaction between analyte and coating. In order to analyze the mass detection limit, a DFT spectrum analysis on the 810 MHz/TFR was first conducted to investigate other possible intrinsic low frequency components. Figure 3.16 shows the DFT spectrum of three modes. The resonant frequency and Q value measured with RF probe are 458 MHz, 1273 (fundamental shear-mode), 810 MHz, 433 (fundamental longitudinal-mode), and 1491, 360 (third shear). The DFT spectrum does not show other

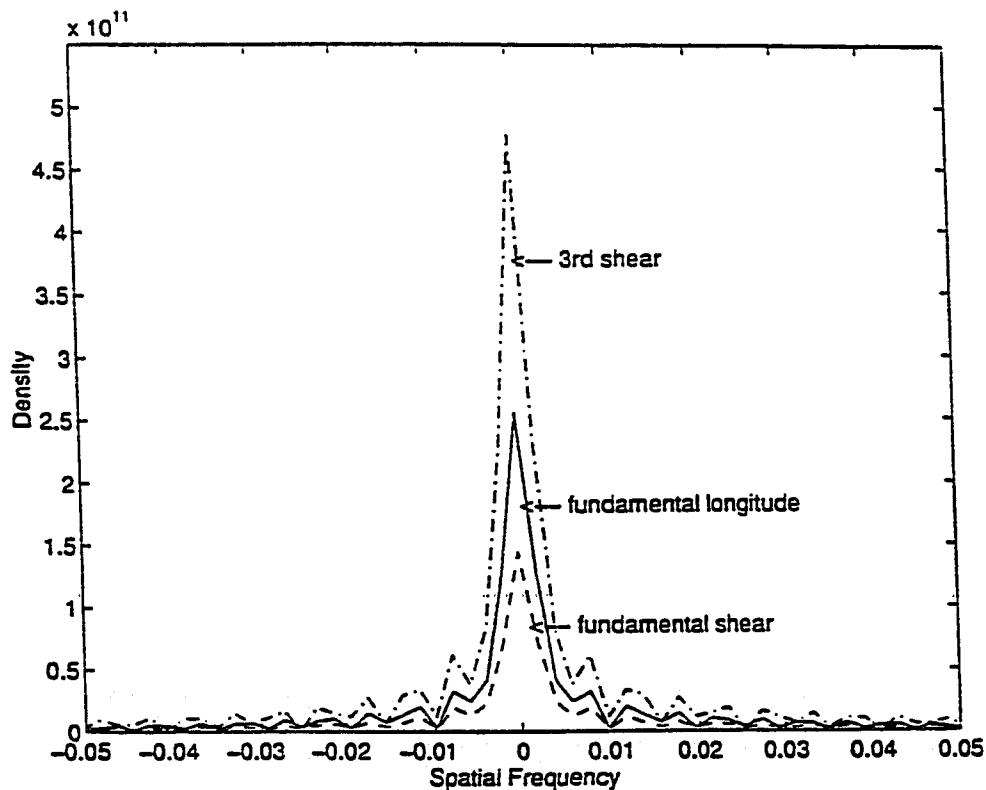


Figure 3.16 DFT spectrum of a typical TFR frequency measurement

frequency components since only the mean value of frequency is observed (zero 'spatial' frequency).

The detection limit is often defined as the analyte concentration that produces a signal three times larger than the noise.<sup>7</sup> The minimum detectable mass per unit area can be derived from Sauerbrey equation as

$$\Delta m_{\min} = -\frac{3\Delta f_{RMS}}{2f_s^2}(v\rho) \quad (3.16)$$

where  $f_s$ ,  $v$ ,  $\rho$  are the resonant frequency, velocity and mass density of an

unloaded TFR.  $\Delta f_{RMS}$  is the measured standard deviation of the loaded TFR frequency change. Substituting this minimum mass to equation (3.10), one can calculate the detection limit in terms of analyte concentration in polymer. The measured noise level of the 810 MHz TFR with PCP/toluene system and the detection limit (DL) are calculated and summarized in Table 3.4

Table 3.4 Detection limit of TFR PCP/toluene system

	810 MHz TFR PCP/toluene
measured noise level (peak-to-peak)	450 Hz
(RMS)	147 Hz
detection limit (fractional frequency)	0.54 ppm
(analyte mass)	$1.2 \times 10$ (ng/ $\mu\text{m}^2$ )
(analyte concentration)	$7.2 \times 10$ (mol/mL)

#### Liquid-coated TFR Analysis and Characterization

Early studies of acoustic wave microsensors are focused on gas- or vapor-phase applications. Recent studies have shown that TSM devices, especially QCM sensors, can be also employed in liquid-phase detection.<sup>56,57</sup> However, liquid-phase operation is precluded if wave motion produces surface-normal displacements. The direction of the longitude wave radiation from successive wave fronts is coherent, causing energy to efficiently leak away from the wave and resulting in heavy attenuation.<sup>7</sup> As the surface of shear-mode devices is placed in contact with a liquid, the wave velocity decreases as if the surface were mass-loaded by a thin layer of liquid. Figure 3.17 illustrates the in-plane motion of a TFR shear-mode device in contact with a liquid. As the work done on QCMs coated with liquid,<sup>57</sup> an extended BVD equivalent circuit can also be extended to analyze liquid-TFR resonant properties as shown in Figure 3.18. When used in liquid, the RF electrode is usually passivated, and only the ground electrode is allowed to contact the liquid in order to prevent interface electrochemical reaction. It is also important that the

TFR surface feature be small compared to wave decay length, and this is very difficult to obtain in TFR devices. Otherwise, considerable longitude displacement may be generated in the rough interface and may increase energy dissipation. In terms of device processing, either a very glassy PECVD layer such as  $SiO_2$ , or  $Si_3N_4$  before top metallization, or a special chemical mechanic polarization (CMP) process may be required in order to achieve excellent performance. Figure 3.19 shows the modeled and measured TFR-water responses. Full-wave analysis was

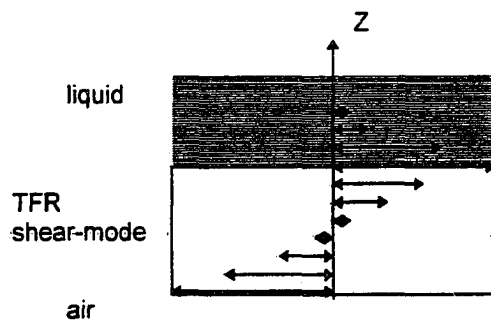


Figure 3.17 Motion of a TFR device contacting with liquid

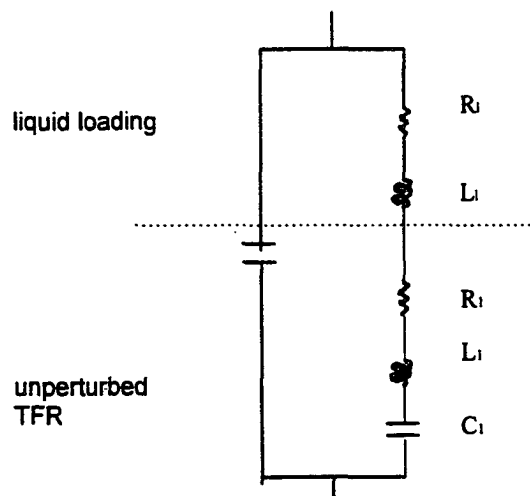


Figure 3.18 BVD model for liquid-loaded bulk shear resonators<sup>57</sup>

used. The viscosity of pure water is  $0.01 \text{ Ns} / \text{m}^2$ . The comparison of frequency shift and admittance magnitude damping is listed in Table 3.5.

There are several reasons for the difference in results, especially for the admittance damping. First, the surface electrochemical effects were observed to be strong. The bonding-wire and ground metallization varied the responses while TFR was immersed in water. When the RF and ground electrode are interchangeably wired-bonded, the admittance is surprisingly increased. Surface potential may be produced because of the Au-water electrochemical reaction. Second, the TFR surface is not hydrodynamically smooth (compared to the skin depth) which may process may be required in order to achieve excellent performance. Figure 3.19 shows the modeled and measured TFR-water responses. Full-wave analysis was

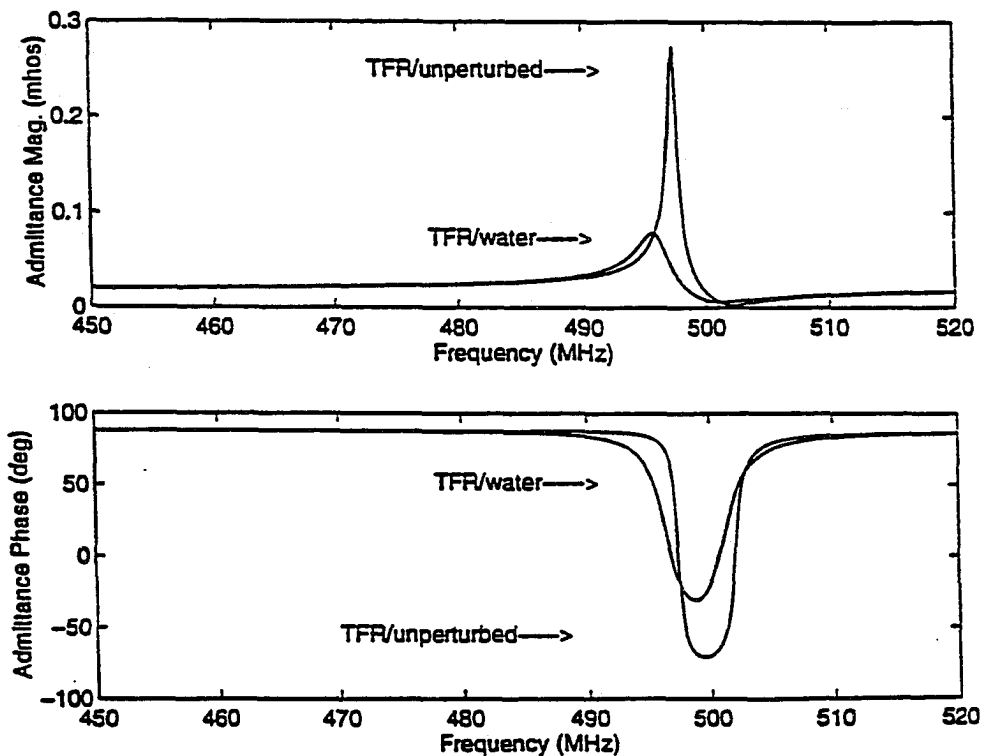


Figure 3.19 a) Modeled responses vs. the liquid loading (DI water)

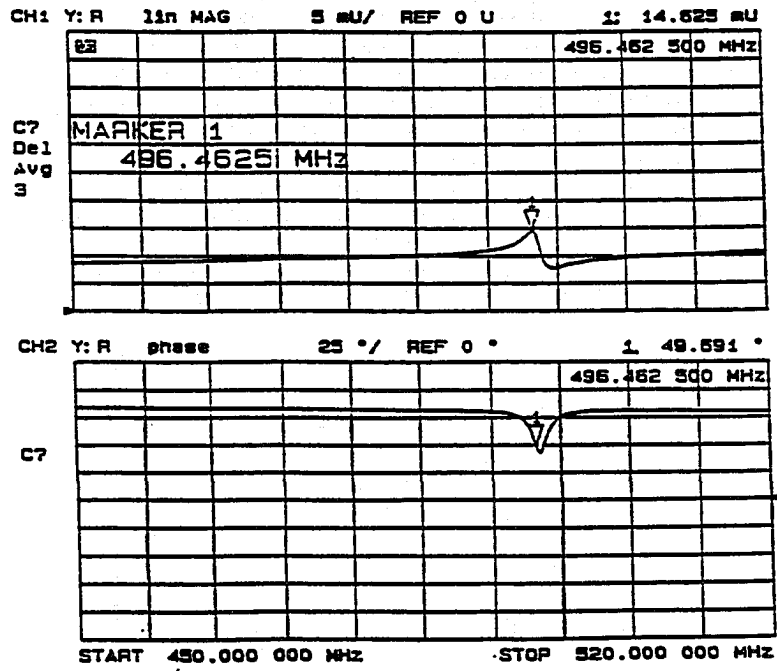
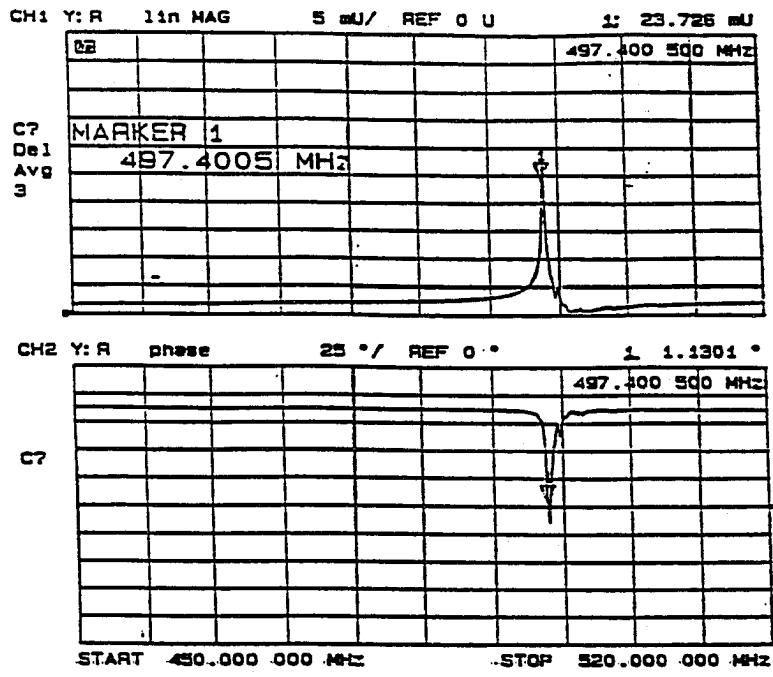


Figure 3.19 (continued) b) Measured responses vs. the liquid loading (DI water)

Table 3.5 Comparison between measured and modeled TFR/water results

	Measured	Modeled
frequency shift (KHz)	938	888
ratio of admittance mag. damping	0.6	0.4

roughness. This phenomenon was observed in other QCM liquid applications.<sup>58</sup> Third, an ideal shear TFR device with Au/AlN/Au configuration was assumed in the wave analysis and only motional path is considered which, as in the polymer modeling, may not accurately interpret the present TFR-water testing setup. The responses by using longitude-mode are shown in Figure 3.20, in which the magnitude is heavily damped because a higher frequency is used and coherent wave coupling occurs in the TFR-water surface.

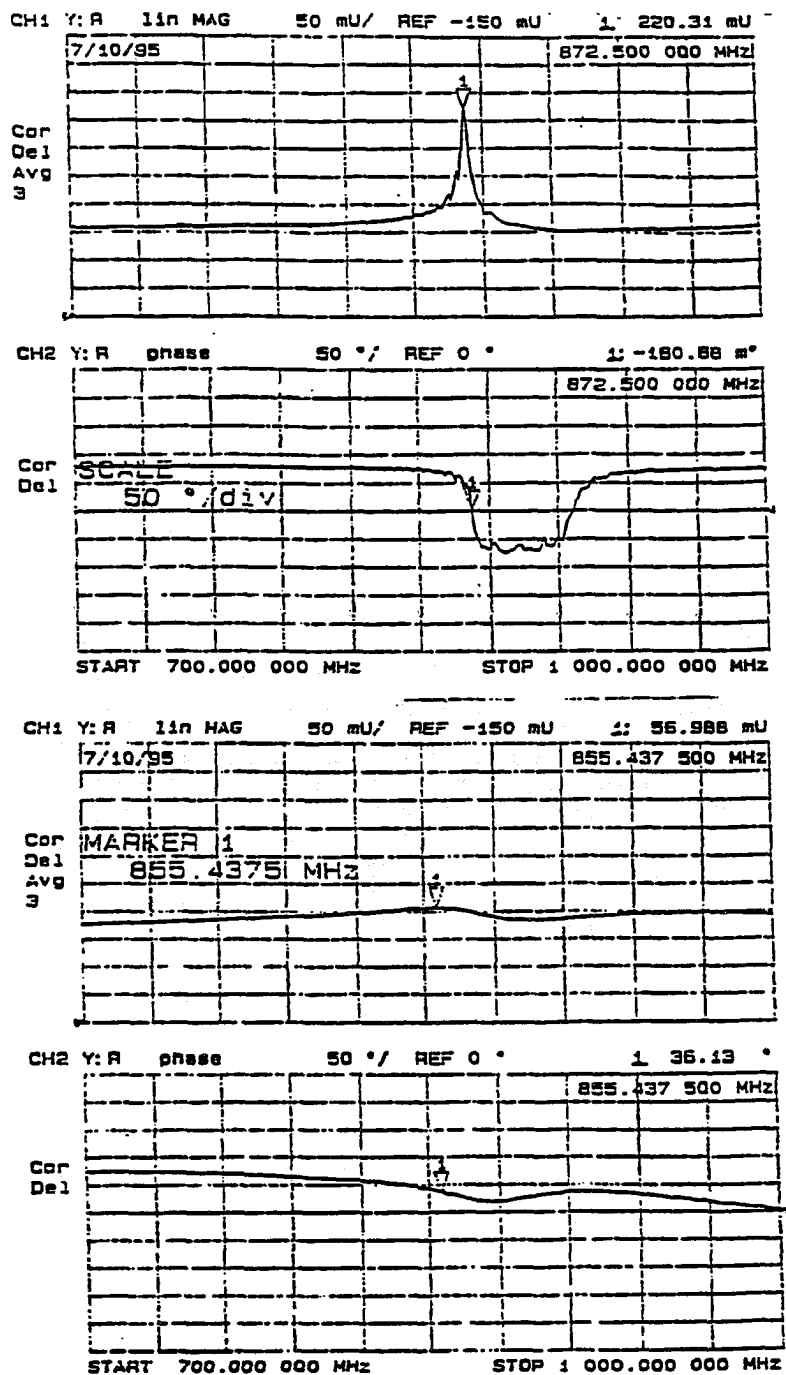


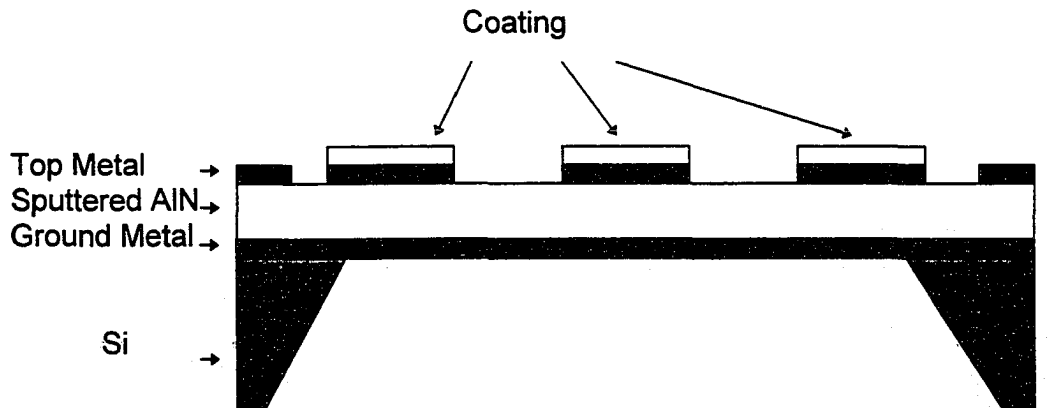
Figure 3.20 Measured longitude-mode TFR-water responses

## CHAPTER 4. TFR ARRAY DESIGN AND MODELING

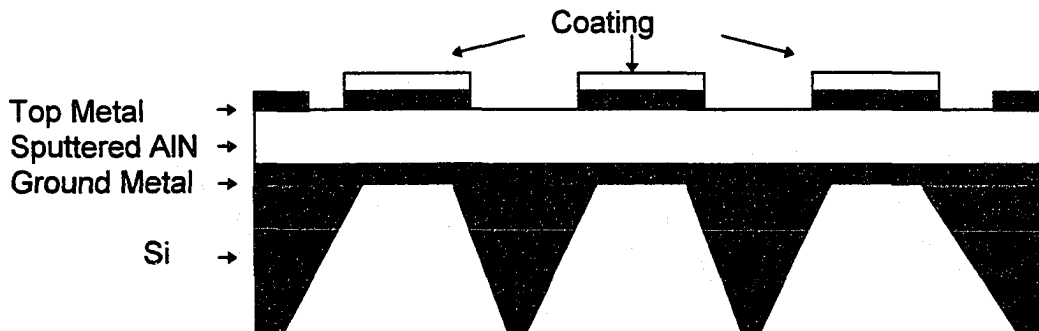
### TFR Array Design

As introduced in Chapter 1, the TFR array should be constructed in order to compensate response drifting due to temperature variation, and material and geometrical mismatch. The differential responses from an analyte and a reference TFR can principally compensate for these effects. However electromagnetic and acoustic crosstalks exist in array structures if individual TFRs are not well designed and patterned sufficiently apart. Acoustic crosstalks contain very complicated wave phenomena. Plate, surface-leaky, and bulk waves are all possibly present in a thin AlN membrane. The ideal approach to diminish acoustical crosstalk is to define TFRs individually. However this requires effectively patterning the AlN film, which is difficult since a thick film is usually used. Besides, large device area and low process yield may occur. Although plasma etching of AlN is being intensively studied thanks to III-V compound device development, there are few successful reports of effectively patterning thick AlN piezoelectric films. Extra photo and plasma processes are thus required to implement these monolithic arrays. Care must also be taken to prevent the loss of piezoelectric properties of the film. While pursuing ultimate patterning methods by higher technology, one should remember that the purpose of building TFR sensor arrays is to compensate temperature and other material mismatch, and eventually realize a full automatic microanalytical system. Other hybrid array structures such as the one described below may also realize the implementation of microsensors systems. To demonstrate this array concept, two designs by defining multiple TFRs on the same AlN membrane are presented. Hybrid integration of this TFR array with active devices may then be used to develop a customized microsensors system. These two basic array structures on same AlN membrane were proposed as shown in Figure 4.1, with 1) TFR on the same Si substrate window (SW) and 2) TFR on different Si substrate window (DW), but closely spaced. The advantages of these structures, especially the SW array, are

that no AlN definition is needed and piezoelectric properties remain undisturbed. A multi-TFR array can be compacted in a single dice on the same AlN membrane. Temperature and material-induced drifting can then be effectively compensated. The ultimate approach is to build a monolithic TFR array as shown in Figure 4.2. Individual TFRs are defined on different AlN membranes. The advantages of

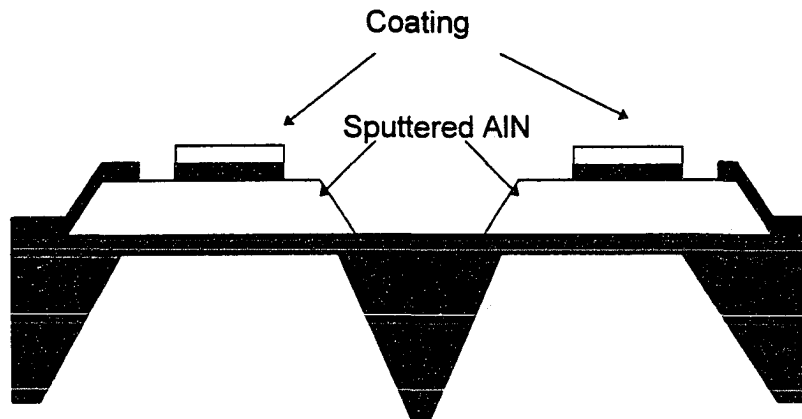


1) TFR array on same back-side Si window (SW array)

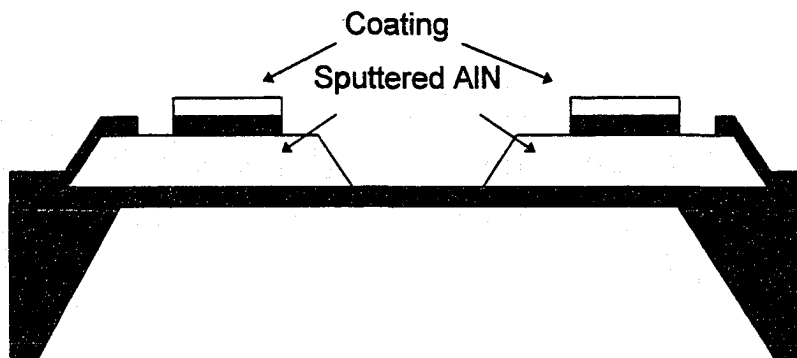


2) TFR array on different back-side Si window (DW array)

Figure 4.1 TFR array on same AlN membrane



1) TFR array on different back-side window



2) TFR on Same back-side window

Figure 4.2 TFR Arrays with different AlN membrane

this monolithic approach are that energy is effectively trapped in the device area and no wire-bonding is needed (parasitic effects between the bottom electrode and ground bonding is thus terminated). Its disadvantages are the larger device area used and the possible loss of piezoelectricity of the AlN film since extra photo and etch processes are required.

In this work, TFR arrays on the same AlN membrane are designed and implemented. The design challenge is how to diminish or decouple the lateral wave coupling between TFRs without using a larger dice area. Although quasi-Rayleigh, leaky and pure shear waves may all propagate in the AlN plate, major acoustic crosstalks arise from plate lamb waves, especially flexural waves, since membrane thickness approaches the wavelength and an asymmetric electric field is applied across the AlN plate.

### Array Acoustic Modeling

The acoustic wave crosstalk between TFRs derives from the wave propagation laterally through the AlN film and on the AlN surface. Notice that the lateral waves are shear modes since a two-port TFR array configuration is used. The shear mode is defined in that particle displacement direction perpendicular to the wave propagation, while the longitude mode is defined as the displacement and wave propagation in the same direction. As discussed in Chapter 2, weakly piezoelectric coupling and quasistatic approximation are applicable for low piezoelectric materials. Electrical flux density is then related to the gradients of particle displacement as long as the stiffened elastic constant is used. Notice that this approximation is only valid in the anisotropic materials with low piezoelectricity (like AlN or QCM), and plane wave propagation. The electrical potential can then be derived as<sup>21</sup>

$$\phi = \frac{1}{(-j\omega)} \frac{(l_i e_{iL} l_{Lj})}{l_i \epsilon_{ij}^E l_j} v_j \quad (4.1)$$

$$l_{Lj} = \begin{bmatrix} l_x & 0 & 0 & l_z & l_y \\ 0 & l_y & 0 & 0 & l_x \\ 0 & 0 & l_z & l_x & 0 \end{bmatrix}^T \quad (4.2)$$

where unit vector  $\hat{\mathbf{l}} = \hat{x}l_x + \hat{y}l_y + \hat{z}l_z$  is the wave propagation direction.  $e$  and  $\varepsilon$  are piezoelectric and dielectric constants.  $\mathbf{v}$  is particle velocity vector.  $I_{ij}$  identifies the unit matrix. From equation (4.1), one can find that electrical potential is uniquely related to the particle velocity field, and the piezoelectric and dielectric constants. In other words, electrical energy is dependent on the mechanical energy and piezoelectric transformation. As discussed in the introduction section, a three-dimensional boundary method has to be implemented if a complete solution of displacement and electric field is required, and is beyond the scope of this research. Also huge computer power is required for three-dimensional numerical methods since larger transverse geometry (relatively to wavelength) is encountered. Any approximation, even in two-dimensional cases, may not be correctly interpreted to real device operation since some elastic information is lost. Under low power, linear condition and ideal piezoelectric transformation, an assumption is thus made in which electrical energy loss can be approximately represented by the energy attenuation of particle velocity. The mechanical attenuation can then be calculated as a measure of electrical energy loss and approximately expressed by the measurable electrical insertion loss. Energy transmission in a two-port configuration is schematically shown in Figure 4.3. In fact, electrical energy loss is larger than mechanical energy loss since a non-ideal piezoelectric transformation is always expected due to AIN dielectric loss and loss component of piezoelectricity. This means that the separation distance to acoustically isolate two adjunct TFRs can be approximately calculated by the mechanical energy attenuation as long as the piezoelectricity is incorporated in the stiffened anisotropic elastic constants. To illustrate different wave mode characteristics, stiffened shear wave is first investigated in an anisotropic hexagonal plate waveguide. A axisymmetric two-dimensional transient finite element method is then implemented to consider complicated flexural plate wave propagation.

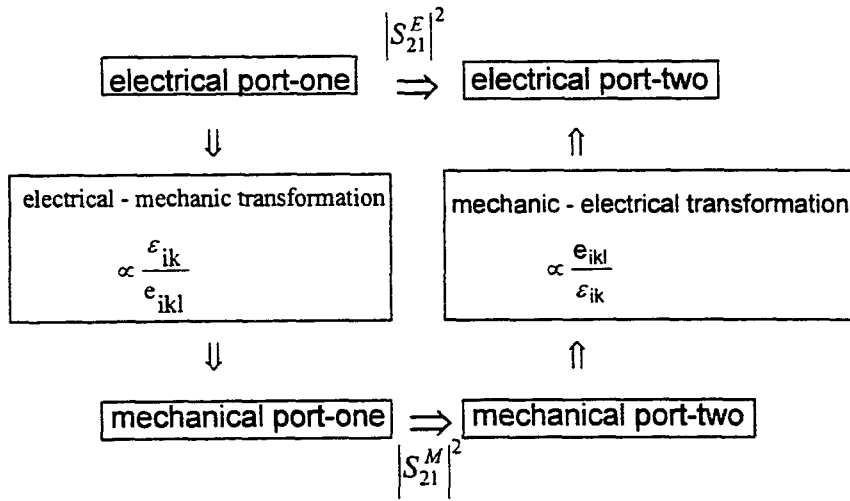


Figure 4.3 Mechanical and electrical energy transmission

#### Analytical Solution For Stiffened Pure Shear Wave

The region between adjunct TFRs can be treated as a two-dimensional parallel-plate acoustic waveguide as shown in Figure 4.4. The stiffened wave is a pure shear wave. Following the same analysis as in Chapter 2, the dispersion relation and velocity field for this stiffened shear wave can be readily written as

$$\kappa_x^2 = \left(\frac{\omega}{V_s}\right)^2 - \kappa_z^2 \quad (4.3)$$

$$v_z = (Ae^{-j\kappa_x z} + Be^{j\kappa_x z})e^{-j\kappa_z x} \quad (4.4)$$

The traction-free boundary requires

$$T_{zz} = \bar{c}_{33}S_{33} = 0 \quad \text{at } z = \pm \frac{h}{2} \quad (4.5)$$

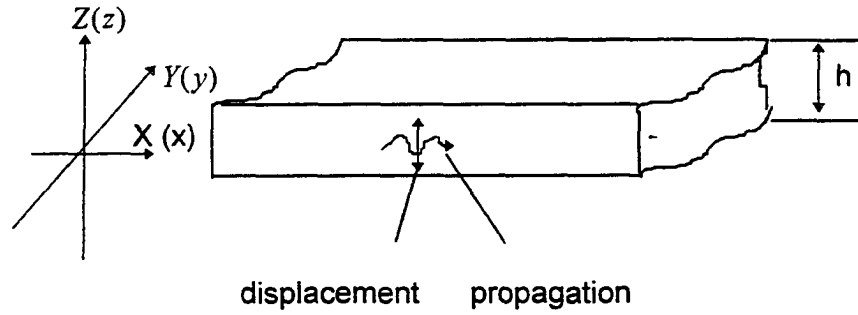


Figure 4.4 AlN free anisotropic plate

The traction-free boundary requires

$$T_z = \bar{c}_{33} S_{33} = 0 \quad \text{at } z = \pm \frac{h}{2} \quad (4.5)$$

which requires that

$$\bar{c}_{33} \frac{\partial u_z}{\partial z} = j\bar{c}_{33}\kappa_z (-Ae^{-j\frac{\kappa_z h}{2}} + Be^{j\frac{\kappa_z h}{2}}) e^{-j\kappa_z x} = 0$$

at any lateral position ( $x$ ). This condition is satisfied if

$$A = -B$$

$$\kappa_z = \frac{n\pi}{h}, \quad n = 1, 3, \dots \text{ mode number}$$

From the (4.3), the dispersion relation is

$$\kappa_s^2 = \left(\frac{\omega}{V_s}\right)^2 - \left(\frac{\pi}{h}\right)^2 \quad (4.6)$$

The shear velocity is

$$V_s = \sqrt{\frac{\bar{c}_{44}}{\rho}} \quad (4.7)$$

where the stiffened elastic constant is

$$\bar{c}_{44} = c_{44}^E + \frac{e_{15}^2}{\epsilon_{11}} = (c_{44} + j\omega\eta_{44}) + \frac{e_{15}^2}{\epsilon_{11}} \quad (4.8)$$

From (4.1), the potential is

$$\phi(x, z) = -\frac{e_{15}}{j\omega\epsilon_{11}} v_z = \frac{e_{15}}{\epsilon_{11}} u_z(x, z) \quad (4.9)$$

The wave vector is then

$$k_s = \alpha - j\beta = \sqrt{\left(\omega \sqrt{\frac{\rho}{\bar{c}_{44}}}\right)^2 - \left(\frac{n\pi}{h}\right)^2} \quad (4.10)$$

The attenuation coefficient can then be derived as

$$\alpha^2 = \frac{\rho}{\bar{c}_{44}} \frac{\omega^2 - \left(\frac{n\pi}{h}\right)^2 \left(\frac{\bar{c}_{44}}{\rho}\right)}{1 + \left(\frac{\omega\eta_{44}}{\bar{c}_{44}}\right)^2} \left\{ 1 - \left[ \frac{\omega^2 \left(\frac{\omega\eta_{44}}{\bar{c}_{44}}\right)}{\omega^2 - \left(\frac{n\pi}{h}\right)^2 \left(\frac{\bar{c}_{44}}{\rho}\right)} \right]^{1/2} \right\} \quad (4.11)$$

Mechanical damping dominates wave attenuation if temperature is kept constant. The viscosity of AlN moduli falls in the range of  $0.1-1 \text{ Ns/m}^2$ <sup>31</sup>. Only fundamental mode is considered since high-order modes experience large damping. The attenuation constant is then calculated to be about  $8.834 \times 10^4 \text{ Np/m}$ . Assuming the AlN is uniformly grown with no internal scattering defects, then the energy attenuation is

$$|S_{21}^M(\text{dB})|^2 = -20 \cdot \log(e) \cdot \alpha \cdot \Delta x \quad (4.12)$$

$$\text{if } \Delta x = 10 \text{ } \mu\text{m, then } |S_{21}^M|^2 = -7.6 \text{ dB}$$

$$\text{if } \Delta x = 25 \text{ } \mu\text{m, then } |S_{21}^M|^2 = -17.5 \text{ dB}$$

$$\text{if } \Delta x = 50 \text{ } \mu\text{m, then } |S_{21}^M|^2 = -35 \text{ dB}$$

Therefore the minimum TFR edge to edge separation to suppress the stiffened shear wave is about  $50 \text{ } \mu\text{m}$ . Pure shear mode is exponentially decayed along the wave propagation direction. However the actual wave phenomenon is quite complicated. These stiffened waves are not only pure shear mode, but also quasishear or quasilongitude plate modes. These lamb modes are coupled through the free boundary. Because of the anisotropic electric field, these lamb waves behave as flexural modes. At high frequency and small plate thickness some of these modes are tightly bound to the surfaces of the plate and their velocities approach degeneracy which makes them behave as quasi-Rayleigh waves. Wave phenomena will become even more complicated if the electrical edge field is considered. Mode analysis by using partial wave, transverse resonance or mode analysis methods<sup>52,52</sup> is then becomes tedious and is not easily implemented. Numerical analysis is thus required.

### Transient Finite Element Analysis

FEM is a powerful numerical tool which can be applied in modeling wave propagation in elastic and piezoelectric media. It has been extensively used in areas such as nondestructive evaluation area, engineering electromagnetics and mechanics.<sup>54-56</sup> Full FEM analysis has recently studied by Lerch in piezoelectric transducers.<sup>25</sup> As discussed in Chapter 2, large amount of computing time, much manpower and complicated algorithms are required in the implementation which is beyond the time scope of this study and is not the purpose of this study. In order to manufacture and experimentally test the TFR array concept, an axisymmetric two-dimensional transient FEM, which was originally used in ultrasonic evaluation,<sup>55</sup> is developed here to study wave propagation in the TFR array structure. As in the analytic analysis, the non-electroded area between TFRs is considered as a mechanically-free anisotropic plate in which piezoelectricity is incorporated in the stiffened elastic constants. The electric field is treated as equivalent surface traction force in one TFR (transmitter TFR). The general discretized finite element equation in matrix form can be derived as<sup>55</sup>

$$M\ddot{U}_i + D\dot{U}_i + KU_i = T \quad (4.13)$$

where  $M$ ,  $D$ ,  $K$ ,  $T$ ,  $U_i$  are respectively global mass, damping and stiffness matrix, equivalent boundary traction force, and the displacement vector. The displacement  $u_i$  in a discretized element is related to its global value by

$$\left[ u_i(x, z, t)^e \right]_i = [N(x, z)]_I U_{ii}^e(t) \quad (4.14)$$

where  $[N(x, z)]_I$  is called the shape function, which is continuous across each element boundary. The time derivative of the global displacement matrix can be discretized by applying the central difference approximation for the second time

derivative and the backward difference approximation for the first order time derivative

$$\ddot{U}_t = \frac{1}{(\Delta t)^2} (U_{t-\Delta t} - 2U_t + U_{t+\Delta t}) \quad (4.15)$$

$$\dot{U}_t = \frac{1}{(\Delta t)} (U_t - U_{t-\Delta t}) \quad (4.16)$$

substituting (4.15) and (4.16) into (4.13) yields

$$\frac{1}{(\Delta t)^2} M U_{t+\Delta t} = T - \left( K + \frac{1}{\Delta t} D - \frac{2}{(\Delta t)^2} M \right) U_t + \left( \frac{1}{\Delta t} D - \frac{1}{(\Delta t)^2} M \right) U_{t-\Delta t} \quad (4.17)$$

where only the global mass matrix is presented in the left side. The mass matrix is usually a block diagonal matrix. For the AIN plate, it is a product of unit block diagonal matrix and a constant related to node mass density and shape function. By applying the mass conservation principle, the mass matrix can be lumped to a diagonal form. The time iteration of displacement can then be realized as

$$U_{t+\Delta t} = (M^D)^{-1} \Delta t^2 F - [(M^D)^{-1} (K + \frac{1}{\Delta t} D) \Delta t^2 + 2] U_t + [(M^D)^{-1} (\Delta t) D - 1] U_{t-\Delta t} \quad (4.18)$$

where the computer-intensive matrix inversion is thus avoided, which allows the use of this method to handle problems of large objects. The calculation geometry is shown in Figure 4.5 in which the geometry and boundary are all axisymmetric. Lateral free-boundary conditions are also enforced, which are closer to the real

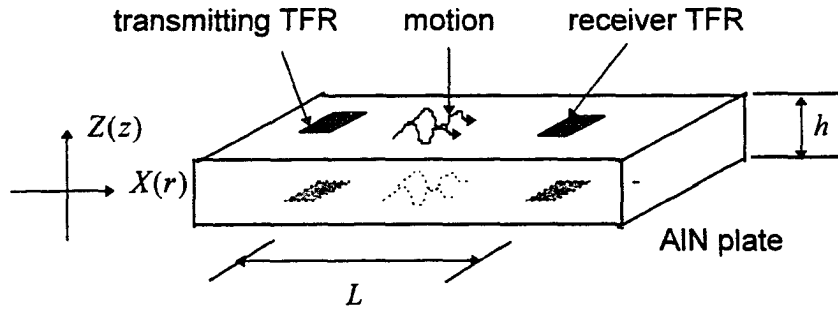


Figure 4.5 Schematic calculation geometry

$$c = \begin{bmatrix} c_{11} & c_{13} & 0 & c_{12} \\ c_{12} & c_{33} & 0 & c_{13} \\ 0 & 0 & \bar{c}_{44} & 0 \\ c_{12} & c_{13} & 0 & c_{11} \end{bmatrix} \quad (4.18)$$

device structures since TFRs are usually sawed in about  $3 \text{ mm}^2$  dice. Finite transverse dimension is thus expected. The equivalent traction force stands for the applied electric field which is asymmetrically distributed along the TFR thickness direction. The anisotropic elastic constant tensor is correspondingly written as (4.18). Piezoelectricity is incorporated in the stiffened elastic constant. The viscosity constant tensor is assumed to have the same symmetry as that of the elastic constants. Standard AIN elastic, piezoelectric constants and density listed in Appendix IV are used in the model. A sinusoidal traction-force with central frequency of 1GHz is applied through symmetric axis which mostly creates asymmetric flexural modes. Iteration time step is chosen as less than the transit time for the fastest wave (longitude wave) traveling across the shortest element node to satisfy the stability requirement. Since the transverse longitude wave has a velocity of about  $10^4 \text{ m/s}$ , the interaction time step is then chosen to be 25 ps. It has been found that 12 to 16 element nodes per shortest wavelength can assure calculation

accuracy which is similar to the finite difference method used in Chapter 2. Figure 4.6 shows the modeled results of normalized displacement magnitude vs. transverse distance in a  $5\ \mu\text{m} \times 100\ \mu\text{m}$  device geometry. One can find that wave amplitude does not decrease exponentially, which is quite different than the pure shear wave. The characteristics of transverse resonance waves due to free boundary is also clearly shown in the amplitude (oscillation along lateral direction) which can not be observed in pure shear wave. Wave propagation along transverse direction is also shown in the three-dimensional transient plots shown in Figure 4.7 where displacement magnitude along mid-plane of AlN plate is calculated at two different observation times. The calculated dimension is  $5\ \mu\text{m}$  by  $50\ \mu\text{m}$ . A trigonometric dependence of displacement amplitude in  $Z$  direction can also be

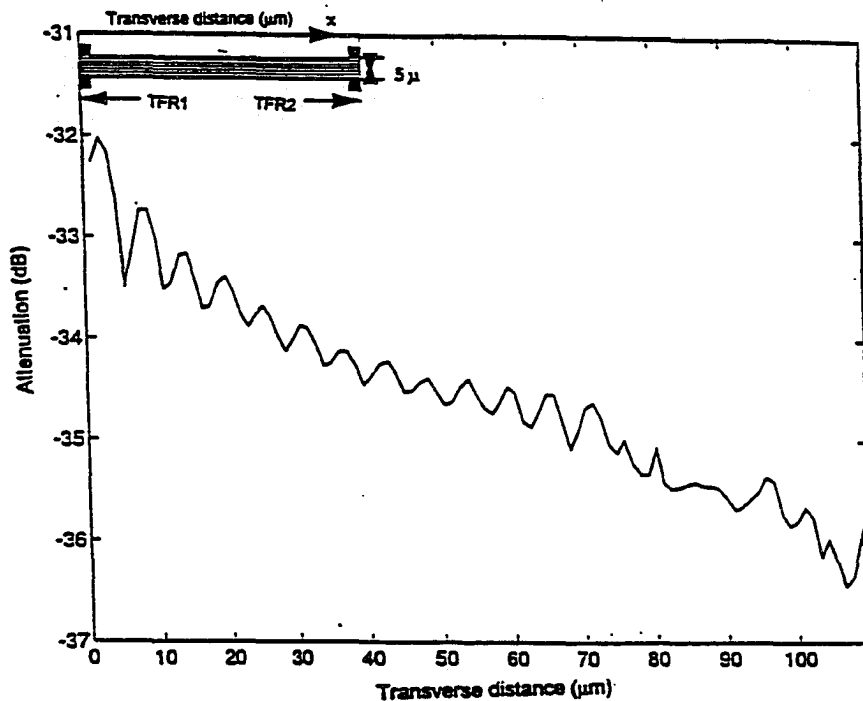


Figure 4.6 FEM modeled displacement attenuation along transverse direction

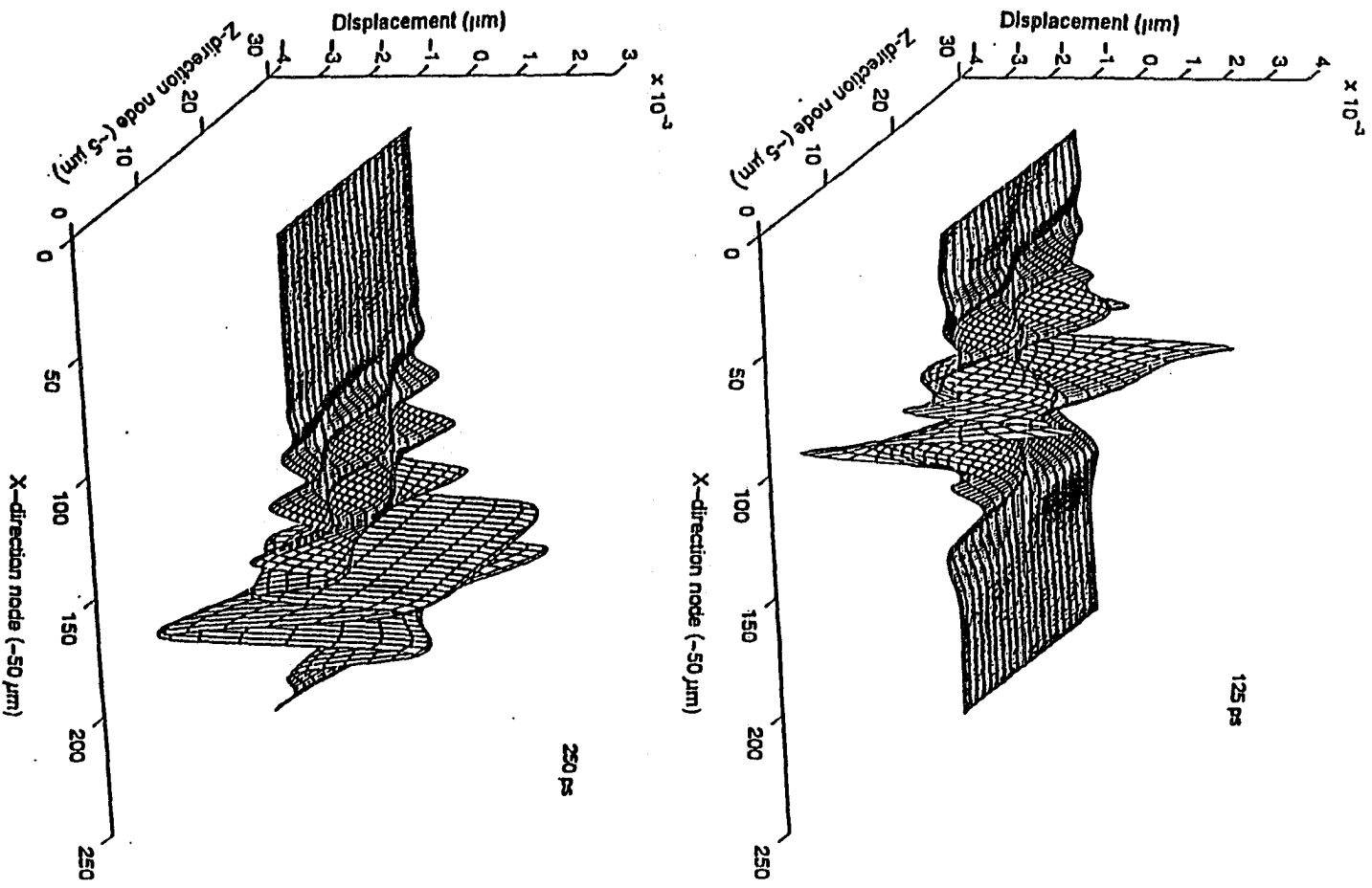


Figure 4.7 3D wave motion along AlN plate

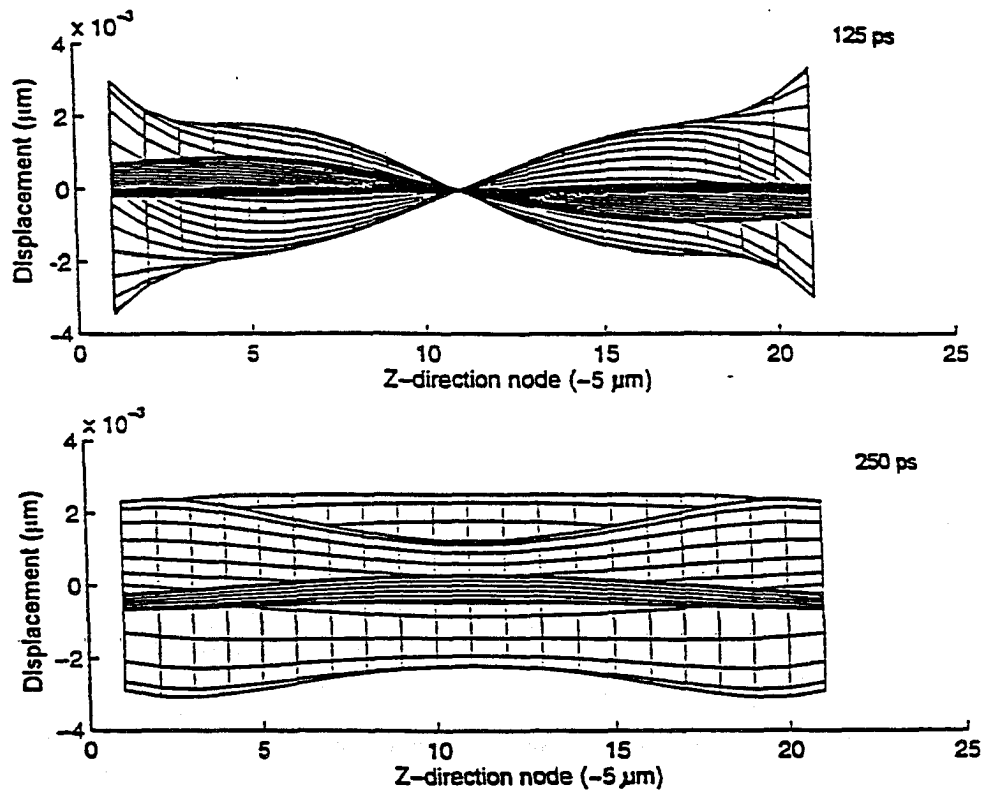


Figure 4.8 Wave motion view along Z direction

found in Figure 4.8. The asymmetric displacement field created by the electrical field shows strong flexural wave characteristics. Compared to the analysis of pure shear mode, FEM methods are more appropriate to interpret actual wave propagation inside a thin AlN plate since multimodes and material anisotropy are included in the modeling. FEM results should thus be used as a measurand to effectively isolate the adjunct TFRs.

#### Array Electromagnetic Isolation

The electromagnetic crosstalks arise from near-field L-C coupling due to metal fringe electric field and possible device radiation. AlN effective permittivity and electrode width due to finite electrode thickness can be expressed as<sup>57,58</sup>

$$w_{eff} = w + \frac{t}{\pi} \left(1 + \ln\left(\frac{2h}{t}\right)\right) \quad (4.19)$$

$$\epsilon_{eff} = \frac{\epsilon_r + 1}{2} + \frac{\epsilon_r - 1}{2} \left(1 + \frac{12h}{w_{eff}}\right)^{-1/2} \quad (4.20)$$

where  $h$  and  $t$  are the AlN thickness and electrode thickness. If the electrode is thicker, permittivity has less effect and the field has large fringing. Electrode thickness used in TFR sensor is usually several thousand angstroms and AlN thickness is about 5 microns. Also sputtered AlN films possess low dispersion.<sup>59</sup> The fringe field effect is therefore a minor effect in terms of electrical coupling. By standard microwave design, the distance between the top electrodes of two TFRs should be chosen to be about three times that of the dielectric thickness in order to suppress edge effects<sup>60</sup>. This suggests that about 15 microns edge to edge separation between TFRs is a minimum distance to decouple the electrode edge evanescent field. This shows that electrode edge fields have minor impact on the TFR array design.

However electromagnetic radiation caused by the device, bonding-wire, bonding-pad and line-discontinuities may also exist, specially in TFR-controlled oscillator systems. Radiated power from one TFR may convert to spurious modes in another TFR and injection-lock the adjunct oscillator, which will deteriorate system operation. The radiation from bonding-wire (like current dipole) can be substantially diminished by working at low power level and orientationally patterning the bond-pad. However, bond-pads in TFR are designed by trade-off the pad stray capacitance and the film resistance. In order to match 50 ohms the width of the bond-pad should be chosen to be close to AlN thickness, but that may cause difficulty with wire-bonding and increase film series resistance, especially in the microwave frequency range. If the width is much wider than the AlN thickness, then stray capacitance becomes dominating and changes TFR resonance

characteristics. At TFR frequency range, other electromagnetic coupling from surface waves and transverse resonance waves is very small since those coupling frequencies are around millimeter-meter wavelength range at AlN thickness. Because TFRs used in microsensors are operated at low-power levels, feed-through crosstalks should not happen. Although electromagnetic wave propagation may also exist in the AlN plate, the condition stated as below in the TFR frequency range usually holds

$$k_z^2 \approx \frac{\rho\omega^2}{c_{IJ}} \gg \omega^2 \mu \epsilon_{ij} \quad (4.21)$$

Thus quasistatic approximation can be applied where the rotational or electromagnetic field inside the piezoelectric plate is negligible. The far-field radiation through the AlN film should be greatly reduced since the loss tangent from the AlN film is strongly experienced. TFR VSWR is usually experimental measured about 1.25 - 2.0, which means the overall match condition is roughly maintained. Electromagnetic radiation and scattering from TFR devices on the same AlN membrane should not result in significant crosstalks. The major crosstalk is then caused by acoustic waves. However, it may not be true for a TFR array on different AlN membrane because boundary conditions are changed. Near-field coupling and radiation may contribute significant crosstalks.

These acoustic and electromagnetic coupling effects should be considered in design array masks. The circuit board should also be well designed, specially in TFR-controlled oscillators.

## CHAPTER 5. TFR ARRAY PROCESS AND CHARACTERIZATION

## Mask Design and Process Characterization

As discussed in Chapter 4, an array mask should consider those wave crosstalks. Notice that TFR sensor processing is basically a bulk micromachining process. Two-sided structures are often used in sensor technology by performing anisotropic silicon etch techniques. Mask design should then include photolithographic tolerances and etching anisotropy. The usual alkaline etchants used in micromachining are EPD (ethylene diamine, pyrocatechol and water),<sup>61</sup> KOH (potassium hydroxide, propanol and water),<sup>62</sup> hydrazine,<sup>63</sup> and choline,<sup>62</sup> with EPD and KOH used extensively. Choosing different etchants depends on the selection of specific masking and etch-stop materials, as well as geometric dimensions. Figure 5.1 shows the etch window diaphragm in the TFR array. Each back-side window is patterned where sidewalls are gradually formed along the etch-resistant (111)

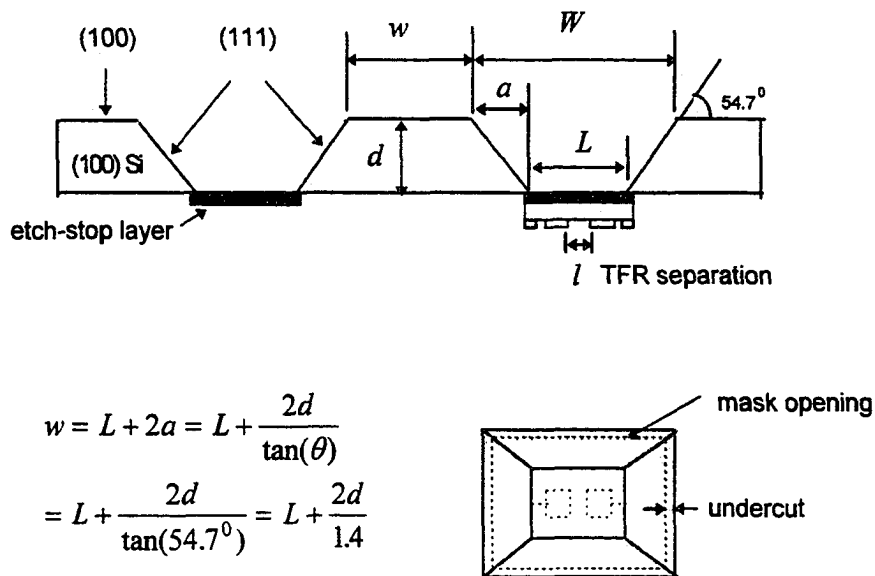


Figure 5.1 Anisotropic etch window diaphragm in TFR array (not to scaled)

planes, while (100) etch fronts progress downward with time. Window mask openings should also allow for undercut effects, especially in the convex corners. Since TFR arrays are designed on the same AlN membrane as the top metal mask, wave acrosstalk effects must be considered in addition to the functionality of individual TFRs. The distance to decouple plate wave crosstalks depends on the acceptable crosstalk level and AlN viscous damping which is strongly dependent on material Q and processing parameters. Usually, about 40 dB attenuation is expected in order to decouple individual TFRs. From the analysis in Chapter 4, the minimum edge-to-edge separation distance for SW array should thus be chosen at around 300 - 400  $\mu\text{m}$ . The routinely used silicon wafer (3 in) has thickness ranging from 14 to 16 mil. With the consideration of the sidewall effects and photo tolerance, the minimum distance between TFRs on a DW array is determined by the smallest width ( $w$ ) between back-side windows as shown in Figure 5.1. This minimum distance should also be sufficient to decouple wave crosstalks. In order to verify the model analysis, actual masks are designed such that the separation distance between adjunct TFRs is swept from 20  $\mu\text{m}$  to 1.4 mm in a SW array, while that distance for DW array is 820  $\mu\text{m}$  to 1.2 mm. Another reason to do this is to find out how many TFRs can be housed in a single SW array dice, in other words, to experimentally find out how mechanically strong the AlN membrane is. About 150  $\mu\text{m}$  design margin is used to prevent the leaky waves from propagating through substrate silicon. These design data are summarized in Table 5.1.

Table 5.1 Data summary of mask design

	SW array	DW array
d ( $\mu\text{m}$ )	350 - 406	350 - 406
a ( $\mu\text{m}$ )	240 - 280	240 - 280
l ( $\mu\text{m}$ )	20 - 1400	820 - 1150
w ( $\mu\text{m}$ )	depend on dice	20 - 350
L ( $\mu\text{m}$ )	1120 - 2500	~700
W ( $\mu\text{m}$ )	1300 - 2760	1180 - 1260

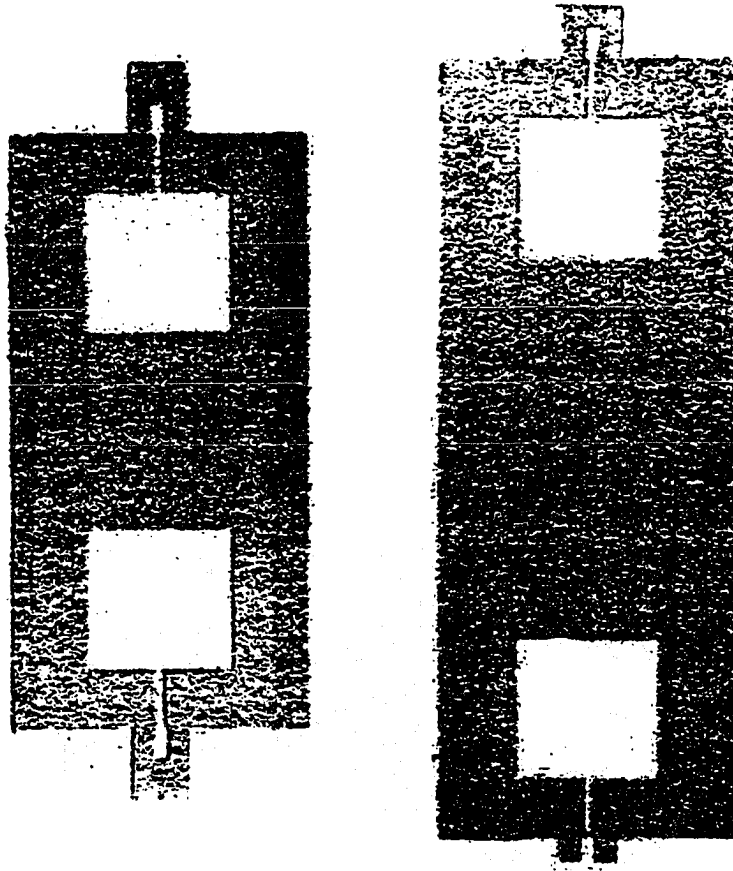


Figure 5.2 A micrograph of actual TFR array (top view)

The top-view of a fabricated TFR array is shown in Figure 5.2. Two SW TFRs (left) and two DW TFRs (right) are aligned in the same direction to perform on-wafer two-port probing and to help further decouple possible electromagnetic crosstalk. The array geometry after processing was defined well within design specification by using this mask set. It was also found that the AlN membrane can extend to a large width to thickness ratio. The maximum ratio of 500 is mechanically stable under regular sensor testing operation, which is much higher than the observed ratio of

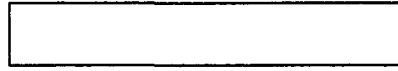
ZnO<sub>2</sub> TFRs (~60)<sup>64</sup>. This shows that six TFRs can be patterned in the SW array structure on a 3 mm x 3 mm dice and the present TFR test fixture can still be used.

Although surface micromachining techniques can further reduce the over-all device size and increase packing density (which offers increased throughput and complexity), there are important factors that keep bulk micromachining the current technology for bulk resonators. TFR sensors are required to work in environments that are hostile to microstructures. Surface-machined features are sensitive to environmental factors such as particles, humidity, and cleanliness. Specially designed packages are often required which can substantially increase device cost. Sacrificial layers and etching are usually required to perform surface micromachining. But those suspended elements are very easily affected by mechanical perturbation such as pressure and acceleration (actually these two kinds of sensors are made by surface-micromachining technique), which may increase the difficulties of processing resonator-related sensors. Also sacrificial etching usually undergoes longer etch times which may add constraints to etch selectivity.

Bulk micromachining techniques with standard TFR technology was therefore used for this thesis work. The major process flow is shown in Figure 5.3. The starting material is a 3" (100) single-crystal silicon. The bottom metallization is a stacked chrome/aluminum layer. Aluminum is mainly used for bottom metallization and as a nucleation layer for the AlN piezoelectric film, while chromium is used for adhesion purposes and etch stops for the window anisotropic etch. 200-500 Å Cr with 1000-2000 Å Al is routinely used. This bottom metallization also helps confine the electric field within the device region which is important for both desired piezoelectricity and less electrode fringe fields. Standard chrome and aluminum etchants are used for etching.

The AlN piezoelectric film is the backbone of TFR technology and has been studied and applied to devices for the last decade at the MRC. Magnetron sputtering techniques are used. In order to grow high quality films, precautions have been taken with process issues such as film crystal structure, grain size, preferred

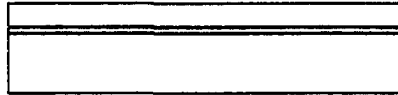
(1) (100) N-type Si wafer



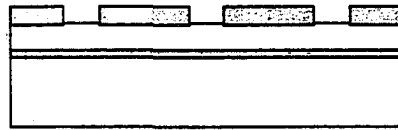
(2) bottom metallization Cr/Al  
and patterning



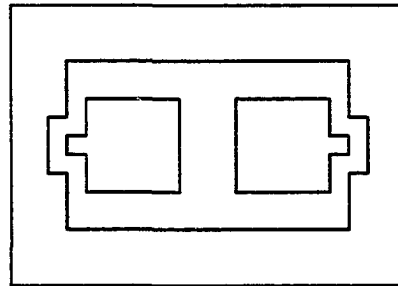
(3) planar sputtered AlN film



(4) top-side metallization Al,  
or Al/Cr/Au and patterning



(top-view)



(5) back-side pattern and SiO<sub>2</sub> etch

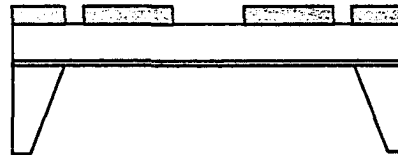
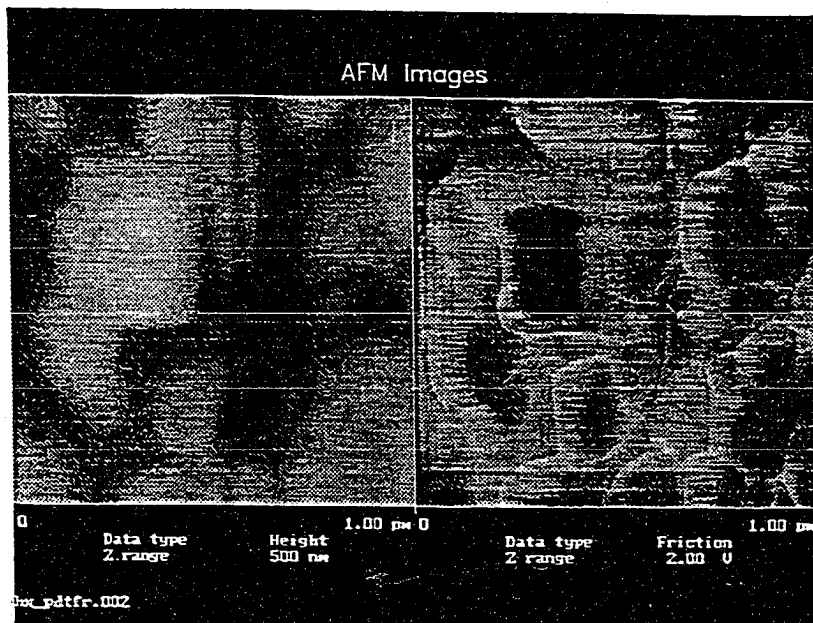
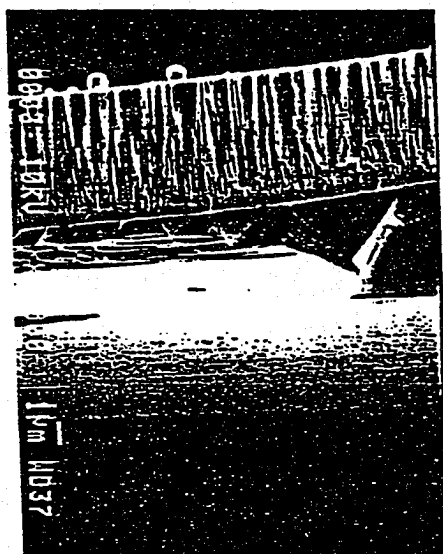


Figure 5.3 TFR array process flow

orientation, stoichiometry, stress and surface morphology. A c-axis perpendicular AlN film is required in TFR sensors utilizing longitude modes. Process parameters such as nitrogen pressure, temperature, power density and substrate bias must be optimized to achieve the desired characteristics. According to the famous Thornton structure zone model,<sup>65</sup> good piezoelectric properties under low-temperature growth can be achieved in zone-T range where a dense array of columnar/fibrous crystals with the grains size of several ten to several hundred nanometers is usually formed.<sup>59,66-68</sup> Film orientation is sensitive to the direction of coating flux because adatoms do not have sufficient surface mobility under low temperature. This is the reason c-axis tilt AlN films can be grown if the sputtered flux arrives at the surface with a tilt angle. Films grown under low nitrogen contents prefer c-axis normal orientation because of less gas-phase scattering. High power operation can promote high growth rate but also effects film structure. Substrate bias can substantially alter film structure. In general, it will help the structure transition from zone-1 to zone-T with low temperature growth. Film stress grown by low pressure sputtering is mostly compressive and increased in thickness, especially at low temperature.<sup>69</sup> These intrinsic stresses are strongly dependent on process parameters and have profound effects on resonant performance such as frequency instability. Although a stress-relief layer (SiO<sub>2</sub>, or Si<sub>3</sub>N<sub>4</sub>) can be incorporated to reduce stress, the additional capacitance series with the motional path of the TFR will decrease device Q. Trade-off should be considered in the implementation. Completely understanding the relation between process parameters on AlN film crystallized structure and piezoelectric properties is still unclear and under continuing study. Figure 5.4 shows a typical SEM cross-section and surface morphology of a recently grown AlN film. Columnar crystals are clearly shown which suggests that film orientation is mostly (0002) with c-axis perpendicular to the substrate. However surface morphology shows that the AlN surface is not smooth, with the roughness on the order of 0.5 μm. Also seen are the large crystals with zone-1 alike structure which may arise



a) AlN surface morphology



b) SEM cross-section picture

Figure 5.4 AlN surface morphology and SEM cross-section

from low adatom surface mobility. Increased temperature and application of appropriate substrate bias can improve film quality and reduce resulting surface roughness and voided grain boundaries.

Top metallization usually uses stacked Cr/Au metal for the polymer sensor and Cr/Au/PdNi metal for the hydrogen sensor, in which Au is used as additive catalyst for the Pd layer. The electrode conductive loss for thin metallization and acoustic loss for thick metal has been balanced in trying to get TFRs with low resistance, high Q and fast response. Metal film resistivity is  $2.7\text{-}3\ \mu\Omega\cdot\text{cm}$  for Al and  $3.4\text{-}5\ \mu\Omega\cdot\text{cm}$  for Au<sup>70</sup>, assuming 1000 Å metallization is used. Series resistance from the bonding strip can then be calculated as about  $2\ \Omega$  for Al and  $2.5\ \Omega$  for Au. For PdNi that value will be up to  $5\ \Omega$ . Also the bond-pad and bonding-wire contribute a fair amount of series inductance. These additional resistances and inductances will deteriorate resonator Q and offset series frequency. This is the major disadvantage of using an edge-support structure with wire-bonding.

After the process is completed, on-wafer two-port probing of the TFR array is conducted by using a Cascade Microtech microprobe station. Error correction is made by using full two-port calibration. One-port return loss and two-port insertion loss were measured using an HP 8753 network analyzer. The coupled network between adjunct TFRs is actually a mechanical monolithic filter with a typical response shown in Figure 5.5, in which bandpass filter characteristics are clearly shown. If the adjunct TFRs are placed closely, a low-insertion monolithic filter should be constructed. The TFR sensor array is actually designed to decouple the filter responses. The measured and modeled attenuation is shown in Figure 5.6 in which the ripped measured data results because individual TFR arrays are located on different positions on a tested wafer. Non uniformity is expected. The measured and modeled results are in close agreement, which implies that most crosstalks arise from acoustic plate wave coupling. Attenuation of TFR arrays on the same AlN membrane near resonant frequency is below 40 dB if the TFR edge-to-edge

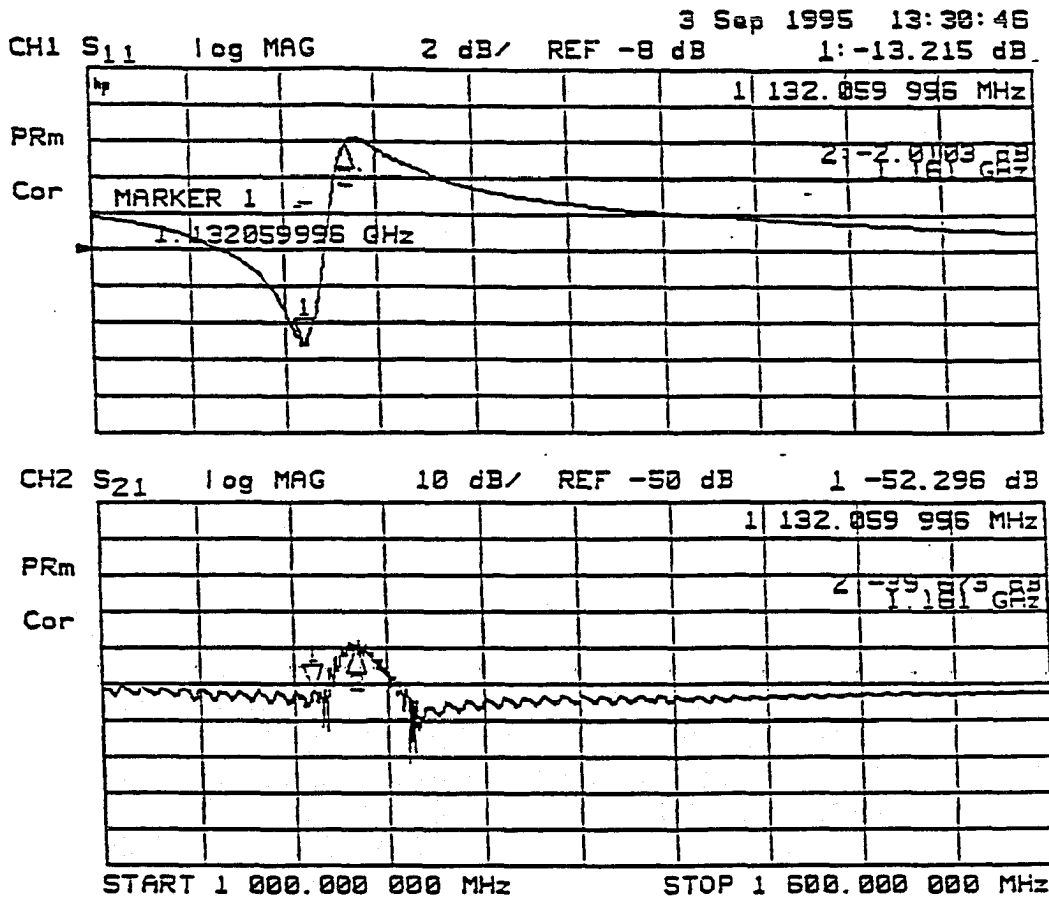


Figure 5.5 Bandpass filter response on a TFR array

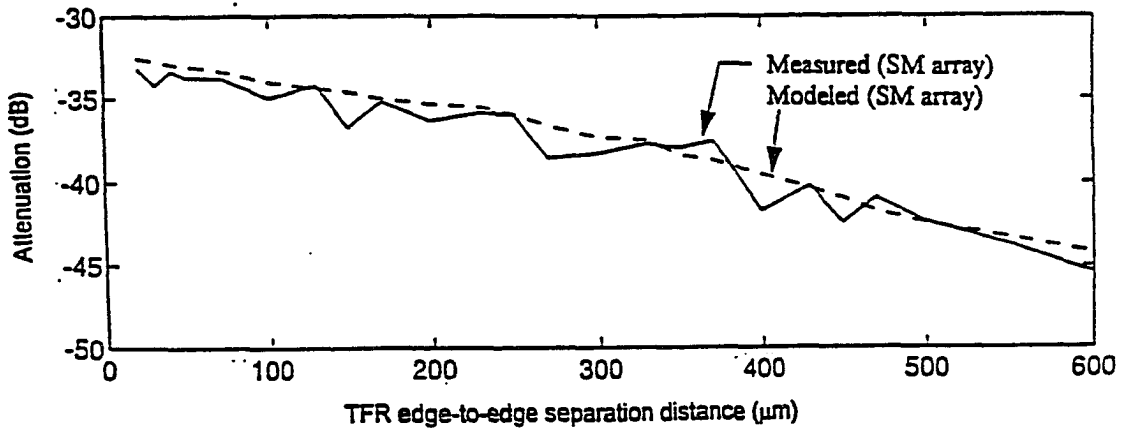


Figure 5.6 Measured and modeled attenuation on a SW array

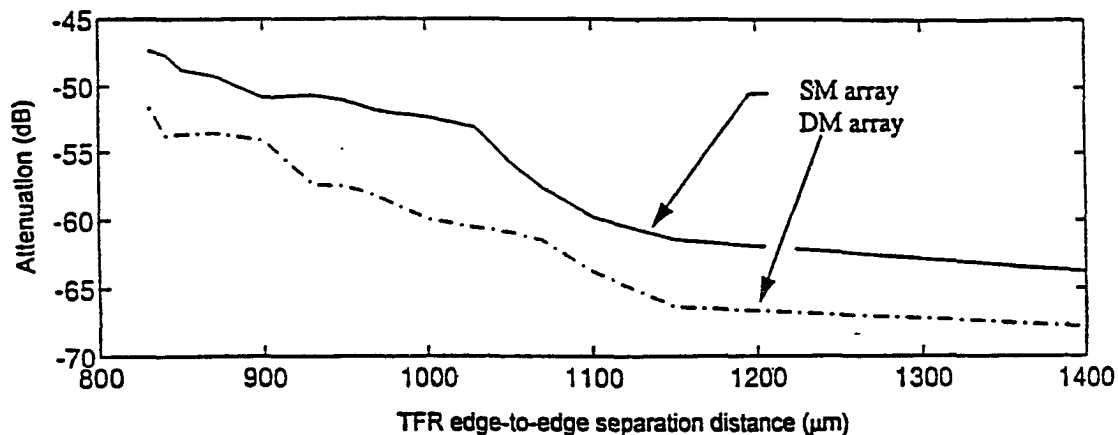


Figure 5.7 Attenuation comparison between SW and DW array

separation is greater than 400 microns. Figure 5.7 shows the comparison of measured attenuation between SW arrays and DW arrays. It is shown that the DW array has larger attenuation because leaky waves also propagate and attenuate in silicon substrates. This is why a margin of error in mask design is allocated to diminish these leaky waves.

#### TFR Array Characterization

The purpose of constructing a TFR array is mainly to compensate temperature-induced response drift and to perform vapor or analyte pattern recognition in a multicomponent analyte system. Temperature-induced drift is because of the fluctuation of temperature coefficient (TC) and material elastic, piezoelectric and dielectric properties of the substrate TFR composite and analyte coating. Table 5.2 lists the TCs for some commonly used materials in the TFR composite,<sup>59,71</sup> in which one can find that the TC of AlN is larger than that of the usually used metal films. These changes may also induce film internal stress fluctuation which creates additional frequency variation. In polymer sensor applications, temperature changes may vary polymer film status and result in glass

Table. 5.2 Temperature coefficients for common materials used in TFR composite

temperature coefficients ( $^{\circ}\text{C}^{-1}$ )	
AlN	$(7.6 - 19) \times 10^{-5}$
Al	$2.4 \times 10^{-5}$
Au	$1.43 \times 10^{-5}$
Pd	$1.18 \times 10^{-5}$
Cr	$0.68 \times 10^{-5}$

transition which may make responses unpredictable. Therefore, temperature compensation should include both the substrate TFR composite and analyte coating. In this study, a polymer coated TFR array was used to characterize temperature effects and demonstrate temperature compensation. The selectivity characterization was also conducted by using a polymer coated TFR array with 400  $\mu\text{m}$  separation distance between two TFRs. The difference of resonant frequency of two TFRs was measured at 0.66 MHz, which means the TFR composite has fairly uniform thickness within the array geometrical range. A TFR array die (with four TFRs) was first wire-bonded and mounted onto a matched TFR test fixture (50 ohms). The electrical delay and resistance caused by the test fixture is 303 ps and 1.2 ohms. A temperature-controlled test box with gas blending system is used to house the test fixture. Nitrogen purging gas is used in order to reduce humidity effects. Resonator data acquisition was through an HP 8753 network analyzer and calculated by the HP resonator software. The array test setup is schematically shown in Figure 5.8. Temperature-induced drift on a polyisobutylene (PIB) coated TFR is shown in Figure 5.9. The temperature effect on resonant frequency of longitudinal TFR with PIB film is around 8 - 10 ppm/ $^{\circ}\text{C}$  and is smaller than that for shear mode in the AlN/Si(p<sup>+</sup>) temperature-compensated structure<sup>34</sup>. This indicates

that longitudinal moduli is more temperature-resistant than shear moduli. Temperature drifting in the lab testing environment was often observed within  $0.3^{\circ}\text{C}$ , which produce response drifting of the same level as the device noise level. This will deteriorate the TFR detection limit. An array concept is thus required to compensate for these temperature effects. Figure 5.10 shows the S-parameter (Smith chart) variation before and after coating the PIB. The frequency shifts due to the PIB film are 1.1 MHz (TFR1) and 1.2 MHz (TFR2). The resistance increases about 3.2 ohms and 3.6 ohms, respectively. According to the analysis in Chapter 3, the PIB film can be treated as a perfectly acoustically thin coating with a calculated thickness of 26 nm and 28 nm respectively. While exposed to hexane vapor, TFR responses are most due to mass loading of these acoustically thin PIB films. Figure 5.11 shows temperature effects on individual TFR responses. The experimental sequence was  $30^{\circ}\text{C} - 45^{\circ}\text{C} - 23^{\circ}\text{C}$ . One can find that response on a single TFR is highly dependent on environmental temperature. The higher the temperature is, the smaller the response. Absorption-desorption equilibrium is kept at low analyte

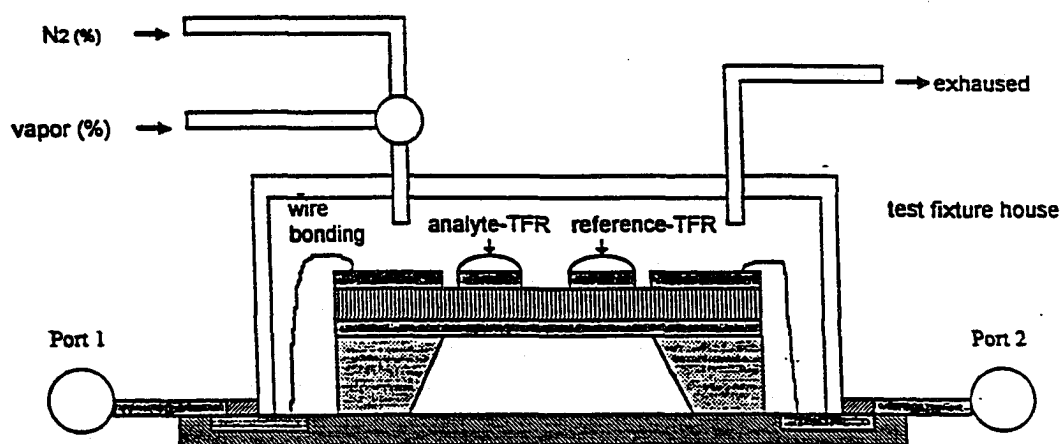


Figure 5.8 Array testing schematic diagram

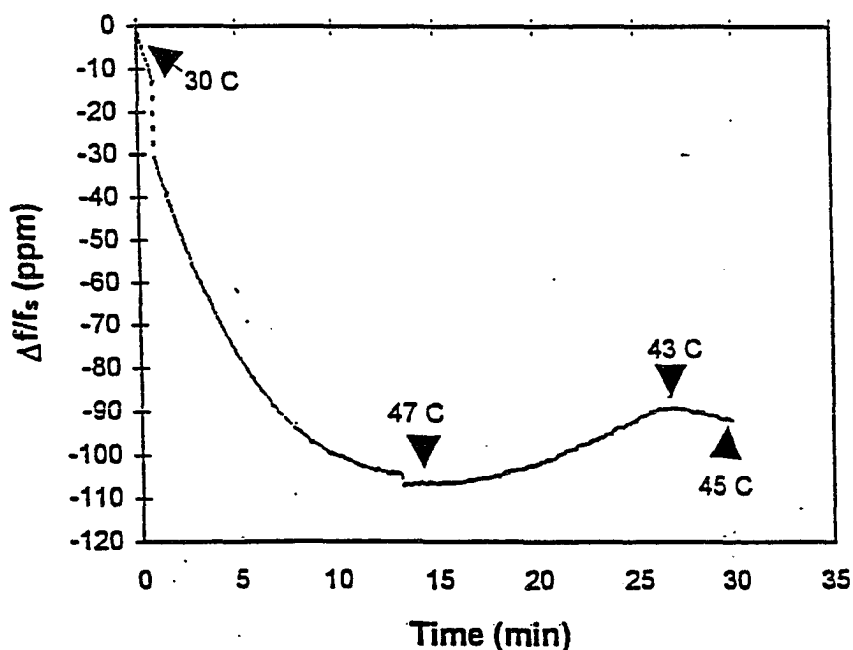


Figure 5.9 Temperature effect for PIB-coated TFR

concentration at high temperature because analyte molecules have large mobility and prefer the desorption process. The response difference between two TFRs at the same temperature is within the TFR noise level. However, the differential responses from these two TFRs remain almost unchanged, as can be seen from Figure 5.12, in which the sensitivity ratio between two TFRs is about the same at two different temperatures. This is a very important result, and means that TFR arrays can be effectively used to compensate temperature-induced drifting, even if an individual TFR has not utilized a temperature-compensation layer, such as in the AlN/Si(p<sup>+</sup>) structure. The offset at zero vapor concentration in either Figure 5.11 or Figure 5.12 is believed due to the calibration error of the system setup. The cross-over responses between 23°C and 30°C for both TFRs may be because of the perturbation of the film status since the experiment at 45°C may vary film properties, especially the PIB film glassy status. Although the static glassy transition

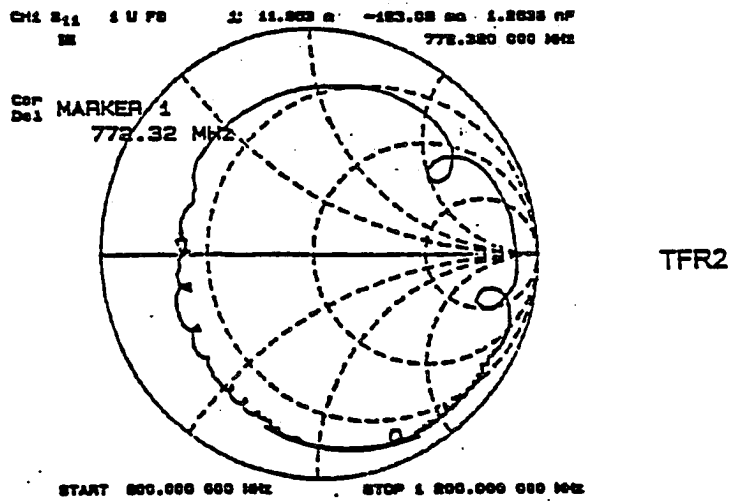
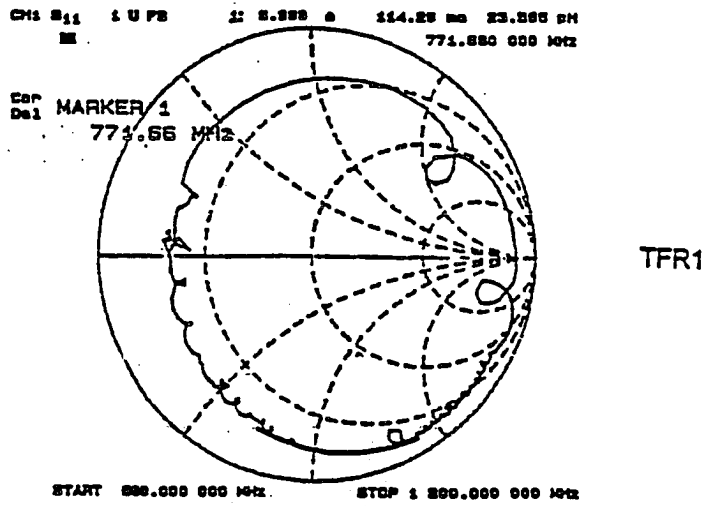
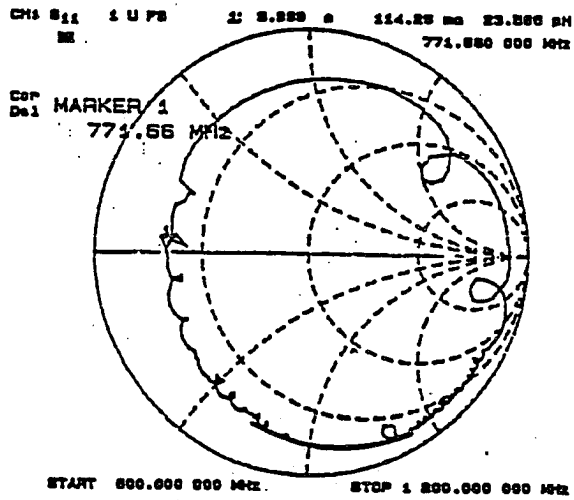
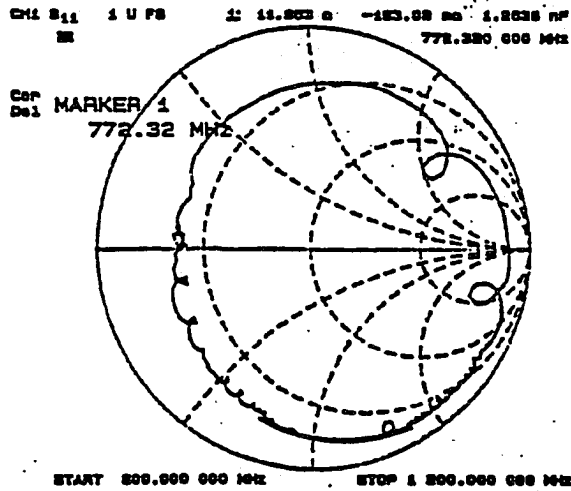


Figure 5.10 a) Smith chart before PIB coating



TFR1



TFR2

Figure 5.10 (continued) b) Smith chart after PIB coating

temperature ( $T_g^\circ$ ) for the PIB film is about  $-68^\circ\text{C}$ , the dynamic transition temperature ( $T_g$ ) is around  $40^\circ\text{C}$  at 100 MHz.<sup>6</sup>

Another important experiment is to conduct sensitivity tests with different polymer coatings on different TFRs while exposed to the same analyte vapor. To do this experiment, the coating process is very critical, in that cross-coating between two TFRs must be prevented. Since the TFR array is sized within micrometer range, the coating process was performed under microscopy. Also the spinning casting technique is not easily implemented since special mask steps have to be implemented in order to coat each TFR separately. The coating technique used in this experiment uses solution capillary effect from a microsyringe and microbrushing techniques. Although these methods are rough approaches, they can serve to demonstrate the array selectivity testing. Polymer thickness is controlled by frequently monitoring frequency shift. The thickness of the polymer coating by these methods can reach approximate uniformity over the TFR device region. One TFR was then coated with a PIB film with a thickness of 21 nm (0.9 MHz), while another was coated with PMMA film with a thickness of 23 nm (1.0 MHz). Since acoustically thin films were coated ( $R \sim 0.02$ , refer to Chapter 3), the responses were then believed to have arisen from mass loading. Figure 5. 13 shows the response of this TFR array exposed to hexane vapor. Response difference is clearly shown between two TFRs with selectivity ratios of about 3 (TFR-PIB/TFR-PMMA) that is comparable to the 9 MHz-QCM data.<sup>72</sup> This result implies that, under acoustically thin polymer films, TFRs and QCMs should give similar responses since the same amount of mass is absorbed whether high frequency TFRs or low frequency QCMs are used. This conclusion is reached under the assumption that no other effects such as thickness expansion and elastic fluctuation contribute to responses in acoustically thin polymer films. This experiment shows that a TFR arrays should be able to test the 'real' vapor or gas with a precalibrated sensitivity pattern, which makes it feasible for environmental monitoring and species detection applications.

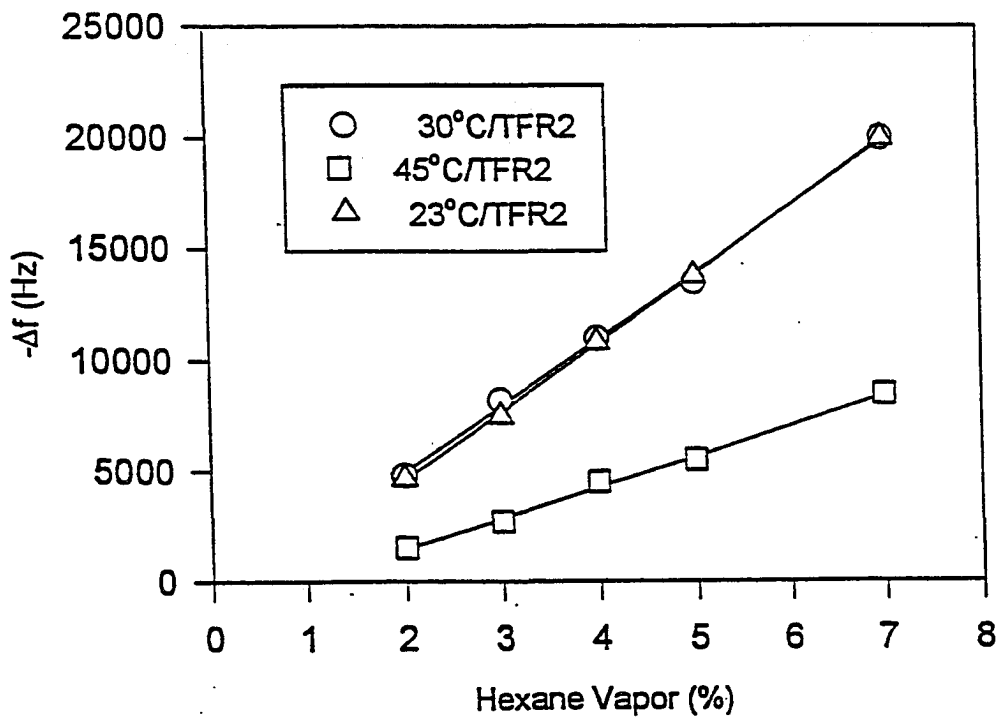
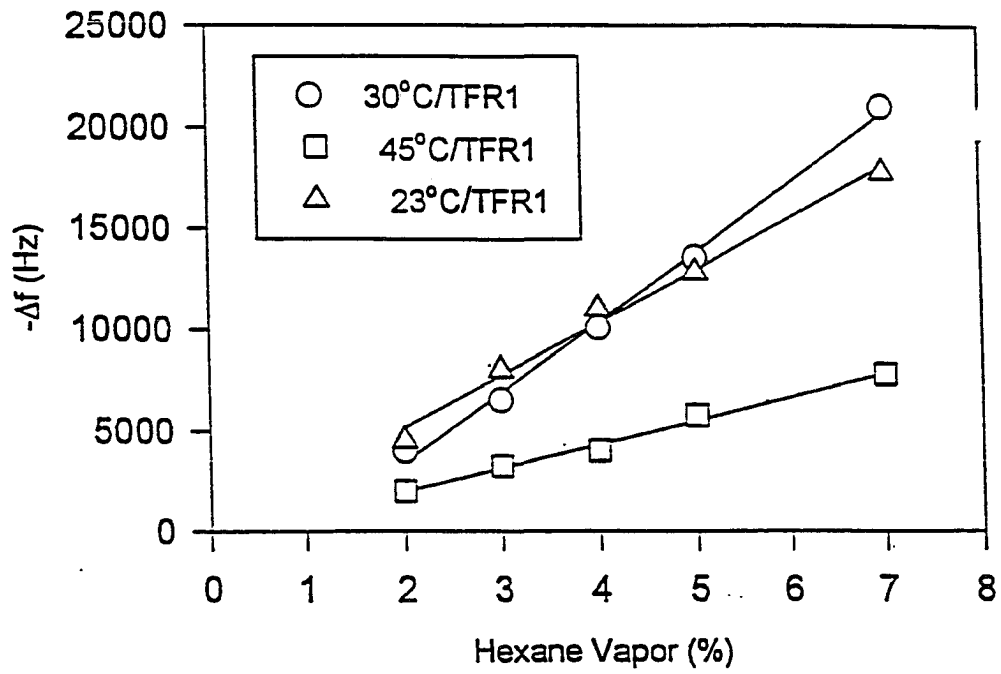


Figure 5.11 Response changes of single TFR due to temperature variation

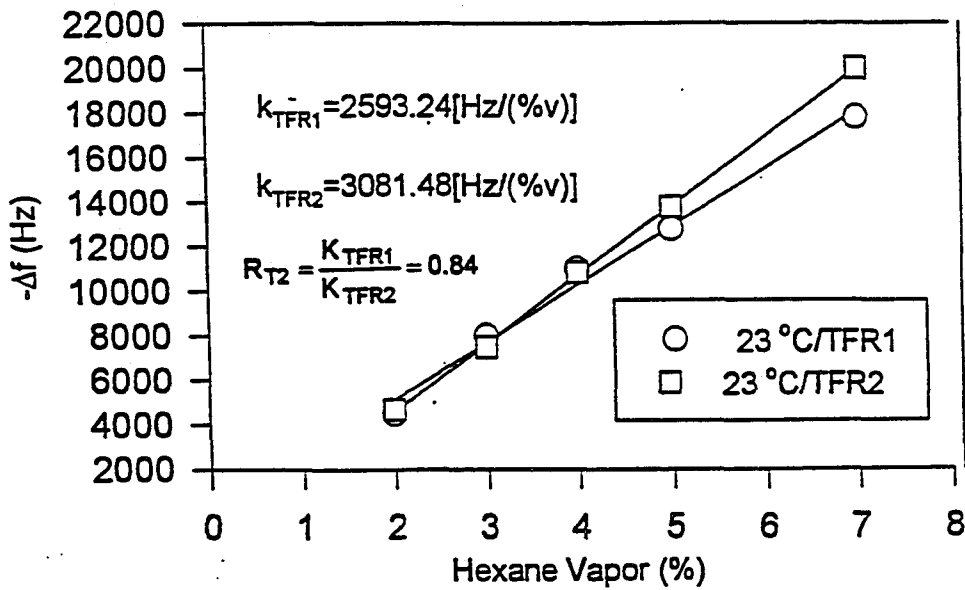
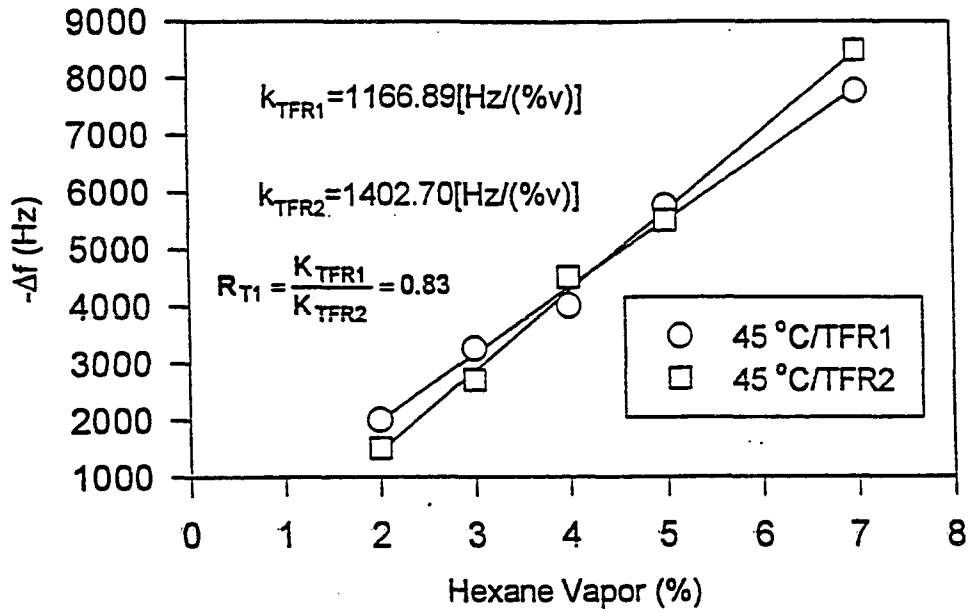


Figure 5.12 Responses of a TFR array due to temperature variation

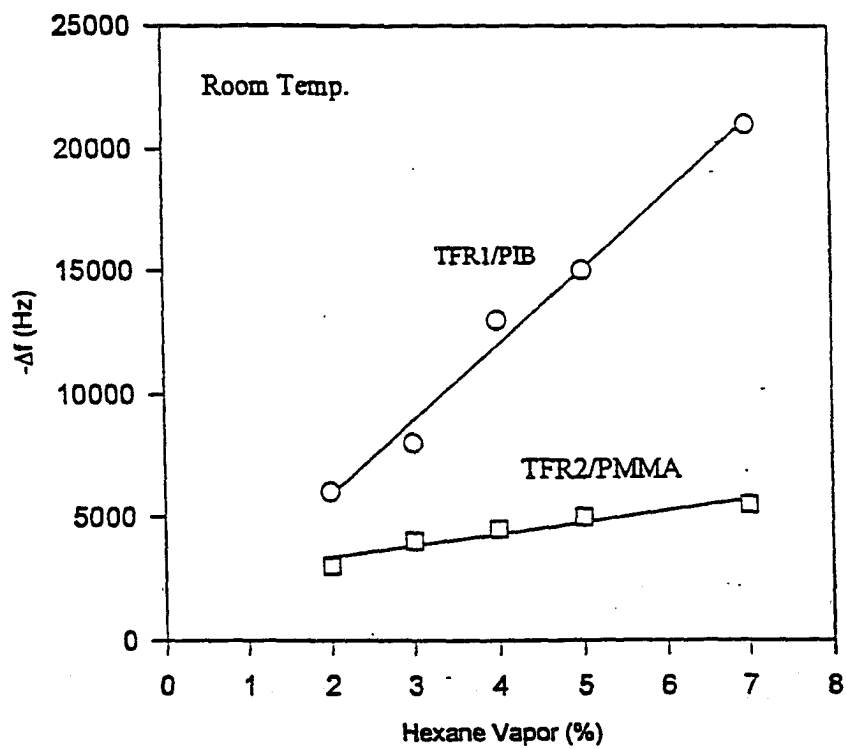


Figure 5.13 Array selectivity measurement to hexane vapor

## CHAPTER 6. SUMMARY AND RECOMMENDATIONS

The objective of this study was to theoretically and experimentally characterize microsensors using the unique bulk acoustic thin film resonators (TFRs), and to design and implement TFR microsensor arrays. By applying the developed wave model, the analysis and characterization of TFR polymer microsensors and TFR liquid microsensors has been studied and compared with the experiments. Reasonable good agreement between theoretical and experimental results were obtained which indicated the availability and applicability of the wave models. TFR microsensor arrays were also modeled and implemented along with the characterization of temperature compensation and selectivity testing. These successful models and characterizations contribute to further application development of microanalytical systems by utilizing thin film resonators.

Microsensors using thin film resonators are actually composite resonators coated with an analyte layer where the changes of mechanic properties of the coating are subjected to the exposed analyte vapor, gas or liquid. Acoustical waves generated by resonator piezoelectricity propagate through the analyte coating and sense wave characteristic changes caused by coating-analyte interaction. Wave characteristic perturbations are transferred to the electrical output through piezoelectricity again. When microsensors are used to detect vapor or gas species, these measurands of interest are completely characterized by the mechanical property variations of coatings due to analyte mass loading, coating thickness expansion and viscoelastic perturbation. When they are used in liquid-phase applications, the detection is then characterized by the mechanical perturbations due to the contacting liquid density and viscosity. Compared to many electrical equivalent models that are extracted from input impedance or admittance through a series of assumptions, piezoelectric wave analysis without any assumptions should be more appropriate to characterize microsensors and was thus developed in chapter 2 shortly after the introduction of piezoelectric theory and TFR operation.

Unlike low-frequency quartz crystal microbalances (QCMs), thin film resonator microsensors are one-dimensional devices and are made such that the bulk membrane is in the range of several micro-meters. The membrane thickness determines the resonant frequency in the range of high MHz up to low GHz. High frequency operation provides great analyte sensitivity but, increases the detection noise. In this wave model, mechanical and electrical characteristics contributed from each layer of the TFR composite were fully included and analyzed through numerical calculation without any analytical assumption. Both longitude-mode and shear-mode TFRs were modeled. To verify the experimentally observed longitude- and shear-mode characteristics, a two-dimensional model utilizing finite difference methods was also implemented and compared with 1D wave analysis.

With understanding the wave phenomena and characteristics in the TFR composite, specially the analyte coating, the analysis and characterization of TFR polymer microsensors were then presented in chapter 3. By the analogue between acoustical and electromagnetic wave, each layer in TFR composite can be treated as an acoustic transmission-line which is characterized by layer mass density, thickness, viscoelasticity and operation frequency. The so-called 'film resonance' phenomenon was then analyzed by utilizing the concept of wave transmission and reflection, and the important physical meaning was discussed. Film resonance occurs more easily in more rubbery films. It was calculated that rubbery films with thicknesses ranging from 0.08 to 0.8  $\mu\text{m}$  (depending on viscosity) can result in film resonance at typical TFR operation frequency. With a fair amount of polymer sensor applications using surface acoustic wave devices (SAWs), sensitivity responses have been found not only contributing by added analyte mass (which is usually valid in QCM cases), but also induced by polymer volume expansion (plasticization) and viscoelastic perturbation (softening). TFRs utilize different wave mode, device configuration and higher operation frequency in contrast to SAWs; different wave characteristics are thus expected. By introducing the important concept of acoustical thickness, the wave analysis was then applied to characterize TFR polymer

microsensors along with experimental comparison. Acoustically thin polymer films used in QCMs may behave as acoustically thick in TFR applications. Experimental characterization of shear-mode TFRs was also conducted. Models considering both mass loading and thickness expansion were more close to the experimental results. The results show that only under acoustically thin polymer films, low analyte concentrations and constant temperatures, the sensitivity responses for TFR sensors can be approximately characterized as mass loading effects. However, this conclusions may not be directly applied to acoustically thick films or acoustically thin films under high analyte concentration and temperature variations since thickness expansion and viscoelasticity effects may become dominant. The sensitivity and detection limit analyses were also made along the comparison with other popular devices. This study provided very promising applications in high sensitivity microanalytical systems using bulk film resonators.

When used in liquid-phase, TFRs, like other acoustic sensors, should be able to detect liquid species and their concentration. However, wave behavior in liquid is different from that in solid. The viscous nature of contacting liquid makes waves heavily attenuated and damped away in the liquid. The liquid characteristics of interest, such as density and viscosity, are fully characterized by the wave propagation constant. For a 500 MHz shear-mode TFR, the skin depth is about 250 Å, which implies that surface condition is very critical to realizing detection purposes. By studying the wave propagation and mechanical boundary interfaced by solid TFR composite and contacting liquid, a wave model was developed to analyze liquid sensitivity responses. The experiment of utilizing a gold-plated TFR contacting with DI water was conducted and compared with the modeling. Experiments also showed the comparison between shear-mode and longitude-mode operation, and why shear-mode is better suited for TFR liquid applications. Through this study, one can see that TFRs can not only be used as solid microsensors, but also be able to provide great potential in liquid detection, especially in biosensor applications.

Microsensors utilizing bulk thin piezoelectric films have much higher sensitivity than bulk QCM sensors, mainly because of their high operation frequency. However, low material Q and high noise level are also expected at high frequency. Most presently used thin piezoelectric films are low-temperature magnetron sputtered AlN or ZnO<sub>2</sub> because the processing is relatively easy to be implemented and sputtering techniques are more appropriate to growth oriented piezoelectric films. Sputtered films have high crystal defects and void grain boundaries that may increase wave scattering and cause large crystal viscous damping. Low resonant Q and high resistance are therefore produced. These effects increase the TFR phase and thermal noise which deteriorates frequency stability. Another disadvantage of low-temperature grown films are their high temperature expansion coefficients. Wave characteristics are thus easily disturbed by the exposed environment, especially temperature fluctuation and humidity. The negative temperature coefficient of an AlN film produces a response of nonlinear shift. Although there are several ways to compensate for this drift, such as by using a compensation layer within the AlN composite, these are not optimized approaches because the processing is complex and acoustic loss will be increased. A better method presented in this work is to use the differential approach in which two almost identical TFRs are closely patterned on the same AlN membrane where one is coated as the active device and the other is passivated as a reference. The differential responses should principally be able to compensate for the response drift. In order to realize this array approach, good isolation between TFRs should be maintained to achieve high device performance. On the other hand, small die with closely placed TFRs are required to increase the packing density and device yield. The crosstalks are produced by acoustical lamb waves along AlN plate and electromagnetic waves. Wave analyses by using transient finite element method and wave-guide models were developed to investigate acoustical wave propagation, while general EM design rules were implemented to characterize electromagnetic coupling. It was found that about 300 to 400  $\mu\text{m}$  separation distance between two

adjunct TFRs were required to decouple those acoustical crosstalks. This distance is enough to isolate near-field electromagnetic L-C coupling. Since TFRs are designed and manufactured by bulk micromachining techniques, anisotropic etching of single crystal Si is required. The design of process masks should not only consider wave coupling, but also examine the geometric dimensions controlled by anisotropic etching. Photo and etch undercut tolerances were thus included in the mask design. The important process issues, such as anisotropic etching and magnetron sputtering of AlN are also discussed. The surface morphology and AlN crystal orientation were examined by AFM and SEM techniques. It was shown that the sputtered AlN had the desired c-axis perpendicular orientation and polycrystalline grains (grain size  $\sim 0.1 \mu\text{m}$ ), but the surface is relatively rough (roughness  $\sim 0.5 \mu\text{m}$ ) which indicates that the process has not yet been optimized in terms of film crystalline structure. The processed TFR arrays were measured by using two-port characterization and the results were in close agreement with the modeled.

Temperature-induced drifting was examined by using a TFR coated with a PIB polymer. A temperature coefficient of 8 -10 ppm/C for longitude-mode has been observed which could produce response drifting at the same level of noise. A temperature-compensation experiment was then conducted with a PIB-coated array. Responses from single TFRs were very sensitive to the temperature variation. Responses at high temperature were observed smaller than that at lower temperature, which indicated that analyte diffusion and desorption dominate the thermoequilibrium process. However, the differential responses from a TFR array approximately remain unchanged at different temperatures, which implies that array approach can effectively compensate temperature-induced drifting. Experiments of analyte selectivity were also made in order to realize multianalyte pattern recognition. Two TFRs were respectively coated with PIB and PMMA at the same thickness and exposed to the dilute hexane vapor. The response selectivity to hexane between PIB and PMMA films was obvious and comparable to QCM array

results. This experiment showed that TFR arrays can realize the same analyte pattern recognition as QCM array but with much smaller device size. It should be beneficial to construct a 'real' microanalytical system.

Several possible areas derived from this work can be explored for future development. In order to predict sensitivity responses and compare with QCM devices, TFR polymer sensors used in this work were deliberately coated acoustically thin. Great efforts can be made in characterization of responses from an acoustically thick rubbery polymer at high analyte concentration. Parallel work can be done in investigating temperature effects on film viscoelasticity. TFR characterization with different liquids can also be examined and compared with the model presented here. A long-term theoretical work is to conduct a complete three-dimensional numerical analysis on a piezoelectric plate in order to gain better understanding of plate wave phenomena. This 3D numerical analysis should be beneficial not only to analysis of wave properties but also to the design of monolithic acoustic filters. Of course, more experimental characterization can be done on the array selectivity testing with a great variety of analytes. The very challenging and also very urgent work, in this author's opinion, is to investigate the processing in order to construct a monolithic integrated version of TFR arrays where patterning the AIN is required and surface micromachining may be incorporated. This will eventually lead to customized microelectronic analytical systems.

## BIBLIOGRAPHY

1. M. E. Motamedi and R. M. White, in Semiconductor Sensors; S. M. Sze, ed.; John Wiley & Sons, New York, 1994, 97-152
2. G. G. Guibrey and J. M. Jordan, *CRE Crit. Rev. Anal. Chem.* 1989, 10, 54-60
3. S. J. Martin, V. E. Granstaff, and G. C. Frye, *Anal. Chem.* 1991, 63, 2272-2281
4. R. P. O'Tool, S. G. Burns, G. J. Bastiaans, M. D. Porter, *Anal. Chem.* 1992, 64, 1289-1294
5. H. Wohltjen and R. E. Dessy, *Anal. Chem.* 1979, 51, 1458-1470
6. S. J. Martin, G. C. Frye, and S. D. Senturia, *Anal. Chem.* 1994, 66, 2201-2219
7. J. W. Grate, S. J. Martin, and R. M. White, *Anal. Chem.* 1993, 65, 940-947, 987-996
8. S. W. Wenzel and R. M. White, *IEEE Trans. Electron Devices*, 1988, 35, 735-743
9. J. Xia, S. G. Burns, M. C. Porter, T. Xue, G. Liu, R. Wyse, C. Thielen, *Proc. IEEE 49th Annual Symp. on Frequency Control*, 1995, 446-450
10. S. J. Martin and G. C. Frye, *Proc. IEEE Ultrasonics Symp.* 1991, 393-398
11. J. G. Gualier, J. A. Kosinski, A. Ballato, *Proc. IEEE 1992 Ultrasonics Symp.* 1992, 183-186
12. T. Shiosaki, *Proc. IEEE 1990 Ultrasonics Symp.* 1990, 537-544
13. J. S. Wang and K. M. Lakin, *Proc. IEEE 1981 Ultrasonics Symp.* 1981, 24-27
14. K. M. Lakin, G. R. Kline, and K. T. McCarron, " *Proc. IEEE 1992 Ultrasonic Symp.* 1992, 250-256
15. R. J. Weber, S. G. Burns, C. F. Campbell, and R. O'toole, *Proc. IEEE 1992 MTT-S Digest*, 1992, 116-120
16. K. Tsubouchi and N. Mikoshiba, *Proc. IEEE 1983 Ultrasonics Symp.* 1983, 299-310

17. T. Goto, et al., *J. Mater. Sci.*, 27, 1992, Jan, 247-254
18. S. Yoshida, et al., *J. Vac. Sci. Technol.* 1993, 16, 990-993
19. F. Takeda and T. Hata, *Jpn. J. Appl. Phys.* 1980, 19, 1001-1002
20. T. Shiosaki, et al., *Appl. Phys. Lett.* , 1980, 36, 643-645
21. B. A. Auld, Acoustic Fields and Waves in Solids, John Wiley & Sons, New York , 1973, 1990,
22. G. Z. Sauerbrey, *Physik*, 1959, 155, 206-208
23. F. A. Lewis, The Palladium Hydrogen System, Academic Press, London, 1967
24. J. F. Rosenbaum, Bulk Acoustic Wave Theory And Devices, Artech House, New York, 1988
25. R. Lerch, *IEEE Trans. on Ultrasonics, Ferroelectrics, and Frequency Control*, 1990, 37, 1101-1105
26. E. Benes, *J. Appl. Phys.* 1984, 56, 508-626
27. A. D. Ballato, H. L. Berton, and T. Timir, *IEEE Trans. on Microwave Theory and Techniques*, MTT-22, 1974, 1, 14-25
28. E. L. Adler, *IEEE Trans. on Ultrasoncs, Ferroelectrinics, and Frequency Control*, 1990, 37, No. 6, 485-490
29. W. P. Mason, *Proc of IEEE*, 1969, 57, No. 10, 1723-1734
30. R. P. O'Tool, Ph. D. Dissertation, Iowa State University, 1994
31. C. F. Campbell, Ph. D. Dissertation, Iowa State Univerity, 1993
32. J. W. Grate, S. L. Rose-Pehrsson, D. L. Venezky, M. Klusty, H. Wohltjen, *Anal. Chem.*, 1993, 65, 1868-1881
33. S. L. Rose-Pehrsson, J. W. Grate, D. S. Ballantine, and P. C. Jurs, *Anal. Chem.*, 1988, 60, 280-291
34. K. M. Lakin, G. R. Kline, R. S. Ketcham, A. R. Landin, W. A. Burkland, K. T. McCarron, S. D. Breymen, S. G. Burns, *Proc. IEEE 41th Annual Symp. on Frequency Control.*, 1987, 560-566
35. T. L. Chu and R. W. Kelm, Jr., *J. electrochem. Soc.*, July, 1975, 995-999

36. S. Zirinsky and E. A. J. *electrochem. Soc.*, Feb., 1978, 305-314
37. C. R. Aita and C. J. Gawlak, *J. Vac. Sci. Technol.*, A1, 1983, 403-407
38. T. Y. Sheng, Z. Q. Yu, and G. J. Collins, *Appl. Phys. Lett.* 1986, 52, 576-582
39. R. J. Weber, S. G. Burns, and S. D. Breyden, *Proc. IEEE 1990 Ultrasonics Symp.* 1990, 525-28
40. S. J. Pearton, C. R. Abernathy, et al., *J. Semicon. Sci. Technol.* 1993, 8, 310-312
41. P. Lloyd and M. Redwood, *J. Acous. Soc. Am.*, 1965, 39, No. 2, 1945-1950
42. G. E. Forsythe, W. R. Wason, Finite-Difference Methods For Partial Differential Equation, John Wiley & Sons, New York, 1960
43. A. L. Kipling, M. Thompson, *Anal. Chem.*, 1990, 62, 1514-1519
44. HP 85165A Resonator Measurement Software Reference Manual, 1990
45. R. J. Weber, EE 413 Class Notes, Iowa State Univ., 1993
46. W. H. King, *Anal. Chem.*, 1964, 36, 1735-1739
47. R. C. Weast, M. J. Astle, W. H. Beyer, CRC Handbook of Chemistry And Physics, CRC Press, Los Angeles, 1983
48. J. R. Vig and F. L. Walls, *Proc. IEEE 48th Annual Symp. on Frequency Control*, 1994, 506-523
49. D. S. Bailey, M. M. Driscoll, R. A. Jelen, and B. R. McAvoy, *IEEE Trans. on Ultrasonics, and Ferroelectrics, and Frequency Control*, 1992, 39, 92-98
50. P. L. Konash, G. J. Bastiaans, *J. Anal. Chem.*, 1980, 52, 1929-31
51. B. A. Martin, S. W. Wenzel, R. M. White, *Sens. Actuators 1990*, A21-A23, 704-708
52. H. F. Tiersten, Liner Piezoelectric Plate Vibrations, Plenum Press, New York, 1969, 825-890
53. J. T. Stewart and Yook-Kong Yong, *Proc. IEEE Annual Symp. On Frequency Control*, 1993, 476-501
54. Sheng Jian-ni, Numerical Analysis of Electromagnetic Fields (in Chinese), Science Press. Beijing, 1984

55. X. Tue, et al., *Review of Progress in QNDE*, 1995, 14, 12-19
56. Z. You, M. Lust, et al., *IEEE Trans. On Ultrasonics, Ferroelectrics, and Frequency Control*, 1991, 38, 436-45
57. E. A. Woff and R. Kaul, *Microwave Engineering and System Application*, John Wiley & Sons, New York, 1988
58. Kai Chang, *Microwave Solid-State Circuits And Applications*, John Wiley, and Sons, New York., 1994
59. X. Li, et al, *Thin Solid Films*, 1988, 139, 261-274
60. G. Ravender, *Monolithic Microwave Integrated Circuits: Technology & Design*, Artech House, New York, 1989
61. S. K. Ghanhdi, *VLSI Fabrication Principles*, 2nd ed., John, Wiley & Sons, New York, 1994
62. W. R. Runyan, and K. E. Bean, *Semiconductor Integrated Circuit Process Technology*, John Wiley & Sons, New York, 1990
63. M. J. Declercq, L. Gerberg, and J. D. Meindl, *J. Electrochem. Soc.* 1975, 122, 545-553
64. M. K. Petersen, *MS Thesis*, Iowa State University, 1985
65. J. A. Thornton, *Ann. Rev. mater. Sci.*, 1977, 7, 239-246
66. H. Okano, Y. Takahashi, T. Tanaka, *Jpn. J. Appl. Phys.* 1992, 31, 3446-3450
67. G. I. Huffman, D. E. Fahnlne, *J. Vac. Sci. Technol.*, 1989, A7, 2252-2256
68. Hwan-Chul Lee and Jai-Young Lee, *J. Mater. Sci.*, 1993, 9, 91-98
69. W. J. Meng, J. A. sell, G. L. Eesley and T. A. Perry, *J. Appl. Phys.* 1993, 74 No. 4, 15-20
70. H. Middlemen, *Process Engineering Analysis In Semiconductor Device Fabrication*, John Wiley & Sons, New York, 1993
71. G. E. McMuire, *Semiconductor Materials and Process Technology Handbook*, Noyes Publications, Houston, 1988, 430-460
72. Hong Xu, Private Communications on QCM Array Testing, Sept. 1995

## ACKNOWLEDGMENTS

I would like to express gratitude to my major professor Dr. Stanley G. Burns for his guidance, encouragement and support throughout this investigation. I would also like to thank Dr. Marc D. Porter for his support concerning about the TFR array characterization and for serving on my committee. I am very indebted to my other committee members, Dr. Howard R. Shanks, Dr. Robert J. Weber, Dr. Hsung-Cheng Hsieh and Dr. Joseph Shinar for serving on my committee.

I would like to thank Department of Energy to fund this research, Microelectronics Research Center and Microanalytical Instrumentation Center for the use of processing facilities and characterization equipment. I would also like to thank Casey Thielen, Dave Schmidt, Al Landin and Dr. Alan Constant of Microelectronics Research Center for processing TFR and array wafers, and Dr. Hang Xu of Microanalytical Instrument Center for array coating development. Many thanks also go to Russ Wyse, Denny Drees, Dr. G. Liu, Dr. Ruth Shinar, Dr. R. Libert and Dr. E-X Ping for numerous discussions and help. A very special thank goes to my wife for her endless patience and boundless support.

APPENDIX I IEEE TFR MICROSENSOR PAPER

- A paper presented at 1995 IEEE international frequency control  
symposium, May, 1995, San Francisco

A Micromachined Sensor Array Using Thin Film Resonators

J. Xia, S. Burns, M. Porter, G. Liu, R. Wyse, C. Thielen

Microelectronics Research Center, Ames Laboratory, Iowa  
State University, 1925 Scholl Road, Ames, IA 50011

Abstract

This paper describes the design, modeling and implementation of a microsensor array using aluminum nitride thin film resonators. A finite element method, formulated to accommodate the anisotropic and piezoelectric properties of aluminum nitride, is used to model acoustic wave coupling between resonators and to define the mask design. Two arrays on the same aluminum nitride membrane were fabricated using standard semiconductor processing. The measurements were in agreement with the modeling. A multilayer Mason model was applied to investigate the mass loading and viscoelastic effects via hydrogen absorption on the PdNi coated TFR. The preliminary H<sub>2</sub> sensitivity tests on a TFR hydrogen sensor are also presented.

## APPENDIX II MATRIX AND ENGINEERING NOTATION

## Full and abbreviated subscripts

Full(or Engineering)	Abbreviated(or Matrix)
(xx) 11	1
(yy) 22	2
(zz) 33	3
(yz, zy) 23, 32	4
(xz, zx) 13, 31	5
(xy, yx) 12, 21	6

## Analogue between electrical and acoustic transmission-line

Acoustic transmission-line

Electrical transmission-line

Negative Stress  $-T_j$ — Voltage  $V$ Particle Velocity  $v_i$ — Current  $I$ Mass density  $\rho$ — Inductance  $L$  per unitInverse Stiffness Coef.  $c_{ij}^{-1}$  — Capacitance  $C$  per unit

$$\text{Characteristic impedance } Z_a = (\rho c_{ij})^{\frac{1}{2}} \left(1 + \frac{i\omega\eta_{ij}}{c_{ij}}\right)^{\frac{1}{2}} \quad \text{—} \quad Z_e = \left(\frac{L}{C}\right)^{\frac{1}{2}} \left(1 + i\frac{\omega C}{G}\right)^{\frac{1}{2}}$$

## APPENDIX III DERIVED ALN MATERIAL MATRIX

A(j,k)	k=1	2	3	4
j=1	c <sub>11</sub>	c <sub>16</sub>	c <sub>15</sub>	e <sub>11</sub>
2	c <sub>61</sub>	c <sub>66</sub>	c <sub>65</sub>	e <sub>16</sub>
3	c <sub>51</sub>	c <sub>56</sub>	c <sub>55</sub>	e <sub>15</sub>
4	e <sub>11</sub>	e <sub>16</sub>	e <sub>15</sub>	-e <sub>11</sub>

B(j,k)	k=1	2	3	4
j=1	c <sub>66</sub>	c <sub>62</sub>	c <sub>64</sub>	e <sub>26</sub>
2	c <sub>26</sub>	c <sub>25</sub>	c <sub>24</sub>	e <sub>22</sub>
3	c <sub>46</sub>	c <sub>45</sub>	c <sub>44</sub>	e <sub>24</sub>
4	e <sub>26</sub>	e <sub>22</sub>	e <sub>24</sub>	-e <sub>22</sub>

C(j,k)	k=1	2	3	4
j=1	c <sub>55</sub>	c <sub>54</sub>	c <sub>53</sub>	e <sub>35</sub>
2	c <sub>45</sub>	c <sub>44</sub>	c <sub>43</sub>	e <sub>34</sub>
3	c <sub>35</sub>	c <sub>34</sub>	c <sub>33</sub>	e <sub>33</sub>
4	e <sub>35</sub>	e <sub>34</sub>	e <sub>33</sub>	-e <sub>33</sub>

D(j,k)	k=1	2	3	4
j=1	c <sub>16</sub>	c <sub>12</sub>	c <sub>14</sub>	e <sub>21</sub>
2	c <sub>66</sub>	c <sub>62</sub>	c <sub>64</sub>	e <sub>26</sub>
3	c <sub>56</sub>	c <sub>52</sub>	c <sub>54</sub>	e <sub>25</sub>
4	e <sub>16</sub>	e <sub>12</sub>	e <sub>14</sub>	-e <sub>12</sub>

E(j,k)	k=1	2	3	4
j=1	c <sub>61</sub>	c <sub>66</sub>	c <sub>65</sub>	e <sub>16</sub>
2	c <sub>21</sub>	c <sub>26</sub>	c <sub>25</sub>	e <sub>12</sub>
3	c <sub>41</sub>	c <sub>46</sub>	c <sub>45</sub>	e <sub>14</sub>
4	e <sub>21</sub>	e <sub>26</sub>	e <sub>25</sub>	-e <sub>21</sub>

F(j,k)	k=1	2	3	4
j=1	c <sub>15</sub>	c <sub>14</sub>	c <sub>13</sub>	e <sub>31</sub>
2	c <sub>65</sub>	c <sub>64</sub>	c <sub>63</sub>	e <sub>36</sub>
3	c <sub>55</sub>	c <sub>54</sub>	c <sub>53</sub>	e <sub>35</sub>
4	e <sub>15</sub>	e <sub>14</sub>	e <sub>13</sub>	-e <sub>13</sub>

G(j,k)	k=1	2	3	4
j=1	c <sub>51</sub>	c <sub>56</sub>	c <sub>55</sub>	e <sub>15</sub>
2	c <sub>41</sub>	c <sub>46</sub>	c <sub>45</sub>	e <sub>14</sub>
3	c <sub>31</sub>	c <sub>36</sub>	c <sub>35</sub>	e <sub>13</sub>
4	e <sub>35</sub>	e <sub>34</sub>	e <sub>33</sub>	-e <sub>33</sub>

H(j,k)	k=1	2	3	4
j=1	c <sub>65</sub>	c <sub>64</sub>	c <sub>13</sub>	e <sub>36</sub>
2	c <sub>25</sub>	c <sub>24</sub>	c <sub>23</sub>	e <sub>32</sub>
3	c <sub>45</sub>	c <sub>44</sub>	c <sub>43</sub>	e <sub>34</sub>
4	e <sub>25</sub>	e <sub>24</sub>	e <sub>23</sub>	-e <sub>23</sub>

I(j,k)	k=1	2	3	4
j=1	c <sub>56</sub>	c <sub>52</sub>	c <sub>54</sub>	e <sub>25</sub>
2	c <sub>46</sub>	c <sub>42</sub>	c <sub>44</sub>	e <sub>24</sub>
3	c <sub>36</sub>	c <sub>32</sub>	c <sub>34</sub>	e <sub>23</sub>
4	e <sub>36</sub>	e <sub>32</sub>	e <sub>34</sub>	-e <sub>32</sub>

APPENDIX IV ALN AND QCM ELASTIC, PIEZOELECTRIC AND PERMITTIVITY MATRIX

AIN elasticity

$$c = \begin{bmatrix} c_{11} & c_{12} & c_{13} & 0 & 0 & 0 \\ c_{12} & c_{11} & c_{13} & 0 & 0 & 0 \\ c_{13} & c_{13} & c_{33} & 0 & 0 & 0 \\ 0 & 0 & 0 & c_{44} & 0 & 0 \\ 0 & 0 & 0 & 0 & c_{44} & 0 \\ 0 & 0 & 0 & 0 & 0 & c_{66} \end{bmatrix}$$

$$\begin{aligned} c_{11} &= 3.45 \times 10^{11} \text{ N/m}^2 \\ c_{12} &= c_{13} = 120 \times 10^{11} \text{ N/m}^2 \\ c_{33} &= 3.95 \times 10^{11} \text{ N/m}^2 \\ c_{44} &= 1.18 \times 10^{11} \text{ N/m}^2 \\ c_{66} &= (c_{11} - c_{12}) / 2 \end{aligned}$$

AIN piezoelectricity

$$e = \begin{bmatrix} 0 & 0 & 0 & 0 & e_{15} & 0 \\ 0 & 0 & 0 & e_{15} & 0 & 0 \\ e_{31} & e_{31} & e_{33} & 0 & 0 & 0 \end{bmatrix}$$

$$\begin{aligned} e_{15} &= -0.48 \text{ C/m}^2 \\ e_{31} &= -0.58 \text{ C/m}^2 \\ e_{33} &= 1.55 \text{ C/m}^2 \end{aligned}$$

AIN permittivity

$$\varepsilon = \begin{bmatrix} \varepsilon_{11} & 0 & 0 \\ 0 & \varepsilon_{11} & 0 \\ 0 & 0 & \varepsilon_{33} \end{bmatrix}$$

$$\begin{aligned} \varepsilon_{11} &= 8.0 \times 10^{-11} \text{ F/m} \\ \varepsilon_{33} &= 9.5 \times 10^{-11} \text{ F/m} \end{aligned}$$

The AT-QCM elastic and piezoelectric constants used in the modeling are

$$\begin{aligned} c_{66} &= 2.90224 \times 10^{10} \text{ N/m}^2 \\ e_{26} &= 0.0949 \text{ C/m}^2 \\ \varepsilon_{22} &= 3.981 \times 10^{-11} \text{ F/m} \end{aligned}$$

## APPENDIX V FINITE DIFFERENCE ADMITTANCE

All the mesh spaces used in finite difference method were equally chosen for the consideration of simplification and calculation accuracy

$$h_E = h_W = h_N = h_S = h$$

then the finite admittance for the central difference equation can be written as

$$Y^E(j,k) = Y^W(j,k) = \frac{A_{jk}}{h^2}$$

$$Y^N(j,k) = Y^S(j,k) = \frac{C_{jk}}{h^2}$$

$$Y^{NE}(j,k) = Y^{SW}(j,k) = \frac{H_{jk} + I_{jk}}{4h^2}$$

$$Y^{NW}(j,k) = Y^{SE}(j,k) = -\frac{H_{jk} + I_{jk}}{4h^2}$$

$$Y^P(j,k) = \begin{cases} -\frac{2(A_{jk} + C_{jk})}{h^2} + \rho\omega^2 & \text{for } j = k \\ -\frac{2(A_{jk} + C_{jk})}{h^2} & \text{for } j \neq k \end{cases}$$

The finite admittance for the two traction forces were then given by

$$Y_1^E(j,k) = -Y_1^W(j,k) = \frac{A_{jk}}{2h}$$

$$Y_1^N(j,k) = -Y_1^S(j,k) = \frac{H_{jk}}{2h}$$

$$Y_3^N(j,k) = -Y_3^S(j,k) = \frac{C_{jk}}{2h}$$

$$Y_3^E(j,k) = -Y_3^W(j,k) = \frac{I_{jk}}{2h}$$

$$Y_1^P(j,k) = Y_3^P(j,k) = 0$$

APPENDIX VI DERIVATION OF THE STRAIN RATIO GENERATED BY  
CROSS-FILM GRADIENTS TO IN-PLANE GRADIENTS

Polymer film deformation generated by TFR is shown in the following grid diagram where in-plane gradients dominates in an acoustically thin polymer and considerable cross-film displacement gradients arise in an acoustically thick polymer.

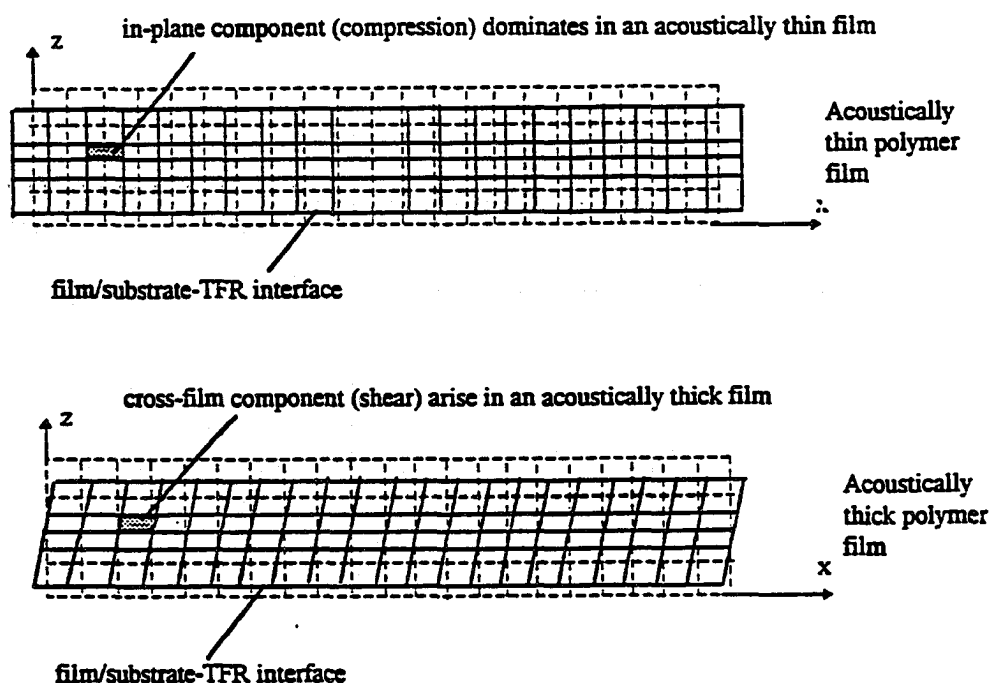


Figure AP-1 Film deformation in a TFR polymer sensor

Wave propagation in the z-direction of a film-coated substrate cause film displacements given a general form as

$$\bar{u}(z) = \tilde{C}(z)e^{-jz} \quad (III-1)$$

where  $\kappa$  is the wave number. In-plane displacement gradients arise from harmonic variation in the  $z$  direction, where  $\tilde{C}$  is approximately constant cross film thickness. Upper film surface vibrates in phase with the low substrate TFR/film driven interface. From the strain definition of

$$S_{ij} = \frac{1}{2} \left( \frac{\partial u_i}{\partial x_j} + \frac{\partial u_j}{\partial x_i} \right) \quad (\text{III-2})$$

then

$$S_{xz} = S_{zx} = \frac{1}{2} \frac{\partial u_x}{\partial z} = -\frac{j\kappa u_x}{2}$$

$$S_{yz} = S_{zy} = \frac{1}{2} \frac{\partial u_y}{\partial z} = -\frac{j\kappa u_y}{2}$$

$$S_{zz} = \frac{\partial u_z}{\partial z} = -j\kappa u_z$$

the in-plane strain can be given as

$$S^{(IP)} = (S_{xz}^2 + S_{yz}^2)^{\frac{1}{2}} + S_{zz} = \frac{\kappa}{2} (u_x^2 + u_y^2)^{\frac{1}{2}} + \kappa u_z \quad (\text{III-3})$$

Since compression strain is much large than the shear strains for the in-plane displacement and assume displacement is constant across the film thickness. Also, the isotropic properties is applied in the transverse  $x, y$  plane because of the hexagonal symmetry of substrate AlN plate. Then

$$S^{(IP)} = \frac{\kappa}{2} (u_{x0}^2 + u_{y0}^2)^{\frac{1}{2}} + \kappa u_{z0} = \frac{\sqrt{2}}{2} \kappa u_{x0} + \kappa u_{z0} \approx \kappa u_{z0} \quad (\text{III-4})$$

where the uniform film displacement have been replaced by the displacement at the substrate TFR/film interface,  $u_D, i = x, y, z$ .

The cross-film stain arise from the inertial lag of displacement of upper film surface with respect to the substrate-TFR/film interface. Shear wave velocity is low enough that the shear displacement gradients arise, which leads to consierabl shear strain in the film. The  $\tilde{C}$  in (III-1) is no longer a constant complex. From the continuity equation

$$\sum_{j=1}^3 \frac{\partial T_{ij}}{\partial x_j} = -\rho_c \omega^2 u_i \quad (\text{III-5})$$

Since no stress is created in the transverse isotropic plane, then (III-5) can be written as

$$\frac{\partial T_{iz}}{\partial x_z} = -\rho_c \omega^2 u_i \quad (\text{III-6})$$

Assume film has  $h$  thickness. The stress-free at the upper film surface ( $T_B(h) = 0$ ), leads to the stress at substrate-TFR/film interface written as

$$T_{iz}(0) = \rho_c \omega^2 u_D h_c \quad (\text{III-7})$$

The shear strains are related to stress by

$$S_{iz}(0) = \frac{1}{2G_c} T_{iz}(0) \quad (\text{III-8})$$

where  $G_c$  is the shear modulus of the film. Then the cross-film strains, by substituting (III-7) into (III-8), can be given as

$$S^{(CF)} = \frac{\rho_c \omega^2 h_c}{2G_c} (u_{x0}^2 + u_{y0}^2)^{\frac{1}{2}} = \frac{\sqrt{2} \rho_c \omega^2 h_c}{2G_c} u_{x0} \quad (\text{III-9})$$

The ratio of strain magnitude induced by cross-film to in-plane gradients can be then written as

$$R = \frac{S^{(CF)}}{S^{(IP)}} = \frac{\sqrt{2} \rho_c \omega^2 h_c}{2G_c \kappa} \frac{u_{x0}}{u_{z0}} = \frac{A f \rho_c h_c}{G_c} \quad (\text{III-10})$$

where  $A$  is a constant related to substrate TFR,  $A = \frac{\sqrt{2} \pi v_0 u_{x0}}{u_{z0}}$ . Phase velocity

$v_0 = \frac{\omega}{\kappa}$  is also used in (III-10). Using the definitions of  $u_{i0} = \frac{v_{i0}}{\sqrt{4\kappa P}}$  and

$\frac{v_{x0}}{v_{z0}} = \frac{\sqrt{c_{44}/\rho}}{\sqrt{c_{33}/\rho}}$ , where  $P$  is wave power density (Poynting energy) [ ], then  $A$  can be

calculated to be 2.66 for AlN/TFR.